POLITECNICO MILANO 1863

SCUOLA DI INGEGNERIA INDUSTRIALE E DELL'INFORMAZIONE

Advanced Methods for Multi-Encounter Conjunction Assessment

Tesi di Laurea Magistrale in Space Engineering - Ingegneria Spaziale

Author: **Alejandro Álvarez Salazar**

Student ID: 11073754
Advisor: Prof. Pierluigi Di Lizia
Co-advisors: Dr. Diego Escobar Antón, Diego Aranda Pradana, Jorge Rubio Antón
Academic Year: 2025-26

Abstract

The operational risk for active satellites is increased by the continuous growth of the orbital object population, driven by frequent launches, large constellations, and space debris. Consequently, multiple encounter situations involving the same satellite are increasingly frequent. This requires new solutions in Space Surveillance and Tracking (SST) to guarantee operational safety.

To address this, an analytical framework aimed at accurately estimating the Total Probability of Collision (TPoC) in multiple encounter scenarios is developed in this thesis. Traditional conservative risk estimations are refined as the main objective, enabling the design of more efficient collision avoidance maneuvers (CAM) in later phases.

To this end, a methodology integrating the statistical correlation between successive events is proposed. This correlation is based on the continuous participation of the same primary satellite, dynamical model uncertainties, and recurring encounters with the same secondary object. The influence of these factors on the TPoC calculation is evaluated to determine under what conditions the results diverge from the standard approximations currently used in real operations and the literature.

The methodological development is initially based on the resolution of a simplified two-dimensional problem. The segregation of the different sources of correlation is allowed by this preliminary analytical approach, allowing a preliminary analysis to quantify the individual contribution of each effect to the total risk.

Subsequently, the model is extrapolated to a realistic three-dimensional orbital environment. The two-dimensional formulation is transformed step by step into the final analytical expression, applying various mathematical methods for its dimensional simplification and subsequent integration.

Finally, an analysis of the feasible operational configurations and their respective orders of magnitude is carried out. To conclude, the methodology is validated through the numerical resolution of specific scenarios, demonstrating the correct functioning of the methods and evidencing their potential for future operational implementation.

Keywords: Multi-Encounter, TPoC, Space Surveillance and Tracking (SST).

Sommario

Il rischio operativo per i satelliti attivi è aumentato dalla continua crescita della popolazione di oggetti orbitali, trainata dai frequenti lanci, dalle grandi costellazioni e dai detriti spaziali. Di conseguenza, le situazioni di incontri multipli che coinvolgono lo stesso satellite sono sempre più frequenti. Ciò richiede nuove soluzioni nell'ambito della sorveglianza e del tracciamento spaziale (SST) per garantire la sicurezza operativa.

Per affrontare questo problema, in questa tesi viene sviluppato un quadro analitico volto a stimare con precisione la probabilità totale di collisione (TPoC) in scenari di incontri multipli. Le tradizionali stime di rischio conservative vengono affinate come obiettivo principale, consentendo la progettazione di manovre di evitamento delle collisioni (CAM) più efficienti nelle fasi successive.

A tal fine, viene proposta una metodologia che integra la correlazione statistica tra eventi successivi. Questa correlazione è basata sulla partecipazione continua dello stesso satellite primario, sulle incertezze dei modelli dinamici e sui ricorrenti incontri con lo stesso oggetto secondario. L'influenza di questi fattori sul calcolo della TPoC viene valutata per determinare in quali condizioni i risultati divergono dalle approssimazioni standard attualmente utilizzate nelle operazioni reali e in letteratura.

Lo sviluppo metodologico si basa inizialmente sulla risoluzione di un problema bidimensionale semplificato. La separazione delle diverse fonti di correlazione è consentita da questo approccio analitico preliminare, permettendo un'analisi iniziale per quantificare il contributo individuale di ogni effetto al rischio totale.

Successivamente, il modello viene estrapolato in un ambiente orbitale tridimensionale realistico. La formulazione bidimensionale viene trasformata passo dopo passo nell'espressione analitica finale, applicando vari metodi matematici per la sua semplificazione dimensionale e successiva integrazione.

Infine, viene condotta un'analisi delle configurazioni operative fattibili e dei rispettivi ordini di grandezza. Per concludere, la metodologia viene convalidata attraverso la risoluzione numerica di scenari specifici, dimostrando il corretto funzionamento dei metodi ed evidenziando il loro potenziale per una futura implementazione a livello operativo.

Parole chiave: Incontri Multipli, TPoC, Sorveglianza e Tracciamento Spaziale (SST).

Contents

1 | Introduction

This first chapter presents an overview of the context needed to follow and understand the development of the thesis, which aims to obtain a better formula to measure the total collision probability for space satellites in scenarios involving multiple encounters, and verify in which cases it could be used instead of the actual approximations.

1.1. Background

The chapter begins with an overview of the space debris problem, its origins, the current population trends, and the risks that it presents to operational infrastructure. This section remarks the importance of the situation and the importance of robust mitigation strategies.

Following this, the chapter introduces the Space Surveillance and Tracking (SST) loop. This section describes the continuous cycle of detection, cataloging, and risk assessment that is essential for maintaining Space Situational Awareness (SSA). It establishes the operational framework currently used to monitor and predict the motion of resident space objects.

Finally, the chapter defines the specific role of this thesis within the SST loop. It identifies the limitations of current risk approximation methods and demonstrates how the research presented here contributes to the safety and reliability of the loop, specifically taking into account the complex challenge of multi-encounter collision probability. The complete problem formulation is then detailed in Chapter 1.4.

1.1.1. The Space Debris Problem

Over the past decades, space debris has become one of the main problems for the long-term sustainability of space operations. The increase in space activity, together with the fast growth in the number of satellites in low-Earth orbit, has accelerated the accumulation of non controlled objects that remain in orbit for long periods of time. As a result, operating in the near-Earth environment now requires continuous monitoring, accurate modelling, and coordinated evasion operations from agencies and operators.

Origin and Growth of Space Debris

Since the launch of Sputnik-1, more than 70 years ago, humanity has been expanding its presence in space, sending an increasing number of instruments beyond the atmosphere. These goes from small probes and technology demonstrators to large telescopes and satellite constellations that provide essential services such as communications, navigation, and Earth and Deep Space observation. Consequently, Earth's orbital environment has become essential for scientific, commercial, and governmental activities, with thousands of active satellites supporting services now integrated into everyday life.

However, this progress brings some challenges. One of the most important is the continuous increase of space debris in Earth's orbits, generated by decades of launches, collisions, fragmentations, and abandoned spacecraft. Satellites now share their orbits with millions of fast-moving debris objects, whose size goes from undetectable debris smaller than 1 cm, to complete inactive satellites, each travelling at several kilometres per second. Even small debris can incapacitate or destroy an operating spacecraft, potentially creating additional debris [1].

According to the 2025 European Space Agency (ESA) Space Environment Report [2], the catalogue currently includes about 39000 objects in Earth orbit by January 1st, 2025, combining both catalogued and asserted objects. Only around 14000 of these are operational payloads, while the remaining 25000 consist of inactive payloads, spent rocket bodies, and debris fragments. The distribution is concentrated in Low Earth Orbit (LEO), which contains approximately 22000 objects, followed by Medium Earth Orbit (MEO) and the Geostationary region (GEO) (see Figure 1.1).

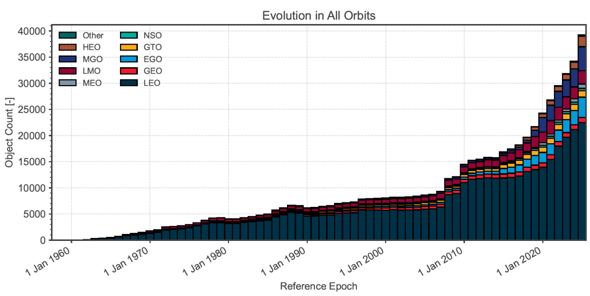

(a) Classification by orbit class

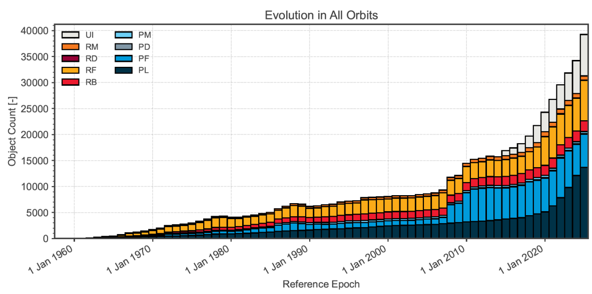

(b) Classification by object class

Figure 1.1: Evolution of number of objects in geocentric orbit [2].

Fragmentation remains the dominant mechanism producing debris that increase the orbital population around Earth. ESA records 656 fragmentation events since the beginning of space activities, with 220 occurring in the last two decades and an average of 9–10 non-deliberate events per year [2]. Many of these events are caused by propulsion anomalies, failures, or unexplained factors, generating thousands of long-lived debris fragments, see Figure 1.2.

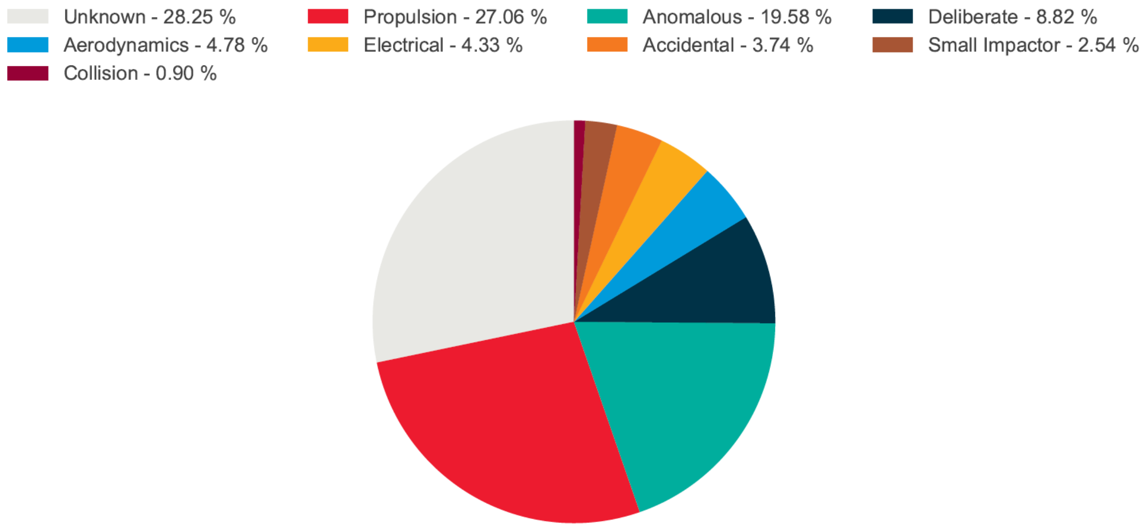

Figure 1.2: Event causes for all past fragmentation events [2].

Another, more recent, source of objects in LEO has been the development of big satellite constellations. In 2024 alone, over 1500 new objects has been launched to this region [2]. While the majority of these are active payloads, a significant part could eventually become inactive if the mitigation operations are not successfully executed at the end of its life-time.

In LEO, atmospheric drag plays a key role in the natural removal of debris. Objects in low-Earth orbit gradually lose altitude due to atmospheric resistance, with reentry times from years to decades depending on their altitude. But objects launched to higher orbits, such as GEO, can remain in space for thousands of years if no active deorbiting activities are taken [1].

As a consequence, the current orbital environment is shaped not only by historical fragmentation events but also by sustained launch activity and incomplete mitigation operations.

Risk to Space Environment

As discussed in the previous section, the population of debris in Earth orbit is continuously growing, and consequently, the probability of collisions for active satellites increases. This situation represents an important threat to the safety and operation of functional spacecraft, highlighting the importance of continuous monitoring and risk assessment.

Even small fragments, on the order of a few centimetres, can disable or even destroy an operational satellite if the impact speed is enough, generating new debris [3]. Currently, Low Earth Orbit (LEO) is the most affected due to its high population density. Other orbital regions, such as MEO or GEO, are less populated but also contain some satellites that are vital for Earth observation, navigation, and communications, which cannot be neglected.

To reduce these risks, it is important the continuous observation and monitoring of the space debris population. Estimating collision probabilities becomes critical particularly for scenarios involving multiple conjunctions, where the total risk must be considered. Operators depend on conjunction analysis, probabilistic methods, and accurate propagation models to execute avoidance manoeuvres while minimizing operational disruption.

The operational impact on active satellites has been notable over recent years. The International Space Station (ISS) has performed around 37 avoidance manoeuvres between 1999 and 2023 [4]. ESA reports that it executes 12 collision avoidance manoeuvres per year [5]. Specifically, in more densely populated regions like LEO, ESA satellites perform around two avoidance manoeuvres per satellite per year, while missions requiring closer monitoring, such as Sentinel-type satellites, may perform manoeuvres approximately every three months [6]. These operations involve careful planning, temporary data interruptions, and fuel consumption.

These examples show the importance of continuous observation, probabilistic risk assessment, and the development of new methods to estimate total collision probabilities in multiple-event scenarios.

1.1.2. Space Surveillance and Tracking

The continuous growth of objects in orbit has made Space Surveillance and Tracking (SST) an important element of current Space Situational Awareness (SSA) activities. In Europe, ESA's SSA programme [7] was created to provide independent and reliable information about the space environment, analysing artificial objects, debris, natural hazards, re-entry events, and space weather.

Within this programme, the Space Surveillance and Tracking (SST) segment [8] is responsible for detecting, tracking, cataloguing, and predicting the orbits of space objects. It covers both operational satellites and debris, and supplies the information needed for conjunction analysis, collision risk assessment, and re-entry prediction. SST is therefore one of the operational pillars of Europe's SSA capability [9], combining sensor networks, catalogue maintenance, conjunction detection, and collision avoidance support. Its goal is simple: to maintain an up-to-date and consistent catalogue of the orbital environment so operators can identify potential risks and react when needed.

SST follows a closed-loop process in which observations are collected, orbits are estimated and propagated, close approaches are detected, and decisions are made regarding potential avoidance manoeuvres. Once new measurements arrive, the cycle starts again. The following sections describe the main stages of this workflow and place the topic of this thesis, the estimation of total collision probability in multi-encounter scenarios, within this context.

Sensor Measurements

The SST cycle starts with the observational data. These observations come from ground-based radar systems, optical telescopes, and laser ranging stations placed around the world. Radar sensors are especially useful for tracking objects in Low Earth Orbit (LEO), where short ranges and high relative velocities make optical observations less effective. Optical sensors are more suitable for Medium Earth Orbit (MEO) and Geostationary Orbit (GEO), where the angular rates are lower and observation windows are longer, allowing more accurate measurements.

Each type of sensor provides different kinds of measurements. Radar sensors provide information about the azimuth, elevation, range, range-rate and radar cross section (RCS) of the object. On the other hand, optical sensors provide information about the right ascension, declination and visual apparent magnitude. Once a set of observations of an object is performed, the information coming from different sensors in the network needs to be integrated. All measurements are affected by noise, biases, and environmental effects such as atmospheric refraction. Because of these limitations, a single observation is not enough to determine an orbit, so the catalogue depends on repeated measurements over time to improve the accuracy. The uncertainty of each sensor must be estimated and modelled, since it affects the orbit determination step and, later, the propagation and prediction of close approaches.

A particular challenge appears when tracking small debris objects. Their low radar cross section or low optical brightness makes them difficult to detect and often leads to large measurement uncertainties. As a result, the orbits of small fragments uses to be less accurate.

Orbit Determination

Once measurements are available, the orbit determination (OD) phase combines them to estimate the position, velocity, and associated uncertainty of each object. Modern OD techniques combine data from different sensors using two principal types of OD methods [10]:

Batch or least-squares estimator, which processes a full set of observations at once. The a priori state is first propagated to the times of the measurements, and simulated measurements are generated using the sensor models. The algorithm then adjusts the trajectory and model parameters to minimise the squared difference between simulated and real measurements. This fitting process is repeated until the solution converges.

Sequential estimator or Kalman filter handles measurements one by one. The state and covariance are first propagated to the time of the new observation, and then corrected using the measurement and its uncertainty through a weighted update.

These methods needs an accurate dynamic model to work and provide a decent estimation of the current state. This model may introduce errors to the estimated state (for example, errors in the perturbation models), that must be added to the errors committed during the measurement phase, and modelled as uncertainties that are represented through covariance matrices that quantify the dispersion in the estimated state.

In operational contexts, orbital states and covariances are transmitted following the standards established by the Consultative Committee for Space Data Systems (CCSDS)[11]. This defines the Orbit Parameter Message (OPM) format, which provide consistent definitions of reference frames, time systems, and useful identifying information about the object studied.

Furthermore, there are others sources available, one of the most used catalogues is released by NASA, derived from the catalogue maintained by the United States Space Command (USSPACECOM). The public version of this catalogue, including Two-Line Element (TLE) sets and other orbital data products, is distributed through CelesTrak, which mirrors and redistributes the official catalogue updates [12]. This provides an accessible source of regularly updated orbital data for satellites and trackable debris.

Orbit Propagation

Once the orbital state has been estimated, it must be propagated forward in time to predict future positions and uncertainties. Orbit propagation is based on dynamical models [10] that include the main perturbations acting on satellites and debris. These models describe how the orbit evolves under the influence of gravity, atmospheric drag, radiation pressure, and other forces, and are therefore required for any propagation.

Along with the state, its uncertainty is also propagated. Because of this, the uncertainty at the time of closest approach depends not only on the quality of the measurements, but also on how the dynamical model is designed. Orbit propagation is therefore the link between orbit determination and conjunction determination.

Orbital Perturbations Objects in orbit around the Earth are following a pure keplerian motion. A number of other forces act on satellites and debris, gradually changing their orbits over time. A model for these effects is needed for propagating trajectories, planning avoidance manoeuvres, and estimating collision probabilities.

In this section, only a fast review of the most important sources of perturbations will be developed, for the complete models and a more detailed definition see *Satellite Orbits: Models, Methods and Applications* [10].

In Low Earth Orbit (LEO), atmospheric drag is the largest non-gravitational effect. Even at altitudes of several hundred kilometres, the residual atmosphere produces a continuous force, gradually reducing their velocity and lowering their orbits. Over long periods, this effect can lead to the eventual re-entry and decay of the object. The magnitude of drag depends on the density of the atmosphere, which varies with solar activity, as well as the object's area-to-mass ratio and orientation.

Earth's gravitational field is not uniform due to the planet's oblateness and variations in mass distribution. These irregularities induce slow changes in the orbital plane and in parameters such as the argument of perigee and the right ascension of the ascending node. The effects are most pronounced in LEO and MEO, where small deviations can accumulate over time, altering the long-term evolution of orbits.

Gravitational perturbations from third bodies, primarily the Moon and the Sun, become increasingly relevant in Medium Earth Orbit (MEO) and Geostationary Orbit (GEO). These forces modify the eccentricity and inclination of the orbit, and can lead to periodic or secular variations that must be considered for accurate long-term predictions and station-keeping operations.

Solar radiation pressure, resulting from the momentum transfer of photons hitting the satellite's surfaces, is particularly important for high-altitude, low-mass, and large-area satellites, such as those in GEO or with deployable solar panels. This effect gradually alters orbital elements, mainly eccentricity and inclination, and can induce long-term drift if not compensated by control manoeuvres.

Other minor perturbations include tidal forces, relativistic corrections, and interactions with Earth's magnetic field, which are generally small but can be relevant for precise orbit determination and collision probability analysis.

These perturbations need complex models that has been developed, but them may have errors in their coefficients, or in their approximations. These errors become a source of common uncertainty that makes important the accurate modelling of perturbations and their uncertainties for studying collision risk and estimating total probabilities in multi-ecnounter scenarios.

Propagation Reference Frames and Standards Orbit propagation requires a clear definition of the reference frames and standards used to express the state vectors. In this work, the two main frames are the Geocentric Celestial Reference Frame (GCRF) and the Tangent–Normal–W (TNW) local frame. All computations are referenced to Coordinated Universal Time (UTC). For a complete definition of these frames see *Satellite Orbits: Models, Methods and Applications* [10].

The GCRF is an inertial frame centred at the Earth's centre of mass and aligned with the International Celestial Reference System (ICRS). It is the standard frame used in most orbit propagators and in the CCSDS Orbit Ephemeris Message (OEM), which provides a common format for exchanging orbital information between agencies and operators.

For analysing relative motion and uncertainty, a local frame attached to the spacecraft is more practical. Here, the TNW frame is used. The T axis is aligned with the velocity vector (along-track), the N axis is normal to the orbital plane (cross-track), and the W axis completes the right-handed set (radial). Expressing covariances in TNW helps to separate uncertainties in the directions most relevant for conjunction analysis.

Conjunction Detection

With the data generated in the previous phases, the process advances to the identification of dangerous conjunctions. It is needed to distinguish a conjunction from a collision in this section; while a collision denotes a physical impact, a conjunction refers only to a close approach between two space objects, implying proximity without necessary interaction.

This identification is achieved by checking every pair of known objects present in a catalog to detect conjunctions. However, the computational cost of this task is too high; for a population of N objects, the number of pairs to be analysed follows the formula $N(N-1)/2$, implying a computational complexity of the order of N^2 [13]. To solve this problem, standard operations employ a filter sequence designed to reduce the possibilities into a more practical shortlist of pairs at real risk. The main methodology, established by Hoots et al. (1984) [14], utilizes three subsequent checks to exclude pairs that cannot collide based on their orbital characteristics, which is faster than propagate all the catalog searching conjunctions.

Conjunction Classical Filters The first filter is geometrical and is based on a perigee-apogee comparison. This step compares the primary object against secondary objects by defining the radial bounds of their respective orbits. Specifically, the algorithm compares the largest perigee (q) and the smallest apogee (Q) of the pair. If the difference between these values ($q - Q$) exceeds a predefined threshold distance (D), the pair is immediately discarded. This filter excludes pairs that, due to their radial separation, are geometrically unable to produce a conjunction.

The second filter refines the geometric analysis by evaluating the relative configuration of the orbits, independent of the objects' specific positions along them. This step determines the minimum distance reached in space between the two orbital paths. This concept is analogous to the Minimum Orbital Intersection Distance (MOID) used in asteroid dynamics, representing the Keplerian distance between two confocal elliptical trajectories. If this minimum geometric separation between the paths is greater than the safety threshold, the pair is safe and excluded from further analysis.

Finally, the third filter introduces the temporal dimension, often referred to as the time filter. This step is applied exclusively to the pairs that have passed the geometric filters, indicating that an orbit crossing configuration has already been confirmed. The algorithm searches for a time of coincidence, evaluating whether the two objects arrive at the crossing region simultaneously. By computing the actual distance between the objects at specific time instants within the propagation window, the filter determines if the separation falls below the critical threshold, identifying the specific pairs that present a real conjunction.

Once a pair of objects pass all the filters, the trajectories are propagated to take into account other perturbations that are neglected in the filters. If the predicted minimum distance between two objects is under a specific safety volume, the conjunction pass to the next phase, the collision probability estimation, to check if the conjunction represents a true danger to the satellite's operations.

Collision Probability Estimation

Once the conjunction identification phase has defined the possible conjunctions, the next step is quantifying the real risk. Information regarding the position and velocity of space objects is subject to uncertainties derived from observation errors, atmospheric models, and orbit propagation. Consequently, it is impossible to determine with absolute certainty if a collision will occur. Operational decision-making is based on the estimation of the Probability of Collision (PoC). This metric allows operators to evaluate if the risk exceeds a safety threshold (typically between 10^{-4} and 10^{-3} in Low Earth Orbit), and start the planning of an avoidance manoeuvre.

To compute this probability, some analytical methods have been developed to reduce the computational complexity of the problem. The most used classical approach is based on the formulation presented by Akella and Alfriend [15]. This method assumes that, during the short interval of the encounter, the relative motion of the objects is rectilinear and that position uncertainties can be represented by Gaussian distributions.

Under these hypotheses, the three-dimensional problem is reduced to a two-dimensional integration on the conjunction plane (often referred to as the B-plane), which is perpendicular to the relative velocity vector. In this plane, the probability of collision is calculated by integrating the probability density function over the circular area representing the combined radius of the two objects (Hard-Body Radius), assuming they are spherical. Although variations exist to handle complex shapes or long-duration encounters, this linearized model remains the standard for most short-term conjunctions due to its computational speed and mathematical robustness.

As an alternative to analytical approximations, particularly when the hypotheses of linearity or Gaussian distribution are not consistent, numerical methods such as Monte Carlo simulations are employed [16]. This approach requires generating a large number of random samples of the objects' initial states based on their covariance matrices and propagating each sample to the time of closest approach (TCA).

The probability of collision is estimated as the ratio of the number of cases where the minimum distance is less than the combined radius to the total number of simulations performed. While the Monte Carlo method is considered the "ground truth" for validating other algorithms and allows for working with complex force models and non-linear dynamics, its high computational cost makes it less suitable for massive and continuous studies, and it is typically reserved for detailed analysis or validation purposes.

Traditionally, the methods described above are applied by evaluating each conjunction as an isolated and independent event. However, the increasing density of objects in orbit has led to the apparition of multi-event scenarios, where a single active satellite may pass through several successive conjunctions within a relatively short time interval [17]. In these situations, analysing each risk individually is not enough, as a manoeuvre designed to avoid one collision could increase the probability of collision for a subsequent event. Therefore, there is a growing need to develop global collision probability metrics that allow for the evaluation of the aggregate risk of the entire scenario, making easier the design of optimized and efficient mitigation manoeuvres.

Risk Analysis and Collision Avoidance Manoeuvres

Once the collision probability is estimated, satellite operators must decide whether to perform a collision avoidance manoeuvre (CAM). The main objective of this phase is to determine if a Collision Avoidance Manoeuvre (CAM) is strictly necessary. This decision is subject to a trade-off between the statistical collision risk against the operational cost of the manoeuvre. Operators usually employ a specific probability threshold to trigger mitigation actions; for instance, the European Space Agency (ESA) and many other operators in Low Earth Orbit (LEO) apply a reaction threshold of 10^{-4} (1 in 10000) [18]. If the estimated collision probability (PoC) exceeds this value, a manoeuvre is planned. However, this threshold is not absolute and must be contextualized with other variables, such as the uncertainties in the state vectors, the remaining time to the Time of Closest Approach (TCA), and the subsequent consequences of the CAM for future conjunctions.

The computation of a CAM is generally formulated as a constrained optimization problem. The primary objective is to identify a trajectory modification that reduces the collision probability below the safe threshold, while simultaneously minimizing the required velocity increment (ΔV) to preserve propellant.

This optimization is sensitive to the execution epoch, performing a manoeuvre half of the orbit's period before the TCA is often most efficient for achieving the necessary radial separation. To address the computational challenges of these problems, recent methodologies have adopted convex optimization techniques, which allow for the rapid and robust determination of fuel-optimal manoeuvres even under complex non-linear constraints [19].

Furthermore, in orbits with high population density, this decision-making process presents new level of complexity: the presence of multiple consecutive conjunctions. As detailed in recent literature, optimizing a manoeuvre for a single high-risk conjunction in isolation may increase the collision probability with other secondary objects or fail to address the aggregate risk of the scenario. Consequently, a global approach to collision avoidance is required, treating the multiple encounters as a set of coupled constraints to find a solution that mitigates the primary threat without violating safety thresholds for subsequent events [20, 21].

Closing the SST Loop

The Space Surveillance and Tracking process functions as a continuous, closed-loop system. The results of the risk analysis phase, and the possible CAM executed, defines the subsequent orbital state of the object. To maintain catalog updated and validate the post-event trajectory, the system needs the acquisition of new sensor measurements. These new observations are fed back into the orbit determination algorithms to refine the state vectors and covariance matrices. This updated catalog then serves as the input for the next iteration of propagation and conjunction determination, closing the surveillance loop and restarting the cycle.

Position of This Thesis Within the SST Framework

Within the Space Surveillance and Tracking (SST) loop described above, the specific objective of this thesis, the estimation of the total probability of collision, is situated mainly within the Risk Analysis phase.

In the standard data flow, the collision probability estimation phase outputs a list of potential close approaches (CDMs). Standard Risk Analysis processes these events individually, calculating a specific Probability of Collision (PoC) for each encounter. This thesis addresses the specific sub-case of multi-encounter scenarios, where a single primary object is subject to multiple conjunctions within the prediction horizon.

Instead of outputting a vector of independent probabilities, the methodology proposed in this work integrates these events to compute a global collision probability. This global metric serves as the primary input for the subsequent Decision Making and Manoeuvre Optimization blocks. By quantifying the total risk, the system provides the optimization algorithms with a objective function that accounts for the correlations between consecutive events, rather than treating them as isolated geometric problems.

1.2. Motivation

The sustainable use of the space environment faces a significant challenge due to the fast growth of the orbital population. Currently, more than 14000 active satellites share the orbital domain with approximately 25000 cataloged debris objects. This high population, driven by the deployment of large commercial constellations and reduced launch costs, has increased the operation maintenance in Low Earth Orbit (LEO). Consequently, collision avoidance has evolved from an occasional anomaly resolution into a routine operational task.

Current Space Surveillance and Tracking (SST) operations typically analyse conjunctions as isolated events. The standard procedure involves checking the actual object catalog to detect close approaches and estimating the Probability of Collision (PoC) for each pair using analytical methods, such as the formulation by Akella and Alfriend, or numerical methods like Monte Carlo simulations. If the risk exceeds a specific threshold, a Collision Avoidance Manoeuvre (CAM) is designed to mitigate that specific risk.

However, the increasing density of objects has led to the emergence of multi-encounter scenarios, where a single satellite faces multiple conjunctions within a short time. In these complex cases, the traditional approach of evaluating and mitigating risks individually is insufficient. Optimizing a manoeuvres to avoid a primary object without considering the global context may increase the collision probability with secondary objects or generate a trajectory that violates safety margins for subsequent events.

From an economic and operational perspective, this approach presents inefficiencies. Executing independent manoeuvres for each conjunction results in high propellant consumption, a finite resource that directly limits the satellite's operational lifetime. On the other hand, global analysis enables the design of mitigation strategies that resolve multiple conflicts simultaneously through a single, optimized manoeuvre. This not only generates significant fuel savings but also reduces operator workload and minimizes mission service interruptions by reducing the frequency of necessary interventions.

Therefore, it is necessary to evolve the Risk Analysis module of the SST loop. The process requires a transition from local, single-event assessment to global risk estimation. This thesis is motivated by the need to define and calculate a total probability of collision that takes into account the risk of all consecutive encounters. By establishing this global metric, operators can evaluate the total risk to the mission and develop mitigation strategies that ensure the total risk is reduced to acceptable levels with minimal propellant cost, improving both safety and operational efficiency without losing safety.

1.3. State of the Art

This section reviews the technical foundations and current methodologies for collision risk assessment, ranging from individual conjunction detection to multi-event scenarios. As highlighted in the *ESA Annual Space Environment Report* [22], the increasing density of resident space objects demands rigorous statistical frameworks to ensure the safety of operational missions.

1.3.1. Conjunction Detection

The detection of a conjunction event is mathematically formulated by analysing the relative motion between two resident space objects. Let $\mathbf{r}_1(t), \mathbf{v}_1(t)$ and $\mathbf{r}_2(t), \mathbf{v}_2(t)$ denote the position and velocity vectors of the primary and secondary objects, respectively. The relative state vectors, $\boldsymbol{\rho}(t)$ and $\mathbf{v}_r(t)$, are defined as:

$$\boldsymbol{\rho}(t) = \mathbf{r}_2(t) - \mathbf{r}_1(t), \quad \mathbf{v}_r(t) = \mathbf{v}_2(t) - \mathbf{v}_1(t) \tag{1.1}$$

The Time of Closest Approach (TCA) is defined as the time instant t_{TCA} at which the Euclidean norm of the relative position vector, $|\boldsymbol{\rho}(t)|$, reaches its global minimum. As derived in the work of Akella and Alfriend [15], this condition is equivalent to finding the stationary point of the squared distance function $\phi(t) = \boldsymbol{\rho}(t)\boldsymbol{\rho}(t)$. Differentiating with respect to time yields the necessary condition for the closest approach:

$$\frac{d}{dt}(\boldsymbol{\rho}(t)\boldsymbol{\rho}(t)) = 2(\boldsymbol{\rho}(t)\dot{\boldsymbol{\rho}}(t)) = 2(\boldsymbol{\rho}(t)\mathbf{v}_r(t)) = 0 \tag{1.2}$$

This relationship establishes that at the exact moment of TCA, the relative position vector is orthogonal to the relative velocity vector. However, Hall et al. [23] note that for complex interactions or formation flying, the time dependence of the collision probability can exhibit multiple peaks, requiring careful analysis beyond a single instant t_{TCA}. Assuming rectilinear motion over the short duration of the encounter, the analytical solution for t_{TCA} is given by [15]:

$$t_{TCA} = -\frac{\boldsymbol{\rho}(t_0)\mathbf{v}_r(t_0)}{|\mathbf{v}_r(t_0)|^2} \tag{1.3}$$

where t_0 represents the epoch time of the initial state vectors.

1.3.2. Individual Probability Estimation

The assessment of collision risk between two resident space objects (RSOs) relies on estimating the probability that their relative trajectory enters the combined hard-body radius during a close approach. Standard procedures for this calculation are detailed in the *NASA Conjunction Assessment Handbook* [24], which provides the operational baseline for risk estimation.

Statistical Foundations and Analytical Solutions

The analysis developed in this thesis relies on fundamental concepts of probability theory, specifically centered on continuous random variables. As a reference for these definitions, *Probability and Statistics: A Course for Physicists and Engineers* by Mathai and Haubold [25] is used.

A random variable is a quantity whose value is subject to uncertainty. Among all possible distributions, the Gaussian (or normal) distribution is the standard model for orbital errors. A multivariate Gaussian variable $\mathbf{X}$ with mean vector $\boldsymbol{\mu}$ and covariance matrix $\boldsymbol{\Sigma}$ is defined by the probability density function [25, p. 242]:

$$f_{\mathbf{X}}(\mathbf{x}) = \frac{1}{\sqrt{(2\pi)^n \det(\boldsymbol{\Sigma})}} \exp\left(-\frac{1}{2}(\mathbf{x}-\boldsymbol{\mu})^{\mathrm{T}}\boldsymbol{\Sigma}^{-1}(\mathbf{x}-\boldsymbol{\mu})\right) \tag{1.4}$$

The covariance matrix $\boldsymbol{\Sigma}$ represents the dispersion of each variable as well as the correlation between them. To compute the probability of an event associated with a continuous random variable, one integrates the probability density function over the region of interest $\mathcal{D}$ in $\mathbb{R}^n$:

$$P(\mathbf{X} \in \mathcal{D}) = \int_{\mathcal{D}} f_{\mathbf{X}}(\mathbf{x})\, d\mathbf{x} \tag{1.5}$$

In the context of collision avoidance, Akella and Alfriend established that, to first order, the uncertainty component along the relative velocity direction vanishes at the Time of Closest Approach (TCA) [15]. This allows the 3D Gaussian distribution to be projected onto the conjunction plane (orthogonal to the relative velocity), reducing the problem to a 2D integration. The collision probability becomes the integral of the projected 2D Gaussian over the circular Hard Body Radius (HBR) $R = R_1 + R_2$ [15]:

$$P_c = \iint_{\xi^2+\eta^2 \leq R^2} \frac{1}{2\pi |P_\perp|^{1/2}} \exp\left(-\frac{1}{2}\begin{bmatrix}\xi-\xi_0\\ \eta-\eta_0\end{bmatrix}^{\mathsf{T}} P_\perp^{-1} \begin{bmatrix}\xi-\xi_0\\ \eta-\eta_0\end{bmatrix}\right) d\xi\, d\eta \tag{1.6}$$

where (ξ_0, η_0) are the coordinates of the projected miss distance, and $P_\perp$ is the projected covariance matrix.

Numerical Methods: Monte Carlo

Monte Carlo methods provide a practical way to estimate probabilities when an analytical expression is not available or to validate analytical developments. The method consists of generating a large number of random simulations of the system and evaluating whether the event of interest occurs in each trial.

If the event is denoted by A and n independent simulations are performed, the Monte Carlo estimator of the probability is:

$$\hat{P}(A) = \frac{1}{n} \sum_{i=1}^{n} I_i \tag{1.7}$$

where $I_i = 1$ if the event occurs in simulation i, and $I_i = 0$ otherwise. To determine the number of samples required to reach a specific precision, the bounded random sampling methods detailed by Alfano [16] are used. The Chernoff-Hoeffding bound determines the minimum number of independent random trials n required to achieve a given absolute error ϵ with a confidence level of $1 - \delta$

$$n > \frac{1}{2\epsilon^2} \ln\left(\frac{2}{\delta}\right) \tag{1.8}$$

Furthermore, if an a priori estimate of the true probability P_T is available, the required number of samples can be significantly reduced by applying the Dagum bound

$$n > \frac{4(e-2)[(1-P_T)P_T]}{\epsilon^2} \ln\left(\frac{2}{\delta}\right) \tag{1.9}$$

General guidelines for determining sample sizes in applied research are further discussed by Nanjundeswaraswamy and Divakar [26], ensuring that the statistical power of the simulation is sufficient. In the specific context of orbital dynamics, Hall et al. [27] presented a multistep computational algorithm that leverages Monte Carlo methods to validate collision probabilities in complex scenarios.

1.3.3. Collision Risk in Multi-Event Scenarios

As orbital population density increases, the probability of a satellite encountering multiple objects within a short prediction horizon grows. In these scenarios, assessing the risk of each conjunction in isolation is insufficient. To evaluate the total risk to the mission, it is necessary to extend the probabilistic framework to multiple events.

Statistical Formulation of Multiple Events

Let $A_1, A_2, \ldots, A_N$ denote N potential collision events occurring at different times $t_1, t_2, \ldots, t_N$ within the analysis window. The probability of each individual event, $P(A_i)$, is calculated using the methods described in Section 1.3.2. The basic statistics formulas (1.10), (1.11), (1.12), (1.14) and (1.15) have been obtained from the book *Probability and Statistics: A*

Course for Physicists and Engineers [25].

The total risk of collision is defined as the probability that at least one collision occurs during the interval. Mathematically, this corresponds to the probability of the union of all events:

$$P_{total} = P\left(\bigcup_{i=1}^{N} A_i\right) \tag{1.10}$$

For a general case of two events A_1 and A_2, the probability of the union is given by the fundamental identity:

$$P(A_1 \cup A_2) = P(A_1) + P(A_2) - P(A_1 \cap A_2) \tag{1.11}$$

where $P(A_1 \cap A_2)$ represents the joint probability, i.e., the probability that both events occur. Using the definition of conditional probability, the joint term can be expressed as:

$$P(A_1 \cap A_2) = P(A_1)P(A_2|A_1) \tag{1.12}$$

In the context of orbital conjunctions, where the random variables representing the state vectors are assumed to follow a multivariate Gaussian distribution, the conditional term $P(A_2|A_1)$ is governed by the properties of the conditional normal distribution.

Consider the global random vector $\mathbf{X}$ partitioned into two sub-vectors $\mathbf{X}_1$ and $\mathbf{X}_2$, corresponding to the variables of events A_1 and A_2, with mean $\boldsymbol{\mu}$ and covariance matrix $\boldsymbol{\Sigma}$ partitioned accordingly:

$$\boldsymbol{\mu} = \begin{bmatrix} \boldsymbol{\mu}_1 \\ \boldsymbol{\mu}_2 \end{bmatrix}, \quad \boldsymbol{\Sigma} = \begin{bmatrix} \boldsymbol{\Sigma}_{11} & \boldsymbol{\Sigma}_{12} \\ \boldsymbol{\Sigma}_{21} & \boldsymbol{\Sigma}_{22} \end{bmatrix} \tag{1.13}$$

If the joint distribution is Gaussian, the conditional distribution of $\mathbf{X}_2$ given $\mathbf{X}_1 = \mathbf{x}_1$ is also Gaussian. Its conditional mean $\boldsymbol{\mu}_{2|1}$ and conditional covariance $\boldsymbol{\Sigma}_{2|1}$ are given by:

$$\boldsymbol{\mu}_{2|1} = \boldsymbol{\mu}_2 + \boldsymbol{\Sigma}_{21}\boldsymbol{\Sigma}_{11}^{-1}(\mathbf{x}_1 - \boldsymbol{\mu}_1) \tag{1.14}$$

$$\boldsymbol{\Sigma}_{2|1} = \boldsymbol{\Sigma}_{22} - \boldsymbol{\Sigma}_{21}\boldsymbol{\Sigma}_{11}^{-1}\boldsymbol{\Sigma}_{12} \tag{1.15}$$

The expression for the conditional covariance $\boldsymbol{\Sigma}_{2|1}$ is mathematically equivalent to the Schur complement of the block $\boldsymbol{\Sigma}_{11}$ in the matrix $\boldsymbol{\Sigma}$ [28]. Physically, this indicates that the knowledge of the first event (fixing $\mathbf{X}_1$) reduces the uncertainty of the second event, creating a constrained covariance ellipsoid for the subsequent analysis.

Integral Definition of the Joint Probability Formally, the term $P(A_1 \cap A_2)$ represents the probability that the combined state of the system satisfies the collision conditions for both events simultaneously. Following the general theory for continuous random variables described by Mathai and Haubold [25], if we define a global state vector $\mathbf{X}$ that concatenates the random variables of the individual events, the probability of the intersection is the integral of the joint probability density function $f(\mathbf{x})$ over the intersection of the defining regions [25, p. 171]:

$$P(A_1 \cap A_2) = \iint_{\mathcal{D}_1 \cap \mathcal{D}_2} f(\mathbf{x})\, d\mathbf{x} \tag{1.16}$$

where $\mathcal{D}_1$ and $\mathcal{D}_2$ represent the subspaces in $\mathbb{R}^n$ corresponding to the collision geometries of events A_1 and A_2, respectively.

The Pearson Correlation Coefficient To explicitly model the dependency between collision events, the joint probability can be reformulated using the Pearson correlation coefficient. This approach captures the linear correlation between the binary outcomes of the events.

Let I_{A_k} be the indicator variable for event k, such that $I_{A_k} = 1$ if the collision occurs and 0 otherwise. The Pearson correlation coefficient ρ_{ij} between the two binary variables associated with events A_i and A_j is computed as [17]:

$$\rho_{ij} = \frac{\mathrm{Cov}(I_{A_i}, I_{A_j})}{\sqrt{\mathrm{Var}(I_{A_i})\,\mathrm{Var}(I_{A_j})}} \tag{1.17}$$

Using this coefficient, the joint probability can be written as the product of the independent probabilities plus an additional term that captures the correlation [17]:

$$P(A_i \cap A_j) = P(A_i)P(A_j) + \rho_{ij}\sqrt{P(A_i)(1 - P(A_i))P(A_j)(1 - P(A_j))} \tag{1.18}$$

This formulation highlights that if $\rho_{ij} = 0$ (independent events), the joint probability reduces to the simple product $P(A_i)P(A_j)$. However, in scenarios where a common uncertainty source affects multiple encounters, ρ_{ij} is non-zero, significantly influencing the total risk calculation.

Classical Probability Boundaries

To manage the ambiguity caused by the unknown correlations without falling into computationally expensive calculations, the problem is often restricted under the Fréchet-

Hoeffding bounds [29]. These inequalities provide rigorous theoretical limits for the probability of a union of events, as illustrated in Figure 1.3.

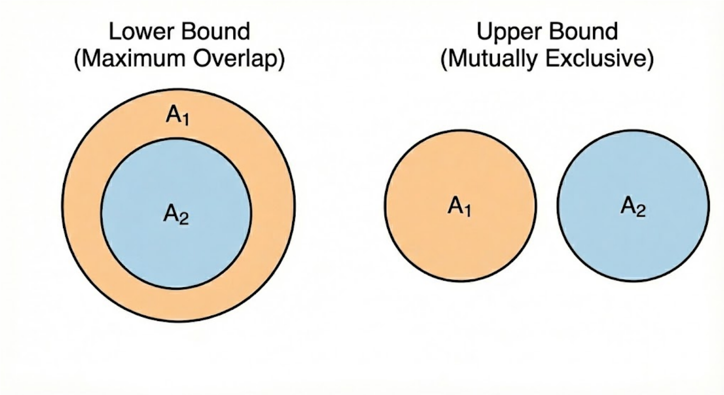

Figure 1.3: Visual representation of the Fréchet-Hoeffding bounds. **Left:** The Lower Bound (Maximum Overlap), where the risk of the smaller event is entirely contained within the larger one. **Right:** The Upper Bound (Mutually Exclusive), where the events are disjoint and risk is additive.

The Lower Bound (Maximum Overlap) The theoretical lower bound corresponds to the scenario where the collision events are maximally correlated, visualized on the left side of Figure 1.3. Mathematically, this is expressed as the maximum of the individual probabilities [17]:

$$P_{LB} = \max_{i=1}^{N}\{P(A_i)\} \leq P\left(\bigcup_{i=1}^{N} A_i\right) \tag{1.19}$$

As discussed by Garmier et al. [30], this metric is often used as a base to identify the dominant risk in a multi-encounter sequence to avoid expensive Monte Carlo trials, although it may underestimate the risk.

The Upper Bound (Mutually Exclusive) On the other hand, the upper bound corresponds to the scenario where the events are disjoint or mutually exclusive (see the right side of Figure 1.3). This is known as Boole's inequality and provides the most conservative estimate:

$$P\left(\bigcup_{i=1}^{N} A_i\right) \leq \sum_{i=1}^{N} P(A_i) = P_{UB} \tag{1.20}$$

This summation approach was formalized by Frigm et al. [31] as the "Total Probability of Collision" (TPoC), proposing it as a robust metric for finite conjunction assessment. While useful for safety-critical constraints in convex optimization [32], this simplification may produce an overestimation of the TPoC in some cases [17].

Standard Approximations and Methods

Two primary methods are dominant in the state-of-the-art for estimating the total collision probability.

The Summation Approximation (Upper Bound) A commonly used simplification assumes that collision events are mutually exclusive. For non-disjoint events, Boole's inequality states that the sum is always an upper bound:

$$P_{total} \leq \sum_{i=1}^{N} P(A_i) \tag{1.21}$$

This approximation is frequently used in maneuver optimization problems, such as those formulated by Pavanello et al. [33] and Armellin et al. [34]. In these approaches, the total risk is treated as a linear constraint in the convex optimization process, simplifying the numerical resolution.

The Product of Survival Probabilities An alternative approach assumes that the collision events are statistically independent. The total collision probability is calculated as the complement of the survival probability:

$$P_{total} \approx 1 - \prod_{i=1}^{N} (1 - P(A_i)) \tag{1.22}$$

Even though this metric is commonly used, its validity is questioned. Morris et al. [35] argue that the aggregated P_c is a theoretical estimate, not a real measure of how often collisions actually occur over time. Therefore, using it for long-term analysis can lead to misleading conclusions.

Alternative Metrics: Expected Number of Collisions

To address the limitations of probability aggregation and the saturation of P_c at unity, Hall [36] proposed the use of the statistically expected number of collisions (N_c) and the collision rate ($\dot{N}_c$). Unlike the probability of collision, which represents a Bernoulli trial outcome (collision or no-collision) and is therefore bounded by $[0, 1]$, N_c is an additive expectation value that scales linearly with the number of encounters.

Mathematical Formulation The collision rate $\dot{N}_c(t)$ is defined as the flux of probability density entering the collision volume. For a hard-body spherical collision model with combined radius R, Hall derives the rate as the surface integral of the probability density function (PDF) flux [36]:

$$\dot{N}_c(t) = \int_{\mathcal{S}} \rho(\mathbf{r}, t) \left(\mathbf{v}_{rel}(\mathbf{r}, t)\hat{\mathbf{n}}\right) d\mathcal{S} \tag{1.23}$$

where $\rho(\mathbf{r}, t)$ is the relative position PDF, $\mathbf{v}_{rel}$ is the relative velocity, and $\hat{\mathbf{n}}$ is the inward-facing normal vector of the collision sphere surface $\mathcal{S}$.

For Gaussian-distributed state errors, this integral can be approximated. The expected number of collisions N_c over a time interval $[t_0, t_f]$ is obtained by integrating the rate over time:

$$N_c = \int_{t_0}^{t_f} \dot{N}_c(t)\, dt \tag{1.24}$$

In single, high-velocity encounters (short duration), N_c is numerically equivalent to the collision probability P_c because the probability of multiple collisions in a single pass is negligible ($P_c \approx N_c$ for $N_c \ll 1$). However, in multi-event scenarios, the distinction becomes critical.

Advantages in Risk Aggregation The fundamental advantage of N_c lies in its summation properties. If a satellite faces a sequence of K encounters, the total expected number of collisions is the simple sum of the expectations for each event:

$$N_{c,total} = \sum_{k=1}^{K} N_{c,k} \tag{1.25}$$

This linearity avoids the "saturation" effect of P_c aggregation (where $\sum P_c$ can exceed 1, losing physical meaning as a probability). Hall's recent work [37] extends this to ephemeris-based calculations, introducing an algorithm that computes N_c directly from interpolated ephemerides without requiring the simplifying assumptions of linear motion often used in P_c calculations.

This metric is particularly relevant for operational thresholds. As discussed by Merz et al. [18], defining risk reduction thresholds for cumulative risk is challenging with standard probabilities due to the ambiguity of determining "acceptable" aggregated risk. The N_c metric provides a direct physical interpretation—the average number of collisions expected if the scenario were repeated many times—making it a robust metric for long-term risk accumulation and constellation management.

Sources of Correlation in Multi-Event Scenarios

The standard approximations for total risk estimation, such as the summation of probabilities (Eq. (1.21)) or the product of survival probabilities (Eq. (1.22)), assume that the collision events are statistically independent or that their correlation is negligible. However, in realistic orbital scenarios, particularly in Low Earth Orbit (LEO), this assumption may be too strong. The statistical dependence between events appears from shared sources of uncertainty that affect the state vectors of the objects involved across multiple epochs.

Two main physical mechanisms produce this correlation, linking the random variables of the encounters and invalidating the independence hypothesis:

Common Object Propagation In a multi-encounter scenario, the primary satellite is, by definition, the common element in all events. Consequently, the position error of the primary at the time of the first encounter (t_1) and at the second encounter (t_2) originates from the same initial orbit determination uncertainty at epoch t_0.

This creates a deterministic link between the events: if the primary satellite is ahead of its nominal position at t_1, it will likely be ahead at t_2 as well, governed by the state transition matrix of the orbital dynamics. In the specific case of a re-encounter with the same secondary object (e.g., after one orbital period), this coupling is further amplified, as the secondary's state error also propagates coherently between the events, leading to a condition of maximum physical correlation.

Environmental and Dynamic Model Uncertainty Beyond the initial state errors, the propagation of satellite trajectories is subject to process noise due to the dynamic model itself. In LEO, the dominant source of this uncertainty is the atmospheric drag.

As demonstrated by Casali et al.[38], errors in atmospheric density forecasts are not uncorrelated random noise but rather act as a systematic bias that affects the entire trajectory. A variation in the atmospheric density affects the drag force suffered by all objects in the scenario simultaneously. This introduces a significant cross-correlation:

- **Temporal Coupling:** The density error accumulates along the primary's track, further coupling its position errors at t_1 and t_2.
- **Inter-Object Coupling:** As noted in the *NASA Conjunction Assessment Handbook* [24], if the primary and secondary objects share similar ballistic properties and orbital regimes, they are affected by the same atmospheric density deviations. This shared environmental influence creates a statistical dependence between the

primary and the secondary objects themselves, which is often modeled using "Consider Parameters" or sensitivity vectors to account for the variance reduction (or inflation) in the relative frame.

These sources of correlation imply that the joint probability of collision $P(A_1 \cap A_2)$ is generally non equal to the product of individual probabilities, requiring the development of advanced analytical methods, such as those proposed in this thesis, to correctly quantify the total risk $P(A_1 \cup A_2)$.

1.4. Problem Statement

The State of the Art review in Section 1.3 established that while robust methods exist for estimating the risk of individual conjunctions, the standard operational approach for multi-encounter scenarios remains limited to simplified bounds or independence assumptions. This thesis addresses this specific gap by proposing an analytical framework to quantify the total collision risk in correlated scenarios.

1.4.1. Definition of the Multi-Event Scenario

Consider a mission scenario where a primary satellite (p) is subject to a sequence of potential collision events with secondary objects (s_i). We focus on the fundamental case of two events, denoted as A_1 and A_2, occurring at epochs t_1 and t_2 (with $t_1 < t_2$) within a short prediction horizon.

As defined in Section 1.3.1, each event is characterized by the relative position vector between the objects involved. Let $\mathbf{r}_p(t)$ be the state of the common primary object, and $\mathbf{r}_{s_i}(t)$ represent the state of the i-th secondary object (typically debris). The encounter geometry for the k-th event ($k \in \{1, 2\}$) is defined as:

$$\boldsymbol{\rho}_k(t_k) = \mathbf{r}_{s_k}(t_k) - \mathbf{r}_p(t_k) \tag{1.26}$$

The uncertainty in these state vectors is modeled as Gaussian, characterized by covariance matrices $\mathbf{C}_p(t)$ and $\mathbf{C}_{s_k}(t)$.

1.4.2. Formulation of the Global Risk

The objective is to compute the total probability of collision, defined as the probability that the primary satellite collides with at least one of the secondary objects during the analysis interval. Following the statistical formulation in Eq. (1.10), this corresponds to the probability of the union of the events:

$$P_{total} = P(A_1 \cup A_2) \tag{1.27}$$

Applying the fundamental inclusion-exclusion principle from probability theory (Eq. (1.11)), this can be expanded as:

$$P(A_1 \cup A_2) = P(A_1) + P(A_2) - P(A_1 \cap A_2) \tag{1.28}$$

The terms $P(A_1)$ and $P(A_2)$ represent the individual collision probabilities. These are computed independently using standard analytical methods (e.g., Akella and Alfriend [15]) as detailed in Section 1.3.2.

1.4.3. Analytical Joint Probability

The central problem addressed by this research is the determination of the joint probability term, $P(A_1 \cap A_2)$. In standard operations, this term is often neglected (Upper Bound approach) or approximated by the product $P(A_1)P(A_2)$ (independence assumption).

However, in this specific scenario, the independence assumption may introduce errors due to two primary sources of correlation:

1. **Common Primary State:** Since the same primary object is involved in both events, the error in the primary's state at t_1 is propagated to t_2.
2. **Common Dynamic Model Uncertainty:** Beyond the initial state errors, the propagator itself introduces correlations. In Low Earth Orbit (LEO), the uncertainty in the atmospheric density model and the satellite's ballistic coefficient significantly impacts the trajectory. Since the same dynamic model (and atmospheric environment) is applied to propagate the primary satellite to both t_1 and t_2, these environmental uncertainties act as a common error, coupling the random variables $\boldsymbol{\rho}_1$ and $\boldsymbol{\rho}_2$.

To solve this, we must construct a global state vector $\mathbf{X}_{global}$ that concatenates the relative states of both encounters:

$$\mathbf{X}_{global} = \begin{bmatrix} \boldsymbol{\rho}_1(t_1) \\ \boldsymbol{\rho}_2(t_2) \end{bmatrix} \tag{1.29}$$

The associated uncertainty is described by a global covariance matrix $\boldsymbol{\Sigma}_{global}$, which explicitly contains the cross-correlation terms:

$$\mathbf{\Sigma}_{global} = \begin{bmatrix} \mathbf{\Sigma}_{11} & \mathbf{\Sigma}_{12} \\ \mathbf{\Sigma}_{21} & \mathbf{\Sigma}_{22} \end{bmatrix} \tag{1.30}$$

Here, the off-diagonal block $\mathbf{\Sigma}_{12}$ captures both the propagated initial covariance and the accumulated process noise from the dynamic model (e.g., drag). The solution to the joint probability $P(A_1 \cap A_2)$ is thus defined as the integration of the multivariate joint PDF over the intersection of the collision domains:

$$P(A_1 \cap A_2) = \int_{\mathcal{D}_1 \cap \mathcal{D}_2} \mathcal{N}(\mathbf{X}_{global}; \boldsymbol{\mu}_{global}, \mathbf{\Sigma}_{global})\, d\mathbf{X}_{global} \tag{1.31}$$

1.4.4. Analysis Scenarios

To validate the proposed analytical method, this thesis will analyze specific orbital scenarios designed to isolate different sources of correlation:

1. **Common Primary with Distinct Secondaries:** The nominal multi-event scenario where the Primary object (P) encounters two different debris objects (S_1 and S_2) at different times. This analysis will focus on the sensitivity of the correlation (via the $\mathbf{\Sigma}_{12}$ block) to the size and shape of the Primary's covariance matrix. It is expected that larger shared uncertainties (e.g., degraded tracking of the primary) will induce higher correlations between the events.

2. **Repeated Encounter (Same Secondary):** A special case where the Primary (P) encounters the same Secondary object (S_1) at two different points in the orbit (e.g., t_1 and $t_2 \approx t_1 + T_{period}$). This scenario represents the condition of maximum physical correlation, as both the Primary and the Secondary propagate their respective uncertainties coherently between the two events.

3. **Influence of Common Environmental Uncertainties:** Scenarios where the correlation is driven not only by the initial state covariance but also by shared uncertainties in the dynamic model. Specifically, this considers the effect of atmospheric density errors (drag perturbations), which act as a common process noise affecting the propagation of all objects involved. This analysis aims to demonstrate how external perturbations contribute to the coupling of seemingly independent collision risks.

1.4.5. Scope and Assumptions

To limit the complexity of the problem while addressing the most critical operational needs, the scope of this thesis is defined by the following boundaries:

- **Orbital Regime (LEO):** The analysis is restricted to Low Earth Orbit (LEO) scenarios. This regime is selected because it presents the highest density of debris and is the region where atmospheric drag uncertainties play a dominant role in trajectory prediction error.
- **Two-Event Sequences ($N = 2$):** While the theoretical framework for global covariance can be extended to N events, this thesis focuses on the analytical derivation and numerical validation of pairwise multi-encounters (i.e., exactly two collision events). This allows for a detailed study of the correlation mechanisms ($\mathbf{\Sigma}_{12}$) without the computational cost of high-dimensional integration required for $N > 2$.
- **Short-Term Encounters:** The standard assumption of rectilinear motion and constant velocity during the brief duration of the conjunction (typically < 1 second) is maintained for the probability integration, consistent with the Akella and Alfriend model [15].

2 | Methodology

The previous chapter formulated the total collision risk in multi-encounter scenarios as the probability of the union of events, $P(A_1 \cup A_2)$. It established that the exact computation of this risk relies on the evaluation of the joint probability term (Eq. (1.31)), which in turn requires the construction of a global covariance matrix $\mathbf{\Sigma}_{global}$ to capture the inter-event correlations.

This chapter details the analytical and numerical framework developed to solve this problem. The methodology is structured in three main stages:

1. **Covariance Propagation and Global Matrix Construction:** Derivation of the analytical expressions for the cross-correlation block $\mathbf{\Sigma}_{12}$. This section leverages the linearized relative motion dynamics to propagate the primary satellite's uncertainty and explicitly includes the process noise contributions from the atmospheric drag model discussed in Section 1.4.4.

2. **Dimensionality Reduction:** Transformation of the high-dimensional global state vector into a standard integration domain. This step generalizes the projection method used in single-event analysis (Section 1.3.2) to the multi-event case, reducing the computational cost of the problem.

3. **Numerical Integration Strategy:** Implementation of the numerical algorithms required to compute the multivariate normal integral over the complex intersection of collision geometries.

The following sections describe each of these steps, providing the mathematical derivations necessary to transform the theoretical problem statement into a computable algorithm.

2.1. Two-Dimensional Toy Problem

2.1.1. Motivation and Overview

Before addressing the full three-dimensional collision probability problem for satellites, a simplified two-dimensional "toy problem" is introduced. The goal of this exercise is to provide an intuitive and analytical understanding of collision risks under uncertainty, while remaining simple enough to be solved and visualized explicitly.

The scenario consists of a vehicle (representing the primary satellite) moving along the y-axis with constant velocity, and two pedestrians (representing secondary objects or debris) crossing the vehicle's path. The pedestrians originate from different x-coordinates (one positive, one negative) and move parallel to the x-axis towards the y-axis.

To model the uncertainty, the initial positions of the pedestrians are treated as Gaussian random variables. Subsequent cases will introduce additional complexity, such as uncertainty in the vehicle's position or correlations between the pedestrians' motions. This development gives us a conceptual and mathematical simplification of the general 3D problem, allowing for the validation of the methodology before its generalization to orbital dynamics.

2.1.2. Problem Formulation

Four progressively complex cases are considered to isolate different sources of uncertainty and coupling effects. In all cases, the kinematic formulation follows a common structure designed to estimate the total collision probability $P(A_1 \cup A_2)$.

Kinematics and Uncertainty

The initial x-positions of the pedestrians are modelled as Gaussian random variables $X_i \sim \mathcal{N}(\mu_{X_i}, \sigma_{X_i}^2)$, where μ_{X_i} and σ_{X_i} denote the mean position and standard deviation of pedestrian i, respectively. The vehicle and pedestrians move with constant velocities v_y and $v_{x,i}$, respectively. A collision event A_i is defined as the geometric intersection of the vehicle and pedestrian i at the crossing point.

Probability Calculation

The objective is to compute the total probability of collision P_{total}. As established in the Problem Statement (Eq. (1.28)), this is given by:

$$P(A_1 \cup A_2) = P(A_1) + P(A_2) - P(A_1 \cap A_2) \tag{2.1}$$

where $P(A_i)$ are the individual collision probabilities.

The core challenge, identical to the orbital scenario, is the computation of the intersection term $P(A_1 \cap A_2)$. Depending on the case study, this term will be evaluated using the correlation framework defined in Chapter 1.3. Specifically, we will analyze the Pearson correlation coefficient ρ_{12} generated by the shared variables in the system.

The results obtained for each case will be validated against the theoretical Fréchet-Hoeffding bounds defined in Section 1.3.3:

$$\max\{P(A_1), P(A_2)\} \leq P(A_1 \cup A_2) \leq P(A_1) + P(A_2) \tag{2.2}$$

This simplified 2D framework allows for the exact analytical derivation of ρ_{12} and the joint integral, providing a benchmark for the numerical methods applied later to the 3D satellite problem.

2.1.3. Cases of Study

Case 1: Deterministic vehicle, uncertain pedestrian lateral position

The first case consists of the base problem, in which the vehicle follows a deterministic straight trajectory along the y-axis and the only source of uncertainty is the initial lateral coordinate of each pedestrian (see Figure 2.1). The two pedestrians are denoted by index $i \in \{1, 2\}$.

Let A_i denote the event "collision with pedestrian i." A possible collision is evaluated at the instant when the vehicle reaches the pedestrian's longitudinal coordinate y_i. At that moment, the relative distance between the vehicle and the corresponding pedestrian is computed and compared against a threshold that accounts for the vehicle's and pedestrian's width, similar to the Hard Body Radius (HBR) defined in the real satellite case.

It is important to remark that this definition of the event represents a simplified and relaxed version of the TCA (Time of Closest Approach) calculation, corresponding to

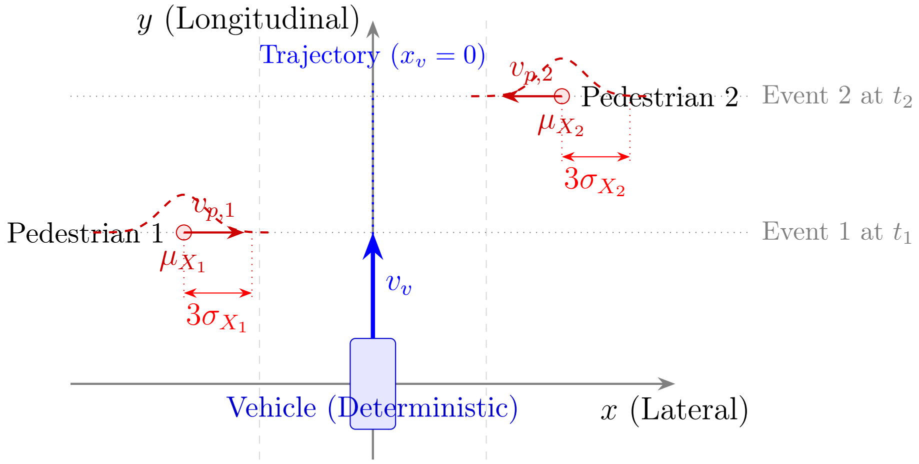

Case 1: Deterministic Vehicle, Uncertain Pedestrians

Figure 2.1: Schematic representation of Case 1. The vehicle travels deterministically along the y-axis. Pedestrians cross at different longitudinal coordinates y_i with uncertain initial lateral positions X_i.

the case where the relative velocity and position vectors are perpendicular under the assumption of that the vehicle's velocity is much higher than the pedestrian's one. This simplification permits an easier and more direct collision check.

In order to calculate these instants t_i, it is known that the vehicle departs from the origin with constant longitudinal velocity $v_v > 0$ and its longitudinal position is

$$y_v(t) = v_v t \tag{2.3}$$

The time at which the vehicle reaches the longitudinal coordinate y_i is therefore

$$t_i = \frac{y_i}{v_v} \tag{2.4}$$

To calculate this it is necessary to assume $y_i > 0$ for both pedestrians and that v_v and y_i are known. In this first case, the vehicle moves with nominal lateral coordinate

$$x_v(t) = 0 \qquad \text{(deterministic)} \tag{2.5}$$

Each pedestrian i has an uncertain initial lateral coordinate denoted by the random variable

$$X_i \sim \mathcal{N}(\mu_{X_i}, \sigma_{X_i}^2) \tag{2.6}$$

The pedestrian moves with known constant lateral velocity $v_{p,i}$ (directed toward the road). Thus the pedestrian lateral coordinate at time t is

$$x_{p,i}(t) = X_i + v_{p,i}\, t \tag{2.7}$$

Evaluating at $t = t_i$ from Eq. (2.4) yields

$$x_{p,i}(t_i) = X_i + a_i, \qquad a_i \equiv v_{p,i}\, t_i = v_{p,i}\, \frac{y_i}{v_v} \tag{2.8}$$

Let us define the relative lateral distance between pedestrian i and the vehicle at the potential collision instant as

$$Z_i \equiv x_{p,i}(t_i) - x_v(t_i) = X_i + a_i \tag{2.9}$$

which is Gaussian random variable because X_i is a Gaussian random variable. Its mean and variance are

$$\mu_{Z_i} \equiv \mathbb{E}[Z_i] = \mu_{X_i} + a_i \tag{2.10}$$

$$\sigma^2_{Z_i} \equiv \mathrm{Var}(Z_i) = \sigma^2_{X_i} \tag{2.11}$$

Let W denote the collision threshold in lateral distance (this includes the vehicle half-width and a possible safety margin). A collision with pedestrian i occurs when

$$A_i = \{\, |Z_i| < W \,\} \tag{2.12}$$

The probability of collision with pedestrian i is the integral of the probability density function (PDF) of Z_i over the collision interval $P(A_i) = \int_{-W}^{W} f_{Z_i}(z)\, dz,$, which can be particularized for a Gaussian PDF as:

$$P(A_i) = \int_{-W}^{W} \frac{1}{\sqrt{2\pi}\,\sigma_{Z_i}} \exp\left(-\frac{(z-\mu_{Z_i})^2}{2\sigma^2_{Z_i}}\right) dz = \Phi\left(\frac{W-\mu_{Z_i}}{\sigma_{Z_i}}\right) - \Phi\left(\frac{-W-\mu_{Z_i}}{\sigma_{Z_i}}\right) \tag{2.13}$$

where $\Phi(\cdot)$ is the standard normal CDF of a Gaussian distribution function with null mean and unitary sigma.

In the general case, the probability that both collisions occur is expressed as the integral of the joint bivariate normal PDF of the random variables Z_1 and Z_2 over the collision domain:

$$P(A_1 \cap A_2) = \iint_{\mathcal{D}} f(z_1, z_2)\, dz_1\, dz_2 \tag{2.14}$$

where the integration domain $\mathcal{D}$ is defined by the lateral limits of both collisions:

$$\mathcal{D} = \{(z_1, z_2) \mid |z_1| < W,\ |z_2| < W\} \tag{2.15}$$

The joint bivariate normal density with correlation coefficient $\rho_{Z_1Z_2}$ is given by

$$f(z_1, z_2) = \frac{\exp(-\frac{1}{2}(\mathbf{z} - \boldsymbol{\mu}_Z)^\top \boldsymbol{\Sigma}_Z^{-1}(\mathbf{z} - \boldsymbol{\mu}_Z)))}{2\pi\, |\boldsymbol{\Sigma}_z|^{1/2}} \tag{2.16}$$

$$\mathbf{z} = \begin{bmatrix} z_1 \\ z_2 \end{bmatrix}, \boldsymbol{\mu}_z = \begin{bmatrix} \mu_{Z_1} \\ \mu_{Z_2} \end{bmatrix}, \Sigma_z = \begin{bmatrix} \sigma_{Z_1}^2 & \rho_{Z_1Z_2}\, \sigma_{Z_1}\sigma_{Z_2} \\ \rho_{Z_1Z_2}\, \sigma_{Z_1}\sigma_{Z_2} & \sigma_{Z_2}^2 \end{bmatrix} \tag{2.17}$$

In this case, the pedestrians are modelled as independent objects, and the vehicle is deterministic. Therefore, the random variables corresponding to the relative lateral distances at the time of each collision i are uncorrelated and the covariance term of the Pearson's coefficient vanishes:

$$\rho_{Z_1Z_2} = \frac{\mathrm{Cov}(Z_1, Z_2)}{\sigma_{Z_1}\sigma_{Z_2}} = 0 \tag{2.18}$$

Substituting $\rho_{Z_1Z_2} = 0$ into Eq. (2.16), the joint PDF yields

$$f(z_1, z_2) = \frac{1}{2\pi\, \sigma_{Z_1}\sigma_{Z_2}} \exp\left[-\frac{1}{2}\left(\frac{(z_1 - \mu_{Z_1})^2}{\sigma_{Z_1}^2} + \frac{(z_2 - \mu_{Z_2})^2}{\sigma_{Z_2}^2}\right)\right] \tag{2.19}$$

And can be factorized as

$$f(z_1, z_2) = f_{Z_1}(z_1)\, f_{Z_2}(z_2) \tag{2.20}$$

which allows the double integral in Eq. (2.14) to be separated into two independent one-dimensional integrals:

$$P(A_1 \cap A_2) = \left(\int_{-W}^{W} f_{Z_1}(z_1)\, dz_1\right)\left(\int_{-W}^{W} f_{Z_2}(z_2)\, dz_2\right) = P(A_1)\, P(A_2) \tag{2.21}$$

Finally, the total probability of collision of the car with any pedestrian is calculated as

$$P(A_1 \cup A_2) = P(A_1) + P(A_2) - P(A_1)\, P(A_2) \tag{2.22}$$

This case represents the most simple and intuitive situation, when both events are actually independent and the analytical solution is simple.

Case 2: Adding uncertainty to the vehicle position

In this second case, uncertainty is also introduced in the x-position of the vehicle. The relative position between the vehicle and each pedestrian at the time of each collision is then a Gaussian random variable derived from the difference between two normal distributions. This couples the two events. See Figure 2.2.

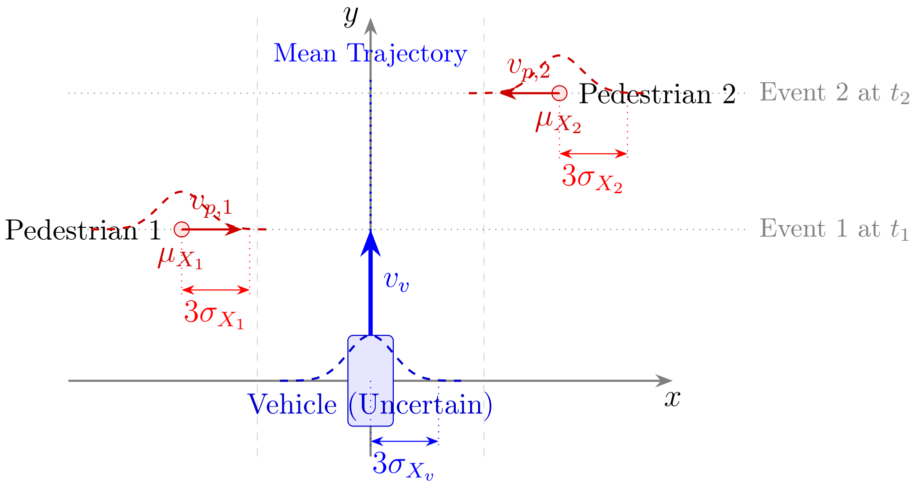

Figure 2.2: Schematic representation of Case 2. The vehicle now has an uncertain initial lateral position X_v (blue variance), which couples the probability of the two events.

Following a similar derivation as in Case 2.1.3, the times of the event evaluation do not change their expression, as the y-coordinates remain deterministic and known. Consequently, these times can be obtained from Eq. (2.4).

Each object has now an uncertain initial lateral coordinate denoted by the random variables

$$X_i \sim \mathcal{N}(\mu_{X_i}, \sigma^2_{X_i}), \qquad X_v \sim \mathcal{N}(\mu_{X_v}, \sigma^2_{X_v}). \tag{2.23}$$

The kinematics of the pedestrian remain as in Case 2.1.3. Consequently, the relative distance between the pedestrian i and the vehicle at t_i is

$$Z_i \equiv x_{p,i}(t_i) - x_v(t_i) = X_i + a_i - X_v, \tag{2.24}$$

which is a Gaussian random variable because X_i and X_v are Gaussian random variables too. Its mean and variance are

$$\mu_{Z_i} \equiv \mathbb{E}[Z_i] = \mu_{X_i} + a_i - \mu_{X_v}, \tag{2.25}$$

$$\sigma^2_{Z_i} \equiv \mathrm{Var}(Z_i) = \sigma^2_{X_i} + \sigma^2_{X_v}. \tag{2.26}$$

The calculation of the individual probability of collision remains as in Case 2.1.3, following Eq. (2.13). The same does not hold for the multiple collision probability, due to the correlation between the events introduced. Now, the correlation between the variables yields

$$\mathrm{Cov}(Z_1, Z_2) = \mathrm{Cov}(X_1, X_2) + \mathrm{Cov}(X_v, X_v) - \mathrm{Cov}(X_1, X_v) - \mathrm{Cov}(X_2, X_v) = \sigma^2_{X_v} \tag{2.27}$$

knowing that both pedestrians and the vehicle are totally independent.

Consequently, the Pearson's correlation coefficient (Eq. (1.17)) is non-zero, and the factorization of the joint bivariate normal PDF changes, modifying the multiple collision probability formula. The joint probability density of the two events is therefore given by Eq. (2.16) where $\rho_{Z_1Z_2} = \sigma^2_{X_v}/(\sigma_{Z_1}\sigma_{Z_2})$ is the correlation coefficient between Z_1 and Z_2, do not confuse this with the correlation coefficient between events $\rho_{A_1A_2}$ used to define the correlation coefficient, they are two different concepts.

Then, the probability of a simultaneous collision between the vehicle and both pedestrians can be written as the double integral of the 2D PDF over the collision domains,

$$P(A_1 \cap A_2) = \iint_{\mathcal{D}} f(z_1, z_2)\, dz_1\, dz_2 \tag{2.28}$$

where $f(z_1, z_2)$ is the bivariate normal PDF developed from Eq. (2.16).

$$f(z_1, z_2) = \frac{\exp\left[-\frac{1}{2(1-\rho^2_{Z_1Z_2})}\left(\frac{(z_1-\mu_{Z_1})^2}{\sigma^2_{Z_1}} + \frac{(z_2-\mu_{Z_2})^2}{\sigma^2_{Z_2}} - \frac{2\rho_{Z_1Z_2}(z_1-\mu_{Z_1})(z_2-\mu_{Z_2})}{\sigma_{Z_1}\sigma_{Z_2}}\right)\right]}{2\pi\, \sigma_{Z_1}\sigma_{Z_2}\sqrt{1-\rho^2_{Z_1Z_2}}} \tag{2.29}$$

which explicitly takes into account the dependence between both events introduced by the vehicle position uncertainty.

This general expression can be factorized as

$$f_{Z_1,Z_2}(z_1, z_2) = f_{Z_1}(z_1)\, f_{Z_2|Z_1}(z_2 \mid z_1) \tag{2.30}$$

where the marginal and conditional densities are

$$f_{Z_1}(z_1) = \frac{1}{\sqrt{2\pi}\,\sigma_{Z_1}} \exp\left(-\frac{(z_1-\mu_{Z_1})^2}{2\sigma_{Z_1}^2}\right) \tag{2.31}$$

$$f_{Z_2|Z_1}(z_2 \mid z_1) = \frac{1}{\sqrt{2\pi}\,\sigma_{Z_2|Z_1}} \exp\left(-\frac{(z_2-\mu_{Z_2|Z_1})^2}{2\sigma_{Z_2|Z_1}^2}\right) \tag{2.32}$$

with the usual conditional moments for the Gaussian:

$$\mu_{Z_2|Z_1} \equiv \mu_{Z_2} + \rho_{Z_1Z_2}\frac{\sigma_{Z_2}}{\sigma_{Z_1}}(z_1-\mu_{Z_1}), \qquad \sigma_{Z_2|Z_1}^2 \equiv \sigma_{Z_2}^2(1-\rho_{Z_1Z_2}^2) \tag{2.33}$$

Note that this factorization clearly shows the effect of correlation. In the uncorrelated case of Section 2.1.3, where $\rho_{Z_1Z_2} = 0$, the conditional term reduces to the marginal one, $f_{Z_2|Z_1}(z_2 \mid z_1) = f_{Z_2}(z_2)$, and therefore the joint density factorizes as the product of independent PDFs. Consequently, the intersection probability simplifies to the well-known expression $P(A_1 \cap A_2) = P(A_1)\,P(A_2)$.

In the present correlated scenario, however, this simplification no longer holds. The probability of the intersection is not simply the product of the individual probabilities, $P(A_1 \cap A_2) \neq P(A_1)\,P(A_2)$, but instead $P(A_1 \cap A_2) = P(A_1)\,P(A_2 \mid A_1)$, since the dependence between the events must be taken into account.

This effect depends on the correlation level between the possible events, given by the uncertainty introduced by the vehicle. The numerical results depicted in Section 3.1.1 illustrate this behaviour, increasing the correlation while the variance of the vehicle increases and gets closer to the pedestrian's variances, or even beyond those.

Case 3: Single pedestrian crossing twice

The third case replaces the two independent pedestrians by a single pedestrian that crosses the road twice. To simplify the calculations, the uncertain object (the pedestrian) will follow a straight trajectory along the x-direction, and the vehicle (totally deterministic) will follow an inverted U-shaped trajectory, intersecting the pedestrian twice (see Figure 2.3). This scenario represents a particular case of multiple encounter that appears when the primary and the secondary objects have orbits with coincidents points and compatible periods. This situation represents a potentially expensive, in terms of fuel consumption, sequence of avoidance maneouvres that could be solved with only one.

Although the vehicle's parameters remains similar to Case 2.1.3, the correlation between the two potential collisions must now be calculated again. This case allows investigating

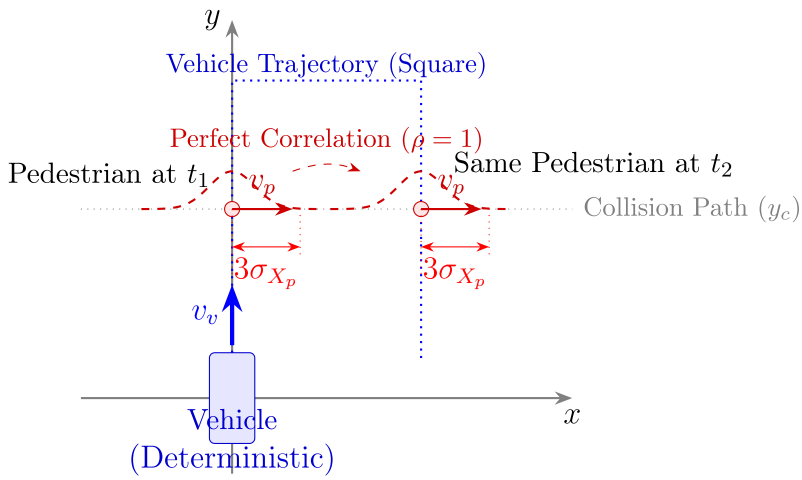

Case 3: Deterministic Vehicle, Single Pedestrian (Repeated)

Figure 2.3: Schematic representation of Case 3. The deterministic vehicle performs a square-shaped trajectory, intersecting the *same* pedestrian twice. Since the pedestrian's error X_p is identical for both events, the correlation is perfect ($\rho = 1$).

how repeated crossings affect the global collision probability.

Now, even if when the pedestrian is the same in both events, the crossing point of each event is different, and consequently their times of closest approach.

The derivation of the problem is similar to the Case 2.1.3, the car position follows a function that simulates the path depicted before $x_v(t)$, and with this function the event times t_i can be easily obtained.

For each collision, the pedestrian is the same, so there is only one random variable

$$X_p \sim \mathcal{N}(\mu_{X_p}, \sigma^2_{X_p}) \tag{2.34}$$

Let us define the relative lateral distance between pedestrian at time t_i and the vehicle at the potential collision instant as

$$Z_i \equiv x_p(t_i) - x_v(t_i) = X_p + a_i - x_v(t_i) \tag{2.35}$$

which is a Gaussian random variable because X_p is a Gaussian random variable too. Its mean and variance are

$$\mu_{Z_i} \equiv \mathbb{E}[Z_i] = \mu_{X_p} + a_i - x_v(t_i) \tag{2.36}$$

$$\sigma^2_{Z_i} \equiv \mathrm{Var}(Z_i) = \sigma^2_{X_p} \tag{2.37}$$

The calculation of the individual probability of collision remains as in Case 2.1.3, following Eq. (2.13). The same does not hold for the multiple collision probability. Now, the correlation between the events yields

$$\mathrm{Cov}(Z_1, Z_2) = \mathrm{Cov}(X_p, X_p) = \sigma^2_{X_p} \tag{2.38}$$

knowing that the car position is deterministic, and the pedestrian is the same for both events.

This yields $\rho_{Z_1 Z_2} = \sigma^2_{X_p}/(\sigma_{Z_1}\sigma_{Z_2}) = 1$, the correlation coefficient between Z_1 and Z_2. As this coefficient is non-zero, the joint probability of collision must be obtained from Eq. (2.28), and, as in Case 2.1.3, it cannot be factorized as the simple product of the individual collision probabilities.

Using the factorization introduced in Section 2.1.3, $f_{Z_1,Z_2}(z_1, z_2) = f_{Z_1}(z_1)\, f_{Z_2|Z_1}(z_2 \mid z_1)$, one can now examine the limit $\rho_{Z_1 Z_2} \to 1$. In this limit, the conditional variance collapses:

$$\sigma^2_{Z_2|Z_1} = \sigma^2_{Z_2}(1 - \rho^2_{Z_1 Z_2}) \longrightarrow 0 \tag{2.39}$$

and the conditional density becomes a Dirac delta along the line

$$z_2 = \mu_{Z_2|Z_1} = \mu_{Z_2} + \frac{\sigma_{Z_2}}{\sigma_{Z_1}}(z_1 - \mu_{Z_1}) \tag{2.40}$$

so that for each value of z_1 there exists a single corresponding value of z_2. Consequently, the joint PDF reduces to

$$f_{Z_1,Z_2}(z_1, z_2) = f_{Z_1}(z_1)\, \delta\Big(z_2 - \mu_{Z_2} - \frac{\sigma_{Z_2}}{\sigma_{Z_1}}(z_1 - \mu_{Z_1})\Big) \tag{2.41}$$

which clearly reflects the perfect correlation between the two variables.

The joint probability of collision can be expressed as a single integral over the subset of values of Z_1 that simultaneously satisfy the collision conditions for both events:

$$P(A_1 \cap A_2) = \int_{\mathcal{D}_1^{\mathrm{eff}}} f_{Z_1}(z_1)\, dz_1, \tag{2.42}$$

where $\mathcal{D}_1^{\mathrm{eff}}$ denotes the set of values of z_1 for which the corresponding z_2 also lies within the collision domain defined in Eq. (2.15).

This formulation emphasizes that, under perfect correlation, the joint probability is fully determined by the marginal distribution of Z_1, and the two collision events are no longer independent. The integration reduces the two-dimensional problem to a one-dimensional one along the line defined by the correlation.

Finally, comparing the result with the previous cases, one can clearly determine the effect of correlation on the joint collision probability. In the uncorrelated case ($\rho = 0$, see Section 2.1.3), the events are independent and $P(A_1 \cap A_2) = P(A_1)\, P(A_2)$. In the general correlated case ($0 < \rho < 1$, see Section 2.1.3), the correlation must be taken into account, and the joint probability is obtained from the conditional factorization of the bivariate normal PDF. Finally, in the limit of perfect correlation ($\rho = 1$), the two events are fully dependent and the joint probability is entirely determined by the marginal of one variable. This illustrates how increasing correlation changes the problem from independence to full dependence, affecting both the expression and its evaluation.

Case 4: Deterministic vehicle, correlated pedestrians

In this case, the vehicle follows the same deterministic trajectory as in Case 2.1.3, while the initial lateral positions of the two pedestrians are now correlated. This case represents the external factors that modifies the behaviour of the objects in a similar way, inducing a correlation between them (for example, the atmospheric drag in the case of satellites in space).

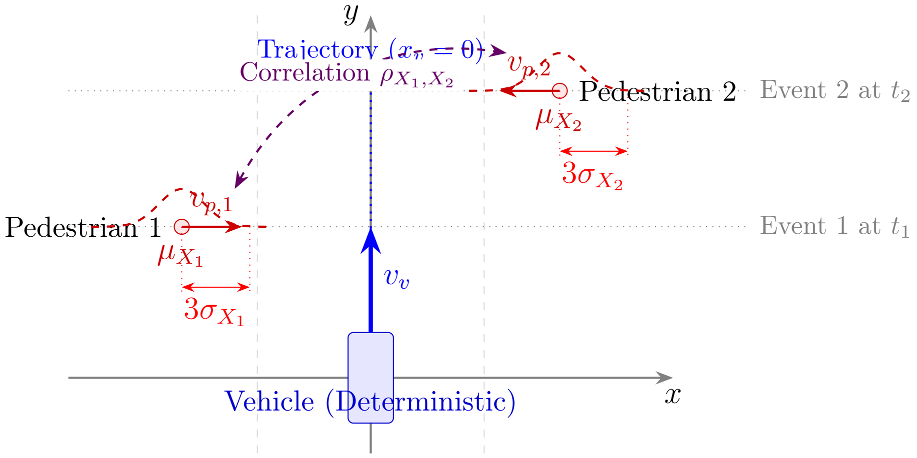

Case 4: Deterministic Vehicle, Correlated Pedestrians

Figure 2.4: Schematic representation of Case 4. The vehicle is deterministic, but the initial positions of the two pedestrians are statistically correlated, linking the two events.

Let the two pedestrians be denoted by $i \in \{1, 2\}$. The initial lateral positions of the pedestrians are modelled as Gaussian random variables

$$\mathbf{X} = \begin{pmatrix} X_1 \\ X_2 \end{pmatrix} \sim \mathcal{N}(\boldsymbol{\mu}_X, \Sigma_X) \tag{2.43}$$

with mean vector $\boldsymbol{\mu}_X = (\mu_{X_1}, \mu_{X_2})^\top$ and covariance matrix

$$\Sigma_X = \begin{pmatrix} \sigma^2_{X_1} & \rho_{X_1,X_2}\,\sigma_{X_1}\sigma_{X_2} \\ \rho_{X_1,X_2}\,\sigma_{X_1}\sigma_{X_2} & \sigma^2_{X_2} \end{pmatrix} \tag{2.44}$$

where ρ_{X_1,X_2} is the correlation coefficient between the pedestrians' lateral positions.

To obtain samples of the pedestrians' positions at the potential collision instants, the sample X_1 can be generated first as usual, using the general random variable,

$$X_1 = x \sim \mathcal{N}\Big(\mu_{X_1},\ \sigma^2_{X_1}\Big) \tag{2.45}$$

and then generate X_2 conditionally using the conditional mean and variance derived in Eq. (2.33),

$$X_2 \mid X_1 = x_2 \sim \mathcal{N}\Big(\mu_{X_2} + \rho_{X_1,X_2}\frac{\sigma_{X_2}}{\sigma_{X_1}}(x_1 - \mu_{X_1}),\ \sigma^2_{X_2}(1 - \rho^2_{X_1,X_2})\Big) \tag{2.46}$$

which can be reduced to a normal Gaussian distribution when no correlation exists.

As in Case 2.1.3, the vehicle is deterministic and its lateral position is given by Eq. (2.5), while the pedestrians move laterally according to Eq. (2.8). Hence, the relative lateral distances at the potential collision instants are

$$Z_i = X_i + a_i, \qquad a_i = v_{p,i}t_i \tag{2.47}$$

which is Gaussian random variable because X_i is a Gaussian random variable. Its mean and variance are

$$\mu_{Z_i} \equiv \mathbb{E}[Z_i] = \mu_{X_i} + a_i \tag{2.48}$$

$$\sigma^2_{Z_i} \equiv \mathrm{Var}(Z_i) = \sigma^2_{X_i} \tag{2.49}$$

The collision events A_i and the corresponding lateral threshold W are defined as in Eqs. (2.12) and (2.13). The joint probability of collision of both pedestrians is obtained from the integral of the bivariate Gaussian PDF in Eq. (2.16) where Σ_Z has the same covariance structure as in Eq. (2.44) due to

$$\mathrm{Cov}(Z_1, Z_2) = \rho_{X_1,X_2}\sigma_{X_1}\sigma_{X_1} \tag{2.50}$$

As the correlation between the pedestrian is not negligible in this case, the final expression for the PDF is:

$$f(z_1, z_2) = \frac{\exp\left[-\frac{1}{2(1-\rho^2_{X_1X_2})}\left(\frac{(z_1-\mu_{Z_1})^2}{\sigma^2_{Z_1}} + \frac{(z_2-\mu_{Z_2})^2}{\sigma^2_{Z_2}} - \frac{2\rho_{X_1X_2}(z_1-\mu_{Z_1})(z_2-\mu_{Z_2})}{\sigma_{Z_1}\sigma_{Z_2}}\right)\right]}{2\pi\,\sigma_{Z_1}\sigma_{Z_2}\sqrt{1-\rho^2_{X_1X_2}}} \tag{2.51}$$

which has to be factorized as in Eq. (2.30).

The total probability of collision with any pedestrian remains as

$$P(A_1 \cup A_2) = P(A_1) + P(A_2) - P(A_1 \cap A_2) \tag{2.52}$$

where $P(A_1)$ and $P(A_2)$ are computed as in Case 2.1.3 and $P(A_1 \cap A_2)$ uses the correlated bivariate PDF.

This case represent a new correlation source that is completely compatible with the first cases source, the uncertainty of the vehicle. In this section both sources has been isolated to understand their effects independently. However, in a more realistic case, they may appear together, but the derivation of the expressions do not change with respect to this last case, one only have to take into account the vehicle uncertainty for the definition of the random variables $Z_i = x_{p,i}(t_i) - x_v(t_i)$ and for the covariance between events $\mathrm{Cov}(Z_1, Z_2) = \sigma^2_{X_v} + \rho_{X_1X_2}\,\sigma_{X_1}\,\sigma_{X_2}$.

Case 5: Uncertain vehicle and environmental disturbance (Wind model)

In this final case, a new source of uncertainty is introduced that acts dynamically on the objects during their motion, rather than being solely an initial state error. This external factor is modelled as a "wind" field W that perturbs the trajectories of both the vehicle and the pedestrians. This represents a physical analogy to environmental perturbations in LEO, such as atmospheric drag, which affect the propagation of all objects involved in the scenario.

Let the wind intensity be modelled as a Gaussian random variable $W \sim \mathcal{N}(\mu_W, \sigma^2_W)$. In addition to this, the vehicle retains its initial position uncertainty as in Case 2.1.3, while

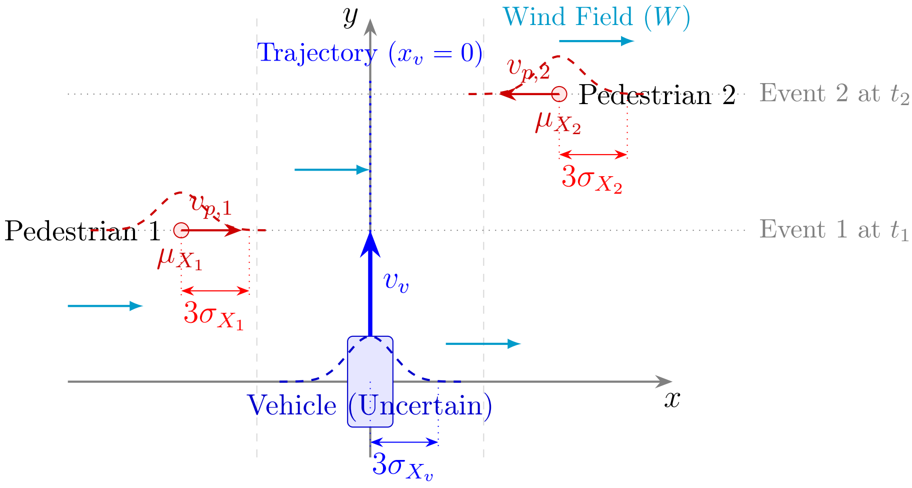

Case 5: Uncertain Vehicle + Environmental Disturbance

Figure 2.5: Schematic representation of Case 5. In addition to the vehicle's initial uncertainty (σ_{X_v}), a common environmental disturbance ("Wind", W) affects all objects, creating a complex correlation structure.

the pedestrians' initial positions are modelled as independent Gaussian variables.

The kinematics of the objects are now coupled to this environmental factor through specific sensitivity coefficients α. The position of the vehicle and the pedestrian i at time t is given by:

$$x_v(t) = X_v + v_v t + \alpha_v W t \tag{2.53}$$

$$x_{p,i}(t) = X_i + v_{p,i} t + \alpha_{p,i} W t \tag{2.54}$$

where α_v and $\alpha_{p,i}$ represent the susceptibility of the vehicle and the pedestrian to the wind (analogous to the ballistic coefficient in satellite dynamics).

The relative lateral distance at the collision instant t_i is derived as the difference between the pedestrian's and the vehicle's position:

$$Z_i = x_{p,i}(t_i) - x_v(t_i) = (X_i + v_{p,i} t_i + \alpha_{p,i} W t_i) - (X_v + v_v t_i + \alpha_v W t_i) \tag{2.55}$$

Grouping the deterministic and stochastic terms, and defining the effective wind coupling coefficient for event i as $k_i = (\alpha_{p,i} - \alpha_v) t_i$:

$$Z_i = X_i - X_v + k_i W + a_i \tag{2.56}$$

Since Z_i is a linear combination of independent Gaussian variables (X_i, X_v, W), it remains a Gaussian random variable. Its mean and variance are:

$$\mu_{Z_i} \equiv \mathbb{E}[Z_i] = \mu_{X_i} - \mu_{X_v} + k_i\mu_W + a_i \tag{2.57}$$

$$\sigma^2_{Z_i} \equiv \mathrm{Var}(Z_i) = \sigma^2_{X_i} + \sigma^2_{X_v} + k_i^2\sigma^2_W \tag{2.58}$$

The collision events A_i and the individual probabilities are computed using these updated moments as in previous cases. However, the critical impact of the wind model appears in the joint probability $P(A_1 \cap A_2)$. The covariance between the two events now contains two sources of correlation: the common vehicle error (X_v) and the common environmental noise (W).

$$\mathrm{Cov}(Z_1, Z_2) = \mathrm{Cov}(X_1 - X_v + k_1W, X_2 - X_v + k_2W) \tag{2.59}$$

Since X_1 and X_2 are independent, their cross-terms vanish. The remaining shared terms yield:

$$\mathrm{Cov}(Z_1, Z_2) = \sigma^2_{X_v} + k_1k_2\sigma^2_W \tag{2.60}$$

Substituting the definition of k_i, the explicit dependence on the environmental parameters is:

$$\mathrm{Cov}(Z_1, Z_2) = \sigma^2_{X_v} + (\alpha_{p,1} - \alpha_v)(\alpha_{p,2} - \alpha_v)t_1t_2\sigma^2_W \tag{2.61}$$

This result demonstrates that even if the initial state uncertainty of the vehicle (σ_{X_v}) is small, a significant environmental uncertainty (σ_W) can induce a strong correlation between the events, especially for events occurring later in time (dependence on t_1t_2).

The joint probability density function $f(z_1, z_2)$ governing the two collision events is the bivariate Gaussian distribution defined by the moments derived above. Substituting the specific correlation coefficient for this case, $\rho_{Z_1Z_2} = (\sigma^2_{X_v} + k_1k_2\sigma^2_W)/(\sigma_{Z_1}\sigma_{Z_2})$, the PDF is given by:

$$f(z_1, z_2) = \frac{\exp\left[-\frac{1}{2(1-\rho^2_{Z_1Z_2})}\left(\frac{(z_1-\mu_{Z_1})^2}{\sigma^2_{Z_1}} + \frac{(z_2-\mu_{Z_2})^2}{\sigma^2_{Z_2}} - \frac{2\rho_{Z_1Z_2}(z_1-\mu_{Z_1})(z_2-\mu_{Z_2})}{\sigma_{Z_1}\sigma_{Z_2}}\right)\right]}{2\pi\sigma_{Z_1}\sigma_{Z_2}\sqrt{1-\rho^2_{Z_1Z_2}}} \tag{2.62}$$

Finally, the joint probability of collision $P(A_1 \cap A_2)$ is obtained by integrating this function over the collision domain $\mathcal{D}$ defined by W:

$$P(A_1 \cap A_2) = \int_{-W}^{W}\int_{-W}^{W} f(z_1, z_2)\, dz_1\, dz_2 \tag{2.63}$$

This integral has to be factorized as in Eq. (2.30).

2.2. Multi-encounter collision probability method

Once the study of the "toy problem" has been completed, the extension to the three-dimensional problem will be developed step by step, while maintaining the typical assumptions regarding orbital conjunctions in space involving satellites (i.e., velocities are approximately constant during the event and their uncertainties are negligible compared to positional uncertainties). To avoid notational issues (change in the objects' names, from vehicle and pedestrians, to primary and secondary), the 3D extension will be developed in several steps, with each step explained in detail.

2.2.1. Objects' Initial State

Firstly, the objects' initial positions must be defined. Each object is represented by a normal (Gaussian) distribution. In 1D, this corresponds to a scalar random variable, while in 3D it extends to a multivariate normal distribution. In both cases, the initial velocities are considered deterministic.

It is necessary to define the state vector for the 3D case, which is needed for the correct propagation of the position and velocity.

1D	**3D**	
Object initial position:	Object initial position:	Object state vector:
$X_v \sim \mathcal{N}(\mu_v, \sigma_v^2)$	$\mathbf{X}_p \sim \mathcal{N}_3(\boldsymbol{\mu}_p, \boldsymbol{\Sigma}_p)$	$\mathbf{Y}_p = (\mathbf{X}_p^\top, \mathbf{v}_p^\top)^\top$
$X_{pi} \sim \mathcal{N}(\mu_{pi}, \sigma_{pi}^2)$	$\mathbf{X}_{si} \sim \mathcal{N}_3(\boldsymbol{\mu}_{si}, \boldsymbol{\Sigma}_{si})$	$\mathbf{Y}_{si} = (\mathbf{X}_{si}^\top, \mathbf{v}_{si}^\top)^\top$

2.2.2. Displacements

Next, the displacement of each object is modelled by assuming linear motion with constant velocity in 1D. However, for the full 3D scenario, this assumption is no longer valid. Instead, the states of the primary object and both secondary objects must be propagated from their initial epoch using a full orbital dynamics model, represented by the propagation function $\mathbf{y}(t) = \varphi(\mathbf{Y}, t_0; t)$, where $\mathbf{Y}$ and $\mathbf{y}(t)$ are the state vectors that contain the position and velocity at times t_0 and t, respectively. Around this propagated state, the motion could be considered linear for small temporal variations.

1D	3D
$x_v(t) = X_v + v_v t$	$\mathbf{y}_p(t) = \varphi(\mathbf{Y}_p, t_0; t)$; $\mathbf{x}_p(t_i + \Delta t) \approx \mathbf{x}_p(t_i) + \mathbf{v}_p(t_i)\Delta t$
$x_{pi}(t) = X_{pi} + v_{pi} t$	$\mathbf{y}_{si}(t) = \varphi(\mathbf{Y}_{si}, t_0; t)$; $\mathbf{x}_{si}(t_i + \Delta t) \approx \mathbf{x}_{si}(t_i) + \mathbf{v}_{si}(t_i)\Delta t$

2.2.3. Conjunction Times

When the motion has been defined, the Time of Closest Approach (TCA) can be determined. In 1D, the intersection has been defined when the vehicle reaches the vertical position of the pedestrian, taking into account that the velocity of the vehicle is much higher than that of the pedestrian. In 3D, this corresponds to minimizing the relative distance between the objects' trajectories.

1D	3D
$t_i = \frac{y_{pi}}{v_v}$	TCA: $t_i := \{t \in \mathbb{R} \mid \boldsymbol{\rho}(t)\boldsymbol{\nu}(t) = 0\}$ where $\boldsymbol{\rho}(t) = \mathbf{x}_{si}(t) - \mathbf{x}_p(t)$ and $\boldsymbol{\nu}(t) = \mathbf{v}_{si}(t) - \mathbf{v}_p(t)$

2.2.4. Relative Position Distribution

Now, the relative position at conjunction is defined as a random variable obtained by subtracting the two random position vectors. The result is again Gaussian, with a mean equal to the difference of the means, and a covariance equal to the sum of the covariances in the simplified 1D case, as the vehicle and the pedestrian are independent. For the real 3D problem, however, the mean state must be propagated from the initial mean state, and the resulting covariance is no longer just the sum of the initial covariances. Instead, both covariances must be propagated to account for all external factors that could introduce correlations between the events, such as atmospheric drag, which has a strong influence in the LEO regime.

1D	3D
$Z_i = x_{pi}(t_i) - x_v(t_i)$	$\mathbf{Z}_i = \boldsymbol{\rho}(t_i)$
$Z_i \sim \mathcal{N}(\mu_{Z_i}, \sigma^2_{Z_i})$	$\mathbf{Z}_i \sim \mathcal{N}_3(\boldsymbol{\mu}_{Z_i}, \boldsymbol{\Sigma}_{Z_i})$
$\mu_{Z_i} = \mu_{pi} + v_{pi} t_i - \mu_v$	$\boldsymbol{\mu}_{Z_i} = \boldsymbol{\mu}_{si}(t_i) - \boldsymbol{\mu}_p(t_i)$
$\sigma^2_{Z_i} = \sigma^2_{pi} + \sigma^2_v$	$\boldsymbol{\Sigma}_{Z_i} = \boldsymbol{\Sigma}_{si}(t_i) + \boldsymbol{\Sigma}_p(t_i)$

2.2.5. Event Definition

Once the relative positions are defined, the event A_i is defined based on proximity thresholds in one and three dimensions. In 1D, the event occurs when the lateral distance is smaller than the vehicle half-width, while in 3D, it occurs when the relative distance between the two objects is smaller than their combined hard-body radius.

1D	**3D**
$A_i : \lvert Z_i \rvert < W$	$A_i : \lVert \mathbf{Z}_i \rVert < R = R_p + R_{si}$

2.2.6. Event Probability

In the 1D case, the probability corresponds to the integral of the Gaussian distribution of Z_i over the interval defined by the vehicle width:

1D	**3D**
$P(A_i) = \int_{-W}^{W} f(z_i)\, dz_i$	$P(A_i) = \iiint_{\lVert \mathbf{z}_i \rVert < R} f(\mathbf{z}_i)\, d\mathbf{z}_i$
$f(z_i) = \frac{1}{\sqrt{2\pi}\,\sigma_{Z_i}} \exp\left(-\frac{(z_i-\mu_{Z_i})^2}{2\sigma_{Z_i}^2}\right)$	$f(\mathbf{z}_i) = \frac{\exp\left(-\frac{1}{2}(\mathbf{z}_i-\boldsymbol{\mu}_{Z_i})^\top \boldsymbol{\Sigma}_{Z_i}^{-1}(\mathbf{z}_i-\boldsymbol{\mu}_{Z_i})\right)}{(2\pi)^{3/2}\,\lvert \boldsymbol{\Sigma}_{Z_i} \rvert^{1/2}}$

In both cases, the integral computes the probability that the relative positions fall within the thresholds defined by the event, either in 1D (lateral distance) or in 3D (hard-body radius).

In the 3D case, a series of simplifications can be made. As explained in the article by Maruthi R. Akella and Kyle T. Alfriend, the volume integral can be reduced to a surface integral without losing any information about the Probability of Collision (PoC) in the process. In summary, the procedure starts by defining the relative positions $\boldsymbol{\rho}(t) = \mathbf{x}_{si}(t) - \mathbf{x}_p(t)$ and velocities $\boldsymbol{\nu}(t) = \mathbf{v}_{si}(t) - \mathbf{v}_p(t)$.

These quantities allow the computation of the TCA (when they become orthogonal) and enable the construction of an orthogonal coordinate system aligned with the relative geometry at conjunction. In particular, the frame is defined as:

$$\boldsymbol{\eta}_i = \frac{\boldsymbol{\nu}(t_i)}{\lVert \boldsymbol{\nu}(t_i) \rVert}, \qquad \boldsymbol{\xi}_i = \frac{\mathbf{v}_{si}(t_i) \times \mathbf{v}_p(t_i)}{\lVert \mathbf{v}_{si}(t_i) \times \mathbf{v}_p(t_i) \rVert}, \qquad \boldsymbol{\zeta}_i = \boldsymbol{\eta}_i \times \boldsymbol{\xi}_i. \tag{2.64}$$

Implicit in this definition is the corresponding orthogonal transformation matrix C_i, which maps vectors from the original reference frame to the conjunction frame:

$$\mathbf{C}_i = \begin{bmatrix} \boldsymbol{\eta}_i^\top \\ \boldsymbol{\xi}_i^\top \\ \boldsymbol{\zeta}_i^\top \end{bmatrix} = \begin{bmatrix} C_{11} & C_{12} & C_{13} \\ C_{21} & C_{22} & C_{23} \\ C_{31} & C_{32} & C_{33} \end{bmatrix} \tag{2.65}$$

This conjunction frame contains the so-called B-plane, defined in the literature as $\{\, \mathbf{x} \in \mathbb{R}^3 : \mathbf{x}\boldsymbol{\nu}(t_i) = 0 \,\}$, which corresponds to the plane orthogonal to the relative velocity at the TCA. The orthonormal basis of the B-plane is then given by $\{\boldsymbol{\xi}_i, \boldsymbol{\zeta}_i\}$.

Given the relative position at the TCA, $\boldsymbol{\rho}(t_i)$, expressed in the original reference frame, it can be rotated into the conjunction frame as $\hat{\boldsymbol{\rho}}(t_i) = \mathbf{C}_i\, \boldsymbol{\rho}(t_i)$.

By construction, the first component of this vector must be zero, since the conjunction frame aligns its $\boldsymbol{\eta}_i$ axis with the relative velocity. This allows extracting the B-vector as the projection of the relative position onto the B-plane using the transformation:

$$\mathbf{T}^* = \begin{bmatrix} 0 & 1 & 0 \\ 0 & 0 & 1 \end{bmatrix}, \qquad \boldsymbol{\rho}^*(t_i) = \mathbf{T}^*\, \mathbf{C}_i\, \boldsymbol{\rho}(t_i) \tag{2.66}$$

If this transformation is applied to the PoC integral through the transformation matrix $\mathbf{T}$, which performs the reference frame rotation and eliminates the components outside the B-plane, the probability calculation becomes:

$$P(A_i) = \iint_{|\mathbf{z}_i^*|<R} f^*(\mathbf{z}_i^*)\, d\mathbf{z}_i^* \tag{2.67}$$

where

$$f^*(\mathbf{z}_i^*) = \frac{1}{2\pi\, |\boldsymbol{\Sigma}_{Z_i}^*|^{1/2}} \exp\left(-\frac{1}{2} (\mathbf{z}_i^* - \boldsymbol{\mu}_{Z_i}^*)^\top (\boldsymbol{\Sigma}_{Z_i}^*)^{-1} (\mathbf{z}_i^* - \boldsymbol{\mu}_{Z_i}^*) \right) \tag{2.68}$$

$$\mathbf{z}_i^* = \mathbf{T}^*\, \mathbf{C}_i\, \mathbf{z}_i, \qquad \boldsymbol{\mu}_{Z_i}^* = \mathbf{T}^*\, \mathbf{C}_i\, \boldsymbol{\mu}_{Z_i}, \qquad \boldsymbol{\Sigma}_{Z_i}^* = \mathbf{T}^*\, \mathbf{C}_i\, \boldsymbol{\Sigma}_{Z_i}\, \mathbf{C}_i^\top\, \mathbf{T}^{*\top} \tag{2.69}$$

In summary, this simplification reduces the 3D collision-probability problem to a 2D analysis on the B-plane. By projecting the relative position and the covariance onto the plane perpendicular to the relative velocity, the calculation becomes simpler and more efficient, while still preserving the main characteristics of the encounter.

2.2.7. Joint Probability Between Events

In both cases, 1D and 3D, the probability that at least one event occurs yields $P(A \cup B) = P(A) + P(B) - P(A \cap B)$. To estimate this value, it is necessary to solve the joint probability between both events, which can be defined as:

1D	**3D**
$P(A_1 \cap A_2) = \iint_{\mathcal{D}} f(\mathbf{z})\, dz_1\, dz_2$	$P(A_1 \cap A_2) = \iiiint \iiint_{\mathcal{D}} f(\mathbf{z})\, d\mathbf{z}_1 d\mathbf{z}_2$
$f(\mathbf{z}) = \frac{\exp(-\frac{1}{2}(\mathbf{z}-\boldsymbol{\mu}_Z)^\top \boldsymbol{\Sigma}_Z^{-1}(\mathbf{z}-\boldsymbol{\mu}_Z))}{(2\pi)^{2/2}\,\lvert\boldsymbol{\Sigma}_z\rvert^{1/2}}$	$f(\mathbf{z}) = \frac{\exp(-\frac{1}{2}(\mathbf{z}-\boldsymbol{\mu}_Z)^\top \boldsymbol{\Sigma}_Z^{-1}(\mathbf{z}-\boldsymbol{\mu}_Z))}{(2\pi)^{6/2}\,\lvert\boldsymbol{\Sigma}_z\rvert^{1/2}}$
$\mathbf{z} = \begin{bmatrix} z_1 \\ z_2 \end{bmatrix}, \boldsymbol{\mu}_z = \begin{bmatrix} \mu_{Z_1} \\ \mu_{Z_2} \end{bmatrix}, \boldsymbol{\Sigma}_z = \begin{bmatrix} \sigma^2_{Z_1} & \rho\sigma_{Z_1}\sigma_{Z_2} \\ \rho\sigma_{Z_1}\sigma_{Z_2} & \sigma^2_{Z_2} \end{bmatrix}$	$\mathbf{z} = \begin{bmatrix} \mathbf{z}_1 \\ \mathbf{z}_2 \end{bmatrix}, \boldsymbol{\mu}_z = \begin{bmatrix} \mu_{Z_1} \\ \mu_{Z_2} \end{bmatrix}, \boldsymbol{\Sigma}_z = \begin{bmatrix} \boldsymbol{\Sigma}_{z_1} & \boldsymbol{\Sigma}_{z_1,z_2} \\ \boldsymbol{\Sigma}^\top_{z_1,z_2} & \boldsymbol{\Sigma}_{z_2} \end{bmatrix}$
$\mathcal{D} = \{(z_1, z_2) \mid \lvert z_1\rvert < W,\ \lvert z_2\rvert < W\}$	$\mathcal{D} = \{(\mathbf{z}_1, \mathbf{z}_2) \mid \lVert\mathbf{z}_1\rVert < R_1, \lVert\mathbf{z}_2\rVert < R_2\}$

Where the correlation coefficient in 1D can be estimated taking into account the intrinsic correlation between the pedestrians and the correlation introduced due to the fact that the primary is the same in both events, $\rho = \rho_{X_1X_1} + \frac{\sigma_v^2}{\sigma_{Z_1}\sigma_{Z_2}}$. In the case of the 3D problem, the development of $\boldsymbol{\Sigma}_{Z_1,Z_2}$ is not direct and must be estimated carefully.

Once the method has been extended to the 3D case, a simplification of the final integral is introduced, following the approach of Akella and Alfriend. The 6D integration volume, corresponding to the relative positions of the two conjunctions, can be separated into two independent 3D sub-volumes, one for each conjunction, which are then projected onto their respective B-planes as detailed below.

Let $\mathbf{C}_i$ be the rotation matrix from the inertial reference frame to the conjunction frame associated with each encounter (see Eq. (2.65)), and let $\mathbf{T}^*$ be the matrix which projects vectors onto the B-plane by removing the component along the relative velocity (see Eq. (2.66)), both already defined.

Extending the development of Akella and Alfriend to a 6D setting, the combined transformation matrix $\mathbf{T}$ is defined as:

$$\mathbf{T} = \begin{bmatrix} \mathbf{T}^*\mathbf{C}_1 & \mathbf{0} \\ \mathbf{0} & \mathbf{T}^*\mathbf{C}_2 \end{bmatrix} \tag{2.70}$$

This matrix simultaneously rotates the 3D relative position vectors and projects them, along with the covariance matrix, onto their respective B-planes. This yields:

$$P(A_1 \cap A_2) = \iint_{|\mathbf{z}_1^*|<R_1} \iint_{|\mathbf{z}_2^*|<R_2} f^*(\mathbf{z}^*)\, d\mathbf{z}_2^*\, d\mathbf{z}_1^* \tag{2.71}$$

where the transformed probability density is:

$$f^*(\mathbf{z}^*) = \frac{\exp\left[-\frac{1}{2}(\mathbf{z}^* - \boldsymbol{\mu}_Z^*)^\top (\boldsymbol{\Sigma}_Z^*)^{-1} (\mathbf{z}^* - \boldsymbol{\mu}_Z^*) \right]}{(2\pi)^2 |\boldsymbol{\Sigma}_Z^*|^{1/2}} \tag{2.72}$$

The transformed variables are defined as:

$$\mathbf{z}^* = \mathbf{T}\,\mathbf{z}, \qquad \boldsymbol{\mu}_Z^* = \mathbf{T}\,\boldsymbol{\mu}_Z, \qquad \boldsymbol{\Sigma}_Z^* = \mathbf{T}\,\boldsymbol{\Sigma}_Z\,\mathbf{T}^\top \tag{2.73}$$

This reduction from the original 6D integral to a 4D integral works because the collision probability depends only on the components of the relative position vectors projected in the B-plane, that is, perpendicular to the relative velocity at each conjunction. Each 3D relative position vector can be separated into a component along the relative velocity and two components in the B-plane.

The transformation matrices $\mathbf{T}^*\mathbf{C}_i$ carry out this projection in a consistent way. Applying the same transformation to the covariance matrix preserves all correlations between the components in the B-plane, so the statistical description of the relative position in the plane remains valid. As a result, each 3D vector reduces to 2D in its B-plane, and the joint probability integral over the two conjunctions becomes a 4D integral that captures all the relevant uncertainty for the collision events.

To clarify how the transformation in Eq. (2.73) operates on the block-structured state vector and covariance matrix, the explicit form of each product will be developed. Given that:

$$\mathbf{z} = \begin{bmatrix} \mathbf{z}_1 \\ \mathbf{z}_2 \end{bmatrix}, \qquad \boldsymbol{\mu}_Z = \begin{bmatrix} \boldsymbol{\mu}_{Z_1} \\ \boldsymbol{\mu}_{Z_2} \end{bmatrix}, \qquad \boldsymbol{\Sigma}_Z = \begin{bmatrix} \boldsymbol{\Sigma}_{Z_1} & \boldsymbol{\Sigma}_{Z_{1,2}} \\ \boldsymbol{\Sigma}_{Z_{1,2}}^\top & \boldsymbol{\Sigma}_{Z_2} \end{bmatrix} \tag{2.74}$$

and recalling that:

$$\mathbf{T} = \begin{bmatrix} \mathbf{T}^*\mathbf{C}_1 & \mathbf{0} \\ \mathbf{0} & \mathbf{T}^*\mathbf{C}_2 \end{bmatrix} \tag{2.75}$$

the transformed vector can be written as:

$$\mathbf{z}^* = \mathbf{T}\mathbf{z} = \begin{bmatrix} \mathbf{T}^*\mathbf{C}_1\mathbf{z}_1 \\ \mathbf{T}^*\mathbf{C}_2\mathbf{z}_2 \end{bmatrix}, \qquad \boldsymbol{\mu}_Z^* = \mathbf{T}\boldsymbol{\mu}_Z = \begin{bmatrix} \mathbf{T}^*\mathbf{C}_1\boldsymbol{\mu}_{Z_1} \\ \mathbf{T}^*\mathbf{C}_2\boldsymbol{\mu}_{Z_2} \end{bmatrix} \tag{2.76}$$

Finally, the covariance transformation expands as:

$$\mathbf{\Sigma}_Z^* = \mathbf{T}\mathbf{\Sigma}_Z\mathbf{T}^\top = \begin{bmatrix} \mathbf{T}^*\mathbf{C}_1\mathbf{\Sigma}_{Z_1}\mathbf{C}_1^\top\mathbf{T}^{*\top} & \mathbf{T}^*\mathbf{C}_1\mathbf{\Sigma}_{Z_{1,2}}\mathbf{C}_2^\top\mathbf{T}^{*\top} \\ \mathbf{T}^*\mathbf{C}_2\mathbf{\Sigma}_{Z_{1,2}}^\top\mathbf{C}_1^\top\mathbf{T}^{*\top} & \mathbf{T}^*\mathbf{C}_2\mathbf{\Sigma}_{Z_2}\mathbf{C}_2^\top\mathbf{T}^{*\top} \end{bmatrix} \tag{2.77}$$

This representation makes explicit how each conjunction's rotation matrix $\mathbf{C}_i$ and projection matrix $\mathbf{T}^*$ independently operate on the corresponding position and covariance blocks, while preserving the cross-correlation terms between conjunctions.

In order to simplify the expression of the joint probability, it is useful to apply the Schur complement factorization to the covariance matrix $\mathbf{\Sigma}_Z^*$, which in this context has the block structure:

$$\mathbf{\Sigma}_Z^* = \begin{bmatrix} \mathbf{\Sigma}_{Z_1}^* & \mathbf{\Sigma}_{Z_{1,2}}^* \\ \mathbf{\Sigma}_{Z_{1,2}}^{*\top} & \mathbf{\Sigma}_{Z_2}^* \end{bmatrix} \tag{2.78}$$

According to Zhang [28], this matrix can be factorized using the Schur complement as:

$$\mathbf{\Sigma}_Z^* = \begin{bmatrix} \mathbf{I} & \mathbf{0} \\ \mathbf{\Sigma}_{Z_{1,2}}^{*\top}\mathbf{\Sigma}_{Z_1}^{*-1} & \mathbf{I} \end{bmatrix} \begin{bmatrix} \mathbf{\Sigma}_{Z_1}^* & \mathbf{0} \\ \mathbf{0} & \mathbf{S} \end{bmatrix} \begin{bmatrix} \mathbf{I} & \mathbf{\Sigma}_{Z_1}^{*-1}\mathbf{\Sigma}_{Z_{1,2}}^* \\ \mathbf{0} & \mathbf{I} \end{bmatrix} \tag{2.79}$$

where $\mathbf{S}$ denotes the *Schur complement* of the block $\mathbf{\Sigma}_{Z_1}^*$, defined as:

$$\mathbf{S} \equiv \mathbf{\Sigma}_{Z_2|Z_1}^* = \mathbf{\Sigma}_{Z_2}^* - \mathbf{\Sigma}_{Z_{1,2}}^{*\top}\mathbf{\Sigma}_{Z_1}^{*-1}\mathbf{\Sigma}_{Z_{1,2}}^* \tag{2.80}$$

From a statistical point of view, $\mathbf{S}$ is the conditional covariance of the second event's 2D relative-position vector given the first one, analogous to the scalar conditional variance defined in Eq. (2.33) in the univariate Gaussian case.

In other words, $\mathbf{S}$ quantifies how uncertain the second event remains after incorporating all the information of the first event. When the two events are strongly correlated, $\mathbf{S}$ becomes much smaller than $\mathbf{\Sigma}_{Z_2}^*$, reflecting the reduction of uncertainty due to the high correlation.

This factorization has two key consequences [28]:

$$|\mathbf{\Sigma}_Z^*| = |\mathbf{\Sigma}_{Z_1}^*|\,|\mathbf{S}| \tag{2.81}$$

$$\mathbf{\Sigma}_Z^{*-1} = \begin{bmatrix} \mathbf{\Sigma}_{Z_1}^{*-1} + \mathbf{\Sigma}_{Z_1}^{*-1}\mathbf{\Sigma}_{Z_{1,2}}^*\mathbf{S}^{-1}\mathbf{\Sigma}_{Z_{1,2}}^{*\top}\mathbf{\Sigma}_{Z_1}^{*-1} & -\mathbf{\Sigma}_{Z_1}^{*-1}\mathbf{\Sigma}_{Z_{1,2}}^*\mathbf{S}^{-1} \\ -\mathbf{S}^{-1}\mathbf{\Sigma}_{Z_{1,2}}^{*\top}\mathbf{\Sigma}_{Z_1}^{*-1} & \mathbf{S}^{-1} \end{bmatrix} \tag{2.82}$$

Using the Schur complement factorization, the exponent of the 4D Gaussian probability density function can be rewritten as:

$$\begin{pmatrix} \mathbf{z}_1^* - \boldsymbol{\mu}_{Z_1}^* \\ \mathbf{z}_2^* - \boldsymbol{\mu}_{Z_2}^* \end{pmatrix}^\top \boldsymbol{\Sigma}_Z^{*-1} \begin{pmatrix} \mathbf{z}_1^* - \boldsymbol{\mu}_{Z_1}^* \\ \mathbf{z}_2^* - \boldsymbol{\mu}_{Z_2}^* \end{pmatrix} = (\mathbf{z}_1^* - \boldsymbol{\mu}_{Z_1}^*)^\top \boldsymbol{\Sigma}_{Z_1}^{*-1} (\mathbf{z}_1^* - \boldsymbol{\mu}_{Z_1}^*) + (\mathbf{z}_2^* - \boldsymbol{\mu}_{Z_2|Z_1}^*)^\top \boldsymbol{\Sigma}_{Z_2|Z_1}^{*-1} (\mathbf{z}_2^* - \boldsymbol{\mu}_{Z_2|Z_1}^*) \tag{2.83}$$

where

$$\boldsymbol{\mu}_{Z_2|Z_1}^* = \boldsymbol{\mu}_{Z_2}^* + \boldsymbol{\Sigma}_{Z_{1,2}}^{*\top} \boldsymbol{\Sigma}_{Z_1}^{*-1} (\mathbf{z}_1^* - \boldsymbol{\mu}_{Z_1}^*) \tag{2.84}$$

Here, $\boldsymbol{\Sigma}_{Z_2|Z_1}^{*-1}$ is the inverse of the Schur complement of $\boldsymbol{\Sigma}_{Z_1}^*$, representing the inverse conditional covariance of the second event's relative position given the first one. And $\boldsymbol{\mu}_{Z_2|Z_1}^*$ is the equivalent to the scalar conditional mean defined in Eq. (2.33) extended to a two-dimensional case.

Using this decomposition, the 4D Gaussian PDF from Eq. (2.72) can be factorized into a marginal PDF for $\mathbf{z}_1^*$ and a conditional PDF for $\mathbf{z}_2^*$ given $\mathbf{z}_1^*$:

$$f^*(\mathbf{z}^*) = f_{Z_1}^*(\mathbf{z}_1^*)\, f_{Z_2|Z_1}^*(\mathbf{z}_2^* \mid \mathbf{z}_1^*) \tag{2.85}$$

where the marginal PDF of $\mathbf{z}_1^*$ is:

$$f_{Z_1}^*(\mathbf{z}_1^*) = \frac{\exp\left[-\frac{1}{2} (\mathbf{z}_1^* - \boldsymbol{\mu}_{Z_1}^*)^\top \boldsymbol{\Sigma}_{Z_1}^{*-1} (\mathbf{z}_1^* - \boldsymbol{\mu}_{Z_1}^*) \right]}{2\pi |\boldsymbol{\Sigma}_{Z_1}^*|^{1/2}} \tag{2.86}$$

and the conditional PDF of $\mathbf{z}_2^*$ given $\mathbf{z}_1^*$ is:

$$f_{Z_2|Z_1}^*(\mathbf{z}_2^* \mid \mathbf{z}_1^*) = \frac{\exp\left[-\frac{1}{2} (\mathbf{z}_2^* - \boldsymbol{\mu}_{Z_2|Z_1}^*)^\top \boldsymbol{\Sigma}_{Z_2|Z_1}^{*-1} (\mathbf{z}_2^* - \boldsymbol{\mu}_{Z_2|Z_1}^*) \right]}{2\pi |\boldsymbol{\Sigma}_{Z_2|Z_1}^*|^{1/2}} \tag{2.87}$$

This factorization explicitly shows that the 4D joint distribution can be evaluated as the product of a 2D marginal and a 2D conditional distribution, which forms the basis for reducing the original 4D probability integral into nested 2D integrals.

Using this factorization while preserving the original integration domains in the B-planes, the joint probability can be expressed as:

$$P(A_1 \cap A_2) = \iint_{|\mathbf{z}_1^*|<R_1} f_{Z_1}^*(\mathbf{z}_1^*) \underbrace{\left(\iint_{|\mathbf{z}_2^*|<R_2} f_{Z_2|Z_1}^*(\mathbf{z}_2^* \mid \mathbf{z}_1^*)\, d\mathbf{z}_2^* \right)}_{\text{conditional probability in the second B-plane}} d\mathbf{z}_1^* \tag{2.88}$$

Here, the outer integral evaluates the probability of the first conjunction over its B-plane, while the inner integral computes the conditional probability of the second conjunction given a particular realization of $\mathbf{z}_1^*$. This approach correctly accounts for the correlation between the two conjunctions through the off-diagonal blocks of the original 4D covariance matrix, while reducing the computational cost from a 4D to two nested 2D integrals.

Finally, this nested analytical expression is resolved numerically by discretizing the continuous integration domains into discrete summations. To evaluate these summations, a dynamic meshing strategy is implemented, where the grid resolution is dependent on the HBR and the magnitude of the respective covariance matrices. This adaptive discretization ensures that a high level of numerical precision is maintained within the regions of greatest probability density, while simultaneously preventing an excessive increase in the overall computational cost.

2.3. Construction of the Global Covariance Matrix

Now, the main problem is the correct characterization of the correlations between events. As shown in previous chapters, the assumption of independence ($P(A \cap B) \approx P(A)P(B)$) fails when there are shared sources of uncertainty.

This section presents the analytical framework to build the global covariance matrix, $\mathbf{\Sigma}_Z$. This matrix describes the joint uncertainty of the relative positions at the times of the two encounters, t_1 and t_2. Unlike standard methods that evaluate the covariance at the time of closest approach in isolation, this formulation considers the evolution of the uncertainty and how the events are coupled ($\Sigma_{Z_{1,2}} \neq 0$).

Specifically, the mathematical model developed below integrates three fundamental sources of correlation found in Low Earth Orbit (LEO):

1. **The Common Primary Object:** Since the same primary satellite is involved in both events, its state uncertainty is not independent between t_1 and t_2. The uncertainty in the primary's initial position and velocity propagates through the State Transition Matrix (STM)—a linear mathematical operator derived from the orbital dynamics that maps deviations from a reference epoch to a future time. By projecting the primary's state error from t_1 to t_2, the STM creates a direct physical and statistical link between the position errors at both encounters.

2. **The Common Secondary Object (Re-encounter):** In specific scenarios, the primary satellite may encounter the same debris object twice (e.g., after one orbital revolution). In this case, the secondary object's state uncertainty is also propagated

from the first event to the second. This creates an additional correlation term, as the uncertainty of the secondary object at t_2 depends directly on its state at t_1.

3. **Dynamic Model Uncertainty (Atmospheric Drag):** In addition to the initial state uncertainty, the orbit propagation is subject to uncertainty in the force model. In LEO, the uncertainty in atmospheric density is the dominant source of uncertainty for propagation of few days. In this work, the density is modeled as a random variable with an associated uncertainty (σ_ρ) constant throughout the propagation. Since this density error affects the trajectory propagation over the entire analysis interval, it acts as a common perturbation that further correlates the relative positions at different times.

The objective of the following subsections is to explicitly derive the blocks of the matrix $\mathbf{\Sigma}_Z$, quantifying how these sources of error combine to form the cross-covariance terms $\mathbf{\Sigma}_{Z_{1,2}}$ required for the joint probability calculation.

2.3.1. First Case: Common Primary Object

Before introducing environmental uncertainties, we first derive the global covariance matrix considering the correlation induced by the common primary satellite. Ideally, for long propagation intervals in LEO (more or less 12 hours, which corresponds to the typical update cycle for catalogued orbits when only one radar is used, the update time could decrease with the use of more radars), Even if the complexity level of the propagations is high, the non-linear effects only play an important role under 500 km and for a few days of propagation, consequently, in the cases studied the linear approximation is sufficient.

To maximize accuracy while maintaining analytical feasibility, this thesis adopts a hybrid propagation strategy. This approach relies on propagating both the state and the uncertainty of the primary satellite to the Time of Closest Approach (TCA) of each event using full dynamic models. Subsequently, to simplify the mathematical development of the joint probability, the variation of the primary's covariance between the two TCAs is approximated linearly using the State Transition Matrix (STM).

Satellite Kinematics and STM

Let the state vector of a satellite at time t be denoted by $\mathbf{y}(t) = [\mathbf{r}(t)^\top, \mathbf{v}(t)^\top]^\top$. The evolution of the mean state from an initial epoch t_0 is governed by the non-linear flow of the dynamics φ:

$$\mathbf{y}(t) = \varphi(t, t_0, \mathbf{y}_0) \tag{2.89}$$

For uncertainty propagation, we linearize the dynamics around the reference trajectory. The evolution of the state error $\delta\mathbf{y}(t)$ is described by the State Transition Matrix (STM), denoted as $\mathbf{\Phi}(t, t_0)$:

$$\delta\mathbf{y}(t) = \mathbf{\Phi}(t, t_0)\,\delta\mathbf{y}(t_0) \tag{2.90}$$

The STM maps the deviations from the initial epoch to any future time t. Consequently, the covariance matrix of the full state of the satellite, $\mathbf{\Sigma}_Y(t)$, at any instant is obtained from its initial covariance $\mathbf{\Sigma}_Y(t_0)$ via the standard propagation law:

$$\mathbf{\Sigma}_Y(t) = \mathbf{\Phi}(t, t_0)\,\mathbf{\Sigma}_Y(t_0)\,\mathbf{\Phi}(t, t_0)^\top \tag{2.91}$$

It is important to note that in this development, this linearization is specifically applied to model the correlation evolution during the interval between the two TCAs, because the propagation until these TCAs will be obtained from other methods more realistic.

Construction of the Global Covariance

We now define the components of the global covariance matrix $\mathbf{\Sigma}_Z$ for the two-event scenario defined in Eq. (1.30).

The random variable for the k-th event is the relative position vector $\mathbf{Z}_k = \mathbf{r}_{s_k}(t_k) - \mathbf{r}_p(t_k)$. The global covariance matrix is composed of four blocks:

$$\mathbf{\Sigma}_Z = \begin{bmatrix} \mathrm{Cov}(\mathbf{Z}_1, \mathbf{Z}_1) & \mathrm{Cov}(\mathbf{Z}_1, \mathbf{Z}_2) \\ \mathrm{Cov}(\mathbf{Z}_2, \mathbf{Z}_1) & \mathrm{Cov}(\mathbf{Z}_2, \mathbf{Z}_2) \end{bmatrix} = \begin{bmatrix} \mathbf{\Sigma}_{Z_1} & \mathbf{\Sigma}_{Z_{1,2}} \\ \mathbf{\Sigma}_{Z_{2,1}} & \mathbf{\Sigma}_{Z_2} \end{bmatrix} \tag{2.92}$$

Diagonal Blocks The diagonal blocks $\mathbf{\Sigma}_{Z_1}$ and $\mathbf{\Sigma}_{Z_2}$ represent the covariance of each encounter considered independently. For the analysis, it is assumed that the state covariance matrices of the primary satellite and secondary objects at the encounter times, $\mathbf{\Sigma}(t_k)$, are available, regardless of the propagation method employed. Regarding the correlation between objects, it is assumed that the initial state errors of all objects are uncorrelated (excluding, for instance, common sensor biases). Furthermore, it is assumed that the dynamical models do not contain shared errors yet that would induce correlation between the objects' trajectories.

$$\mathbf{\Sigma}_{Z_k} = \mathrm{Cov}(\mathbf{Z}_1, \mathbf{Z}_1) = \mathrm{Var}(\mathbf{Z}_1) = \mathrm{Var}(\mathbf{r}_{s_k}(t_k) - \mathbf{r}_p(t_k)) = \mathbf{\Sigma}_{r_{si}}(t_k) + \mathbf{\Sigma}_{r_p}(t_k) \tag{2.93}$$

where $\mathbf{\Sigma}_{r_{si}}$ is the position covariance of the secondary object and $\mathbf{\Sigma}_{r_p}$ is the position covariance of the primary.

Off-Diagonal Block The off-diagonal blocks $\mathbf{\Sigma}_{Z_{1,2}} = \mathbf{\Sigma}_{Z_{2,1}}$ (due to the symmetry of the covariance matrix) captures the correlation between the two events. While the covariances at t_1 and t_2 are available, we assume that over the short time interval between the two encounters ($\Delta t = t_2 - t_1$), the evolution of the state deviation is sufficiently linear. This allows us to map the uncertainty from the first encounter to the second using the STM.

By definition:

$$\mathbf{\Sigma}_{Z_{1,2}} = \mathrm{Cov}(\mathbf{Z}_1, \mathbf{Z}_2) = E\left[(\mathbf{r}_{s1} - \mathbf{r}_{p1})(\mathbf{r}_{s2} - \mathbf{r}_{p2})^\top\right] \tag{2.94}$$

For the sake of notation simplicity, the explicit time dependencies are excluded in some formulas. Let the subscripts denote the specific object and the specific event time (TCA) simultaneously:

- $\mathbf{r}_{p1} \equiv \mathbf{r}_p(t_1)$: Position of the primary object at t_1.
- $\mathbf{r}_{p2} \equiv \mathbf{r}_p(t_2)$: Position of the primary object at t_2.
- $\mathbf{r}_{s1} \equiv \mathbf{r}_{s1}(t_1)$: Position of the first secondary object at t_1.
- $\mathbf{r}_{s2} \equiv \mathbf{r}_{s2}(t_2)$: Position of the second secondary object at t_2.

Since the secondary objects are independent, the expression simplifies to the auto-covariance of the primary satellite:

$$\mathbf{\Sigma}_{Z_{1,2}} = E\left[(-\mathbf{r}_{p1})(-\mathbf{r}_{p2})^\top\right] = E\left[\mathbf{r}_p(t_1)\,\mathbf{r}_p(t_2)^\top\right] \tag{2.95}$$

Using the linearized mapping $\delta\mathbf{y}_p(t_2) = \mathbf{\Phi}_p(t_2, t_1)\,\delta\mathbf{y}_p(t_1)$, we decompose the state transition matrix and the covariance matrix into their position (r) and velocity (v) 3×3 sub-blocks:

$$\mathbf{\Phi}_p(t_2, t_1) = \begin{bmatrix} \mathbf{\Phi}_{r_p} & \mathbf{\Phi}_{rv_p} \\ \mathbf{\Phi}_{vr_p} & \mathbf{\Phi}_{v_p} \end{bmatrix}, \qquad \mathbf{\Sigma}Y_p(t_1) = \begin{bmatrix} \mathbf{\Sigma}_{r_p} & \mathbf{\Sigma}_{rv_p} \\ \mathbf{\Sigma}_{vr_p} & \mathbf{\Sigma}_{v_p} \end{bmatrix} \tag{2.96}$$

Substituting this decomposition into the expectation value yields the full covariance update:

$$\mathrm{Cov}(\mathbf{y}_p(t_1), \mathbf{y}_p(t_2)) = \begin{bmatrix} \mathbf{\Sigma}_{r_p} & \mathbf{\Sigma}_{rv_p} \\ \mathbf{\Sigma}_{vr_p} & \mathbf{\Sigma}_{v_p} \end{bmatrix} \begin{bmatrix} \mathbf{\Phi}_{r_p}^\top & \mathbf{\Phi}_{vr_p}^\top \\ \mathbf{\Phi}_{rv_p}^\top & \mathbf{\Phi}_{v_p}^\top \end{bmatrix} \tag{2.97}$$

Finally, considering only the position components (the upper-left block of the resulting matrix), we obtain the analytical expression for the cross-correlation block:

$$\mathbf{\Sigma}_{Z_{1,2}} = \mathbf{\Sigma}_{r_p}(t_1)\mathbf{\Phi}_{r_p}(t_2, t_1)^\top + \mathbf{\Sigma}_{rv_p}(t_1)\mathbf{\Phi}_{rv_p}(t_2, t_1)^\top \tag{2.98}$$

2.3.2. Second Case: Repeated Encounter with the Same Secondary

This scenario represents a special case of maximum physical correlation, where the primary satellite (p) encounters the same secondary object (s) at two different epochs t_1 and t_2 (e.g., due to orbital geometry resulting in a re-encounter after one period).

In this case, the independence assumption between the secondary states at t_1 and t_2 is no longer valid. The uncertainty of the secondary object also propagates from the first event to the second, creating a strong statistical link parallel to that of the primary.

Kinematics and STM for the Secondary

Since the secondary object is now common to both events, its state evolution must be modeled explicitly. Let $\mathbf{\Phi}_s(t_2, t_1)$ denotes the State Transition Matrix governing the motion of the secondary object between the two encounters. Similar to the primary, the propagation of the secondary's state error is linearized as:

$$\delta \mathbf{y}_s(t_2) = \mathbf{\Phi}_s(t_2, t_1)\, \delta \mathbf{y}_s(t_1) \tag{2.99}$$

It is important to note that $\mathbf{\Phi}_s$ differs from the primary's STM ($\mathbf{\Phi}_p$) because the two objects follow different trajectories and experience different linearized dynamics.

Construction of the Global Covariance

The structure of the global covariance matrix $\mathbf{\Sigma}_Z$ remains the same as in the previous case, but the content of the blocks changes to reflect the added correlation.

Diagonal Blocks The diagonal blocks $\mathbf{\Sigma}_{Z_1}$ and $\mathbf{\Sigma}_{Z_2}$ define the uncertainty of each encounter individually. As in the first case, we assume that the individual covariances at the time of the events are obtained previously.

$$\mathbf{\Sigma}_{Z_k} = \mathrm{Var}(\mathbf{r}_s(t_k) - \mathbf{r}_p(t_k)) = \mathbf{\Sigma}_{r_s}(t_k) + \mathbf{\Sigma}_{r_p}(t_k) \quad \text{for } k = 1, 2 \tag{2.100}$$

where $\mathbf{\Sigma}_{r_s}(t_k)$ is the position covariance of the secondary object at time t_k.

Off-Diagonal Block The off-diagonal block $\mathbf{\Sigma}_{Z_{1,2}}$ now captures the correlation contributed by both objects. The covariance between the relative position vectors is defined as:

$$\mathbf{\Sigma}_{Z_{1,2}} = E\left[(\mathbf{r}_{s1} - \mathbf{r}_{p1})(\mathbf{r}_{s2} - \mathbf{r}_{p2})^\top\right] \tag{2.101}$$

Expanding this product, and assuming that the primary and secondary objects are statistically independent of each other (i.e., cross-terms between p and s vanish), we obtain the sum of two auto-correlations:

$$\mathbf{\Sigma}_{Z_{1,2}} = E\left[\mathbf{r}_{s1}\mathbf{r}_{s2}^\top\right] + E\left[\mathbf{r}_{p1}\mathbf{r}_{p2}^\top\right] \tag{2.102}$$

Applying the same strategy as before, we use the STM of each object to map the correlation from t_1 to t_2:

$$E\left[\mathbf{r}_{p1}\mathbf{r}_{p2}^\top\right] = \mathbf{\Sigma}_{r_p}(t_1)\mathbf{\Phi}_{r_p}(t_2,t_1)^\top + \mathbf{\Sigma}_{rv_p}(t_1)\mathbf{\Phi}_{rv_p}(t_2,t_1)^\top \tag{2.103}$$

$$E\left[\mathbf{r}_{s1}\mathbf{r}_{s2}^\top\right] = \mathbf{\Sigma}_{r_s}(t_1)\mathbf{\Phi}_{r_s}(t_2,t_1)^\top + \mathbf{\Sigma}_{rv_s}(t_1)\mathbf{\Phi}_{rv_s}(t_2,t_1)^\top \tag{2.104}$$

Substituting these into the expression for $\mathbf{\Sigma}_{Z_{1,2}}$, the final analytical form for the cross-correlation block in a repeated encounter scenario is:

$$\mathbf{\Sigma}_{Z_{1,2}} = \mathbf{\Sigma}_{r_p}\mathbf{\Phi}_{r_p}^\top + \mathbf{\Sigma}_{rv_p}\mathbf{\Phi}_{rv_p}^\top + \mathbf{\Sigma}_{r_s}\mathbf{\Phi}_{r_s}^\top + \mathbf{\Sigma}_{rv_s}\mathbf{\Phi}_{rv_s}^\top \tag{2.105}$$

For brevity, all covariance matrices $\mathbf{\Sigma}$ are evaluated at time t_1, and all state transition matrices $\mathbf{\Phi}$ propagate the state from t_1 to t_2, consistently with the STM notation adopted throughout this work.

This result demonstrates that in a re-encounter scenario, the correlation is increased because both objects contribute to the coupling between the events.

2.3.3. Third Case: Influence of Environmental Uncertainty (Atmospheric Drag)

This final case addresses the most realistic scenario in Low Earth Orbit (LEO): the presence of a common environmental source of uncertainty, specifically atmospheric drag, affecting a primary satellite encountering the same secondary object at two different TCA (t_1 and t_2).

As established by Hejduk et al. [39], errors in the atmospheric density acts as a systematic bias rather than random noise. A deviation in the predicted space weather affects the trajectory propagation of the Primary satellite (p) and the Secondary object (s) simultaneously over the analysis interval. Consequently, even if the secondary objects are distinct and their initial states are independent, the shared environmental error creates a statistical dependence between the two events.

Modelling the Global Environmental Error

Following the formulation by Casali et al.[38], the uncertainty in the atmospheric density is modelled as a single global random variable $\epsilon_\rho \sim \mathcal{N}(\mu_\rho, \sigma_\rho^2)$, which will be considered without any correlation with the initial state.

In this expression, μ_ρ denotes the expected value (mean bias) of the density prediction error, and σ_ρ represents the standard deviation associated with the model's uncertainty. For the purpose of this analysis, the atmospheric density model is assumed to be unbiased, meaning that the predicted density matches the true atmospheric density on average. Consequently, the mean of the error distribution is set to zero:

$$\mu_\rho = 0 \tag{2.106}$$

To capture the full dynamic effect of this perturbation, the state deviation must include both position and velocity components. The state deviation of any object j at time t is expressed as the sum of its propagated initial state error and the environmental error accumulated along its trajectory. Expanding the state vector into position ($\mathbf{r}$) and velocity ($\mathbf{v}$) blocks yields:

$$\begin{bmatrix} \delta\mathbf{r}_j(t) \\ \delta\mathbf{v}_j(t) \end{bmatrix} = \begin{bmatrix} \mathbf{\Phi}_{rr}(t,t_0) & \mathbf{\Phi}_{rv}(t,t_0) \\ \mathbf{\Phi}_{vr}(t,t_0) & \mathbf{\Phi}_{vv}(t,t_0) \end{bmatrix} \begin{bmatrix} \delta\mathbf{r}_j(t_0) \\ \delta\mathbf{v}_j(t_0) \end{bmatrix} + \begin{bmatrix} \mathbf{S}_{r,j}(t) \\ \mathbf{S}_{v,j}(t) \end{bmatrix} \epsilon_\rho \tag{2.107}$$

where the transition matrix $\mathbf{\Phi}$ is partitioned into 3×3 sub-blocks relating position and velocity. The term multiplying the density error is the generalized sensitivity vector $\mathbf{S}_j(t)$, which is now decomposed into:

- $\mathbf{S}_{r,j}(t) = \frac{\partial \mathbf{r}_j(t)}{\partial \epsilon_\rho}$: The sensitivity of the position to the density deviation.
- $\mathbf{S}_{v,j}(t) = \frac{\partial \mathbf{v}_j(t)}{\partial \epsilon_\rho}$: The sensitivity of the velocity to the density deviation.

It is important to note that these sensitivity vectors will differ for the primary ($\mathbf{S}_p$) and secondary objects ($\mathbf{S}_{s1}, \mathbf{S}_{s2}$) based on their specific ballistic coefficients and orbital regimes.

Construction of the Global Covariance

The structure of the global covariance matrix $\mathbf{\Sigma}_Z$ remains the same as in the previous case, but the content of the blocks changes to reflect the added correlation.

Diagonal Blocks The diagonal blocks $\mathbf{\Sigma}_{Z_k}$ represent the total covariance of the relative position vector $\mathbf{Z}_k$ for the k-th encounter ($k = 1, 2$). This matrix combines the independent propagated state covariances of the primary and the specific secondary object (s), increased by the correlated environmental uncertainty.

Using the relative sensitivity vector $\mathbf{S}_{rel,k} = \mathbf{S}_{rs}(t_k) - \mathbf{S}_{rp}(t_k)$, the covariance is given by:

$$\mathbf{\Sigma}_{Z_k} = \mathrm{Var}(\mathbf{Z}_k) = \mathrm{Var}(\mathbf{r}_s(t_k) - \mathbf{r}_p(t_k)) = \mathbf{\Sigma}_{r_s}(t_k) + \mathbf{\Sigma}_{r_p}(t_k) + \mathbf{S}_{rel,k}\mathbf{S}_{rel,k}^\top \sigma_\rho^2 \tag{2.108}$$

The term $\mathbf{S}_{rel,k}\mathbf{S}_{rel,k}^\top \sigma_\rho^2$ represents the contribution of the global density error projected onto the relative geometry. This formulation captures the physical coupling: if the primary and secondary objects have similar ballistic properties and trajectories ($\mathbf{S}_s \approx \mathbf{S}_p$), the environmental error cancels out in the relative frame, preventing the increment of the covariance.

Off-Diagonal Block The cross-covariance $\mathbf{\Sigma}_{Z_{1,2}}$ between the relative positions at t_1 and t_2 must now capture both the objects' state propagation and the global environmental coupling.

$$\mathbf{\Sigma}_{Z_{1,2}} = \mathrm{Cov}(\mathbf{Z}_1, \mathbf{Z}_2) = E\left[(\mathbf{r}_{s1} - \mathbf{r}_{p1})(\mathbf{r}_{s2} - \mathbf{r}_{p2})^\top\right] \tag{2.109}$$

Expanding the terms, and assuming that the initial states of the different secondary object (s) are statistically independent of the primary (p), all cross-terms involving secondary state errors vanish. The remaining correlations are:

1. Primary State Correlation: The initial error of the primary propagates from t_1 to t_2.
2. Secondary State Correlation: The initial error of the secondary propagates from t_1 to t_2.
3. Environmental Correlation: The global density error ϵ_ρ links all terms.

The final analytical expression for the cross-correlation block is:

$$\mathbf{\Sigma}_{Z_{1,2}} = \underbrace{\left[\mathbf{\Sigma}_{r_p}\mathbf{\Phi}_{r_p}^\top + \mathbf{\Sigma}_{rv_p}\mathbf{\Phi}_{rv_p}^\top\right]}_{\text{Primary State Correlation}} + \underbrace{\left[\mathbf{\Sigma}_{r_s}\mathbf{\Phi}_{r_s}^\top + \mathbf{\Sigma}_{rv_s}\mathbf{\Phi}_{rv_s}^\top\right]}_{\text{Secondary State Correlation}} + \underbrace{\mathbf{S}_{rel,1}\mathbf{S}_{rel,2}^\top \sigma_\rho^2}_{\text{Environmental Correlation}} \tag{2.110}$$

For brevity, all covariance matrices $\mathbf{\Sigma}$ are evaluated at time t_1, and all state transition matrices $\mathbf{\Phi}$ propagate the state from t_1 to t_2, consistently with the STM notation adopted throughout this work.

In the specific case where the secondary object is different for each event ($s_1 \neq s_2$), the Secondary State Correlation term will vanish, reducing the formula.

2.4. Orbital 3D Cases of Study

This section presents the scenarios selected for the numerical validation and analysis of the proposed methodology. The study focuses on estimating the total collision probability in multi-event conjunctions and comparing the analytical estimation against the actual approximations, considering the physical and geometric factors introduced in Section 2.3. Each case is supported by the needed physical interpretation, and mathematical analysis. Some of these cases will be developed into the Chapter 3, to verify the real behaviour.

The cases are chosen to isolate and quantify the impact of each correlation source. They are also designed to maintain continuity with the simplified "Toy Problems" analysed in Section 2.1, allowing a clear transition from abstract mathematical models to orbital simulations.

2.4.1. Analysis of Study Cases

Three primary cases are considered to explore how collision risk responds to different conditions.

Case 1: Influence of the Common Primary Object

In this scenario, a single primary satellite interacts with two distinct secondary objects at epochs t_1 and t_2. The initial state errors of all objects are assumed to be independent, and no common environmental uncertainty sources are considered. Consequently, the exclusive source of statistical correlation between the two events is the position uncertainty of the primary satellite.

Regarding the complete covariance matrix for both events, the diagonal blocks $\mathbf{\Sigma}_{Z_k}$, for $k \in \{1, 2\}$, are defined as in the general construction presented in Section 2.3.1, where each block represents the sum of the primary and secondary position covariances at the corresponding Time of Closest Approach (TCA). The propagation of the full state covariance between both TCAs follows Eq. (2.91). As a result, the cross-correlation block between the two encounters is derived using the linear mapping between t_1 and t_2, leading to Eq. (2.98).

It must be emphasized that Eq. (2.98) depends exclusively on the primary covariance at t_1 and the State Transition Matrix (STM) between t_1 and t_2. Because the secondary objects are independent, no secondary terms are present in the off-diagonal block.

Once the complete covariance is defined, it is transformed into the respective conjunction planes (B-planes) via rotation and geometric projection, as defined in Eq. (2.77). This projected form of the global covariance matrix is the one utilized in the analytic method. If the events were completely independent, the relative position covariance of each encounter would simply be the respective diagonal block of the complete projected covariance matrix $\mathbf{\Sigma}^*_Z$. However, in realistic scenarios where a physical correlation exists between the events, the uncertainty of the second encounter is determined by the Schur complement introduced in Eq. (2.80):

$$\mathbf{\Sigma}^*_{Z_2|Z_1} = \mathbf{\Sigma}^*_{Z_2} - \mathbf{\Sigma}^*_{Z_{21}}\mathbf{\Sigma}^{*-1}_{Z_1}\mathbf{\Sigma}^*_{Z_{12}} \tag{2.111}$$

Before evaluating this conditional covariance, the structure of the projected covariance matrix must be rigorously established. The unprojected covariance matrix $\mathbf{\Sigma}_Z$ is mathematically defined as a symmetric positive semidefinite matrix, representing physical orbital uncertainty. The transformation of this matrix into the respective B-planes involves rotations, denoted by $\mathbf{C}_1$ and $\mathbf{C}_2$, and a 2D geometric projection, denoted by $\mathbf{T}^*$. The complete transformation is expressed as

$$\mathbf{\Sigma}^*_Z = \mathbf{T}\mathbf{\Sigma}_Z\mathbf{T}^\top = \begin{bmatrix} \mathbf{T}^*\mathbf{C}_1\mathbf{\Sigma}_{Z_1}\mathbf{C}_1^\top\mathbf{T}^{*\top} & \mathbf{T}^*\mathbf{C}_1\mathbf{\Sigma}_{Z_{1,2}}\mathbf{C}_2^\top\mathbf{T}^{*\top} \\ \mathbf{T}^*\mathbf{C}_2\mathbf{\Sigma}_{Z_{1,2}}^\top\mathbf{C}_1^\top\mathbf{T}^{*\top} & \mathbf{T}^*\mathbf{C}_2\mathbf{\Sigma}_{Z_2}\mathbf{C}_2^\top\mathbf{T}^{*\top} \end{bmatrix} \tag{2.112}$$

Linear algebra dictates that any congruence transformation of the form $A\mathbf{\Sigma}A^\top$ preserves the positive semidefinite property of the original matrix. For any arbitrary vector v, the quadratic form evaluates to $(A^\top v)^\top\mathbf{\Sigma}(A^\top v)$, which is guaranteed to be non-negative because $\mathbf{\Sigma}$ is positive semidefinite. Consequently, the rotation and subsequent projection do not alter the fundamental geometric properties of the uncertainty. The individual projected diagonal blocks, $\mathbf{\Sigma}^*_{Z_k}$, remain symmetric positive semidefinite. In practical operational scenarios, unless the position uncertainty is exactly zero in a specific direction, these blocks are strictly positive definite and invertible.

The subtracted term on the right-hand side of Eq. (2.111) represents the mathematical variance reduction provided by the knowledge of the first encounter. By construction, the cross-covariance block satisfies $\mathbf{\Sigma}^*_{Z_{21}} = {\mathbf{\Sigma}^*_{Z_{12}}}^\top$. Therefore, the reduction term can be rewritten as ${\mathbf{\Sigma}^*_{Z_{12}}}^\top{\mathbf{\Sigma}^*_{Z_1}}^{-1}\mathbf{\Sigma}^*_{Z_{12}}$.

This expression follows the standard quadratic form $A^\top MA$, where the core matrix $M =$

${\boldsymbol{\Sigma}^*_{Z_1}}^{-1}$. Because the inverse of a positive definite covariance matrix is also strictly positive definite, M is positive definite. To prove that the entire variance reduction term is positive semidefinite, an arbitrary vector x is applied

$$x^\top {\boldsymbol{\Sigma}^*_{Z_{12}}}^\top {\boldsymbol{\Sigma}^*_{Z_1}}^{-1} \boldsymbol{\Sigma}^*_{Z_{12}} x = (\boldsymbol{\Sigma}^*_{Z_{12}} x)^\top {\boldsymbol{\Sigma}^*_{Z_1}}^{-1} (\boldsymbol{\Sigma}^*_{Z_{12}} x) \geq 0 \tag{2.113}$$

This derivation proves that the subtraction term is strictly non-negative. It may fail to be strictly positive only along specific directions x where the cross-covariance mapping yields a null vector ($\boldsymbol{\Sigma}^*_{Z_{12}} x = 0$). As a result, the Schur complement subtracts a positive semidefinite matrix from the marginal covariance $\boldsymbol{\Sigma}^*_{Z_2}$, modelling the physical reduction of uncertainty without violating the geometric properties of the covariance.

Therefore, $\boldsymbol{\Sigma}^*_{Z_2|Z_1}$ is always mathematically smaller than or equal to $\boldsymbol{\Sigma}^*_{Z_2}$. The reduction is strictly non-zero whenever $\boldsymbol{\Sigma}^*_{Z_{12}} \neq 0$, which occurs as long as the primary covariance at t_1 is non-zero.

To evaluate why the variance reduction is typically partial rather than complete, an analysis of the characteristic orders of magnitude is presented. The diagonal blocks scale with the combined primary and secondary covariances at their respective epochs. Conversely, the cross-covariance term is governed by the primary object's uncertainty at t_1 and its subsequent linear mapping through the STM.

To estimate the magnitude of this cross-covariance, the individual contributions of the position and velocity terms must be considered. In scenarios involving short propagation intervals, the numerical values of the velocity-related covariances ($\boldsymbol{\Sigma}_{rv_p}$) are generally orders of magnitude smaller than the pure position covariances ($\boldsymbol{\Sigma}_{r_p}$). Furthermore,in the ideal case of a short time interval between TCAs the position-to-position block of the STM is approximately equivalent to the identity matrix ($\boldsymbol{\Phi}_{r_p} \approx \mathbf{I}$), while the velocity-to-position mapping block ($\boldsymbol{\Phi}_{rv_p}$) remains bounded.

Under these conditions, the velocity-coupled term becomes negligible compared to the primary position term. Denoting by $\mathcal{O}(\cdot)$ the characteristic magnitude of a covariance block, the overall cross-covariance scales with the initial position covariance of the primary object

$$\mathcal{O}(\boldsymbol{\Sigma}^*_{Z_{12}}) \sim \mathcal{O}(\boldsymbol{\Sigma}_{Z_{12}}) \sim \mathcal{O}(\boldsymbol{\Sigma}_{r_p}(t_1)) \tag{2.114}$$

Similarly, the diagonal blocks of the covariance scale as

$$\mathcal{O}(\boldsymbol{\Sigma}^*_{Z_k}) \sim \mathcal{O}(\boldsymbol{\Sigma}_{Z_k}) \sim \mathcal{O}(\boldsymbol{\Sigma}_{r_p}(t_k) + \boldsymbol{\Sigma}_{r_{sk}}(t_k)) \tag{2.115}$$

Three significant physical regimes can then be distinguished based on these magnitudes. If the secondary uncertainties dominate

$$\mathcal{O}(\mathbf{\Sigma}_{r_p}) \ll \mathcal{O}(\mathbf{\Sigma}_{r_{s1}}), \mathcal{O}(\mathbf{\Sigma}_{r_{s2}}) \tag{2.116}$$

the diagonal blocks are governed primarily by the secondary covariances. In that case, the inverse matrix approximates to

$$\mathbf{\Sigma}_{Z_k}^{*-1} \approx \mathbf{\Sigma}_{r_{sk}}^{-1} \tag{2.117}$$

and the Schur reduction term scales as

$$\mathcal{O}\left(\mathbf{\Sigma}_{Z_{21}}^{*}\mathbf{\Sigma}_{Z_1}^{*-1}\mathbf{\Sigma}_{Z_{12}}^{*}\right) \sim \frac{\mathcal{O}(\mathbf{\Sigma}_{r_p})^2}{\mathcal{O}(\mathbf{\Sigma}_{r_{s1}})} \tag{2.118}$$

Since this quantity is of second order with respect to the small primary covariance, the mathematical reduction is minimal compared to $\mathbf{\Sigma}_{Z_2}^{*}$, yielding

$$\mathbf{\Sigma}_{Z_2|Z_1}^{*} \approx \mathbf{\Sigma}_{Z_2}^{*} \tag{2.119}$$

Conversely, if the primary covariance is of the same order as the secondary covariances

$$\mathcal{O}(\mathbf{\Sigma}_{Z_1}^{*}) \sim \mathcal{O}(\mathbf{\Sigma}_{r_p}) \tag{2.120}$$

the Schur reduction term scales as

$$\mathcal{O}\left(\mathbf{\Sigma}_{Z_{21}}^{*}\mathbf{\Sigma}_{Z_1}^{*-1}\mathbf{\Sigma}_{Z_{12}}^{*}\right) \sim \mathcal{O}(\mathbf{\Sigma}_{r_p}) \tag{2.121}$$

which is of the same order as the primary contribution inside $\mathbf{\Sigma}_{Z_2}^{*}$. In this regime, the reduction is noteworthy but cannot eliminate the full covariance because the independent term $\mathbf{\Sigma}_{r_{s2}}(t_2)$ remains unaffected.

Finally, if the primary covariance strongly dominates over both secondary objects

$$\mathcal{O}(\mathbf{\Sigma}_{r_p}) \gg \mathcal{O}(\mathbf{\Sigma}_{r_{s1}}), \mathcal{O}(\mathbf{\Sigma}_{r_{s2}}) \tag{2.122}$$

the diagonal blocks are dominated entirely by the primary uncertainties. The inverse block simplifies to

$$\boldsymbol{\Sigma}^{*-1}_{Z_k} \approx \boldsymbol{\Sigma}^{-1}_{r_p}(t_k) \tag{2.123}$$

and the Schur reduction term scales directly with the primary covariance at the first encounter

$$\mathcal{O}\left(\boldsymbol{\Sigma}^{*}_{Z_{21}}\boldsymbol{\Sigma}^{*-1}_{Z_1}\boldsymbol{\Sigma}^{*}_{Z_{12}}\right) \sim \mathcal{O}(\boldsymbol{\Sigma}_{r_p}(t_1)) \tag{2.124}$$

Because the reduction is on the order of $\boldsymbol{\Sigma}_{r_p}(t_1)$, while the unconditioned second block scales with $\boldsymbol{\Sigma}_{r_p}(t_2)$, a significant portion of the primary uncertainty is cancelled. However, because covariance inherently grows over time due to orbital dynamics ($\boldsymbol{\Sigma}_{r_p}(t_2) > \boldsymbol{\Sigma}_{r_p}(t_1)$), the cancellation is never complete. Therefore

$$\boldsymbol{\Sigma}^{*}_{Z_2|Z_1} < \boldsymbol{\Sigma}^{*}_{Z_2} \tag{2.125}$$

The total vanishing of $\boldsymbol{\Sigma}^{*}_{Z_2|Z_1}$ would require that the entire uncertainty in Z_2 could be perfectly explained through its correlation with Z_1. This is physically impossible in this scenario because the second secondary object introduces a completely independent error source. Even in the theoretical limit where the primary dominates both diagonal blocks, the Schur complement removes only the specific component of $\boldsymbol{\Sigma}^{*}_{Z_2}$ that is statistically coupled to Z_1 via the cross-covariance matrix $\boldsymbol{\Sigma}^{*}_{Z_{12}}$.

This mathematical framework explains why, in Case 1, the conditioned covariance is always smaller than the unconditional one but remains strictly positive and significant: the correlation is driven only by the primary object, while each secondary object contributes an independent uncertainty component that cannot be inferred from the other encounter.

Another critical factor preventing the total vanishing of the Schur complement is the State Transition Matrix present in the definition of $\boldsymbol{\Sigma}^{*}_{Z_{12}}$. This matrix multiplies the primary covariance factor; consequently, while the established magnitude trends maintain their validity, the actual variance reduction produced by the Schur complement may be less noteworthy depending on how drastically the STM deforms the uncertainty ellipsoid over the propagation interval.

The conditioned mean of the second encounter is obtained from the standard Gaussian conditioning formula

$$\boldsymbol{\mu}^{*}_{Z_2|Z_1} = \boldsymbol{\mu}^{*}_{Z_2} + \boldsymbol{\Sigma}^{*}_{Z_{21}}\boldsymbol{\Sigma}^{*-1}_{Z_1}\left(\mathbf{z}^{*}_1 - \boldsymbol{\mu}^{*}_{Z_1}\right) \tag{2.126}$$

Because the cross-covariance block $\boldsymbol{\Sigma}^{*}_{Z_{21}}$ is determined by the propagated primary covariance and its STM, the predicted mean for the second encounter is modified exclusively by the primary state error observed at the first encounter. The position uncertainty introduced by the first secondary object has no influence on the prediction of the second encounter.

The magnitude of this mean correction term is estimated as

$$\mathcal{O}\left(\boldsymbol{\Sigma}^*_{Z_{21}}\boldsymbol{\Sigma}^{*-1}_{Z_1}\right) \sim \frac{\mathcal{O}(\boldsymbol{\Sigma}_{r_p})}{\mathcal{O}(\boldsymbol{\Sigma}_{Z_1})} \tag{2.127}$$

If the primary covariance is smaller than the secondary covariance at the first encounter, this correction ratio is minimal, and the conditioned mean is maintained close to the nominal mean $\boldsymbol{\mu}^*_{Z_2}$. Conversely, if the primary covariance is dominant, the specific deviation observed at the first encounter results in a proportional position shift in the second encounter prediction.

The joint probability of the simultaneous events is evaluated utilizing the conditional factorization of the joint Gaussian distribution associated with the block covariance matrix $\boldsymbol{\Sigma}^*_Z$, as defined in Eq. (2.88). In this analytical formulation, the second integral is evaluated using the conditioned mean and the conditioned covariance, derived respectively from the linear shift term and the Schur complement.

Consequently, the statistical dependence between the two encounters is caused by the cross-covariance block $\boldsymbol{\Sigma}^*_{Z_{12}}$. This block alters both the position dispersion and the central location of the second-encounter distribution due to the shared initial uncertainty of the primary object.

The effect of this conditioning is manifested through two distinct mechanisms. First, the subtraction inherent to $\boldsymbol{\Sigma}^*_{Z_2|Z_1}$ concentrates the conditional probability density relative to the unconditioned density. Second, the linear shift of $\boldsymbol{\mu}^*_{Z_2|Z_1}$ displaces the centre of the distribution as a direct function of the observed position variable z_1.

When the primary covariance is relatively small, both the concentration and the displacement effects are weak, and the joint probability approaches the simple product of the independent probabilities. However, when the primary covariance is numerically comparable to, or greater than, the secondary covariances, the nested integral departs significantly from the independent approximation. The occurrence of a position deviation at the first encounter modifies the expected location of the second encounter distribution through the shared primary uncertainty.

Therefore, in Case 1, the deviation from statistical independence in the final calculated probability is governed by the magnitude of the primary covariance relative to the secondary covariances, and by the structural deformation induced by the STM mapping the primary errors between the two epochs.

Case 2: Influence of a Common Secondary Object

In this scenario, a single primary satellite interacts with the same secondary object at epochs t_1 and t_2. The initial state errors of all objects are assumed to be independent, and no common environmental uncertainty sources are considered. Consequently, now the source of statistical correlation between the two events comes from both satellites.

Regarding the complete covariance matrix for both events, the diagonal blocks $\mathbf{\Sigma}_{Z_k}$, for $k \in \{1, 2\}$, are defined as in the general construction presented in Section 2.3.2, where each block represents the sum of the primary and secondary position covariances at the corresponding Time of Closest Approach (TCA). The propagation of the full state covariance between both TCAs follows Eq. (2.91). As a result, the cross-correlation block between the two encounters is derived using the linear mapping between t_1 and t_2, leading to Eq. (2.105).

It must be emphasized that Eq. (2.105) depends on the primary and secondary covariances at t_1 and the State Transition Matrix (STM) between t_1 and t_2.

Following the construction of the 3D position covariance, the geometric transformations are applied. As demonstrated in Case 1, the sequence of rotations and 2D projections onto the respective B-planes preserves the positive semidefinite properties of the original matrices. Consequently, the projected diagonal blocks $\mathbf{\Sigma}^*_{Z_k}$ and the cross-covariance block $\mathbf{\Sigma}^*_{Z_{12}}$ remain symmetric positive semidefinite and mathematically robust for the subsequent conditioning operations.

The conditional covariance of the second encounter, is defined by the Schur complement

$$\mathbf{\Sigma}^*_{Z_2|Z_1} = \mathbf{\Sigma}^*_{Z_2} - \mathbf{\Sigma}^*_{Z_{21}} \mathbf{\Sigma}^{*-1}_{Z_1} \mathbf{\Sigma}^*_{Z_{12}} \tag{2.128}$$

In contrast to Case 1, an important structural distinction arises in the magnitude analysis. Because both the primary and secondary uncertainties are incorporated into the diagonal blocks and the off-diagonal blocks, the mathematical reduction provided by the Schur complement does not depend on the relative ratio between the primary and secondary covariances. Whether one object possesses a significantly larger uncertainty than the other is irrelevant in this scenario, as:

$$\mathcal{O}(\boldsymbol{\Sigma}^*_{Z_{12}}) \sim \mathcal{O}(\boldsymbol{\Sigma}_{Z_{12}}) \sim \mathcal{O}(\boldsymbol{\Sigma}_{r_p}(t_1) + \boldsymbol{\Sigma}_{r_s}(t_1)) \tag{2.129}$$

$$\mathcal{O}(\boldsymbol{\Sigma}^*_{Z_k}) \sim \mathcal{O}(\boldsymbol{\Sigma}_{Z_k}) \sim \mathcal{O}(\boldsymbol{\Sigma}_{r_p}(t_k) + \boldsymbol{\Sigma}_{r_s}(t_k)) \tag{2.130}$$

To understand the boundaries of this conditional covariance, a purely ideal theoretical case is analysed first. In this ideal limit, three assumptions are imposed. First, the orbital propagation is completely free of environmental perturbations, meaning the STM describes the dynamic evolution exactly. Second, the velocity covariances are assumed to tend to zero, leaving only the initial position covariances. Third, it is assumed that the re-encounter occurs exactly one full orbital period later. Under these unperturbed conditions, the orbits remain constant, and the State Transition Matrices evaluated over exactly one revolution approximate the identity matrix ($\boldsymbol{\Phi}_p \approx \mathbf{I}$ and $\boldsymbol{\Phi}_s \approx \mathbf{I}$).

Under these ideal conditions, the cross-covariance block becomes numerically identical to the diagonal blocks. The subtraction term in the Schur complement perfectly cancels the marginal covariance of the second encounter. Consequently, the conditional covariance tends to the null matrix

$$\boldsymbol{\Sigma}^*_{Z_2|Z_1} \rightarrow \mathbf{0} \tag{2.131}$$

However, operational realities introduce significant deviations from this ideal limit. When external orbital perturbations are considered, the true dynamics become more complicated, and the STM represents only a first-order approximation. Furthermore, due to these perturbations, the successive encounters do not occur in perfectly identical geometric conditions, causing the STMs to deviate from the identity matrix. Finally, the initial velocity covariances are never strictly zero, introducing coupled position dispersion over time. Due to these combined factors, the cross-terms do not perfectly cancel the diagonal block. The Schur complement does not vanish to zero, although it remains relatively small.

The conditional mean of the second encounter dictates the expected location of the second event based on the first, which is used when solving numerically the full integral

$$\boldsymbol{\mu}^*_{Z_2|Z_1} = \boldsymbol{\mu}^*_{Z_2} + \boldsymbol{\Sigma}^*_{Z_{21}} \boldsymbol{\Sigma}^{*-1}_{Z_1} \left(\mathbf{z}^*_1 - \boldsymbol{\mu}^*_{Z_1}\right) \tag{2.132}$$

The matrix

$$\mathbf{K}^* = \boldsymbol{\Sigma}^*_{Z_{21}} \boldsymbol{\Sigma}^{*-1}_{Z_1} \tag{2.133}$$

acts as a linear gain that maps deviations in the first B-plane to predicted deviations in the second one.

In the ideal limit characterized previously, the linear gain matrix approaches the identity matrix

$$\mathbf{K}^* \approx \mathbf{I} \tag{2.134}$$

and therefore

$$\boldsymbol{\mu}^*_{Z_2|Z_1} \approx \boldsymbol{\mu}^*_{Z_2} + \left(\mathbf{z}^*_1 - \boldsymbol{\mu}^*_{Z_1}\right) \tag{2.135}$$

If the nominal relative means of both encounters are assumed to be equal ($\boldsymbol{\mu}^*_{Z_2} = \boldsymbol{\mu}^*_{Z_1}$), the conditioned mean interpolates directly around the origin, matching the relative position studied in each step of integration in the first encounter ($\boldsymbol{\mu}^*_{Z_2|Z_1} \approx \mathbf{z}^*_1$).

More generally, independently of which object contributes more to the total covariance, the conditional mean represents the best linear prediction of $\mathbf{Z}^*_2$ from $\mathbf{Z}^*_1$. When the Schur complement $\boldsymbol{\Sigma}^*_{Z_2|Z_1}$ is small, this prediction becomes highly accurate. Conversely, in realistic perturbed scenarios, the gain matrix deviates from the identity, and the nominal means are not perfectly equal, resulting in a displaced conditioned mean.

The impact of this conditioning is finally evaluated through the total joint collision probability, expressed as a nested integral

$$P(A_1 \cap A_2) = \int_{A_1} f_{Z_1}(\mathbf{z}^*_1) \left(\int_{A_2} f_{Z_2|Z_1}(\mathbf{z}^*_2 \mid \mathbf{z}^*_1)\, d\mathbf{z}^*_2 \right) d\mathbf{z}^*_1 \tag{2.136}$$

In the theoretical ideal case where the Schur complement approaches the null matrix, the inner conditional probability density function loses the dispersion. The distribution converges to a Dirac delta function centred strictly on the conditioned mean

$$\boldsymbol{\Sigma}^*_{Z_2|Z_1} \to \mathbf{0} \quad \Longrightarrow \quad f_{Z_2|Z_1}(\mathbf{z}^*_2 \mid \mathbf{z}^*_1) \to \delta\big(\mathbf{z}^*_2 - \boldsymbol{\mu}^*_{Z_2|Z_1}(\mathbf{z}^*_1)\big) \tag{2.137}$$

Substituting this limit into Eq. (2.136), the inner integral reduces to evaluating whether the conditional mean itself satisfies the second collision condition:

$$\int_{A_2} \delta\big(\mathbf{z}^*_2 - \boldsymbol{\mu}^*_{Z_2|Z_1}(\mathbf{z}^*_1)\big)\, d\mathbf{z}^*_2 = \mathbf{1}_{A_2}\big(\boldsymbol{\mu}^*_{Z_2|Z_1}(\mathbf{z}^*_1)\big) \tag{2.138}$$

where $\mathbf{1}_{A_2}$ is the indicator function of the second collision domain.

Therefore, in the regime of a small Schur complement, the joint probability approaches

$$P(A_1 \cap A_2) \approx \int_{A_1} f_{Z_1}(\mathbf{z}_1^*)\, \mathbf{1}_{A_2}\big(\boldsymbol{\mu}^*_{Z_2|Z_1}(\mathbf{z}_1^*)\big)\, d\mathbf{z}_1^* \tag{2.139}$$

This shows that the second encounter no longer contributes an independent stochastic dimension. Instead, for each admissible $\mathbf{z}_1^*$, the occurrence of the second collision is determined primarily by whether the propagated conditional mean lies inside A_2, with only a small correction due to the residual covariance $\boldsymbol{\Sigma}^*_{Z_2|Z_1}$. While this Dirac delta approximation provides a theoretical framework to understand the coupling between identical recurrent events, the perturbations and STM deviations inherent to real space operations ensure that the residual Schur complement is small but never zero, requiring the rigorous evaluation of the complete Gaussian distribution.

Case 3: Influence of Atmospheric Model Uncertainty

This scenario evaluates the impact of environmental uncertainty, as detailed in Section 2.3.3. In addition to the initial state errors studied in previous cases, a new level of statistical coupling is introduced. This coupling is caused by atmospheric density errors, which affect the aerodynamic drag of all satellites at the same time.

The random variable ϵ_ρ acts as a shared source of uncertainty for all objects involved in the conjunction. Its physical effect is determined by the sensitivity vectors. The diagonal covariance blocks are defined in Eq. (2.108), and the off-diagonal covariance is defined in Eq. (2.110).

The sensitivity vectors $\mathbf{S}_{rel,k}$ measure how the relative position at each encounter changes due to a density error. Their direction and size depend on the ballistic coefficients, orbital geometry, and propagation time. If the drag effects on both objects are very similar, the relative sensitivity approaches zero, which minimizes the atmospheric contribution. If the drag effects are very different, this environmental term is amplified.

The off-diagonal block captures the total statistical correlation between the events. The atmospheric term acts as an extra component. Its sign and size depend on the angle between $\mathbf{S}_{rel,1}$ and $\mathbf{S}_{rel,2}$. If the sensitivity vectors point in the same direction, the environmental effect increases the correlation. If they point in opposite directions, it reduces the correlation.

The conditional covariance of the second encounter is evaluated using the Schur complement

$$\boldsymbol{\Sigma}^*_{Z_2|Z_1} = \boldsymbol{\Sigma}^*_{Z_2} - \boldsymbol{\Sigma}^*_{Z_{21}}\boldsymbol{\Sigma}^{*-1}_{Z_1}\boldsymbol{\Sigma}^*_{Z_{12}} \tag{2.140}$$

To understand the impact of this environmental covariance, its size is compared to the initial state uncertainty.

If the atmospheric error is very small compared to the state covariance

$$\mathcal{O}\big(\boldsymbol{\Sigma}_{r_p}\big) \gg \mathcal{O}\big(\mathbf{S}_{rel,k}\mathbf{S}^\top_{rel,k}\sigma^2_\rho\big) \tag{2.141}$$

the environmental addition to the cross-covariance is negligible. In this situation, the covariance reduction is driven entirely by the state correlation analyzed in Case 1 or Case 2.

Conversely, if the drag uncertainty becomes comparable to or larger than the state errors

$$\mathcal{O}\big(\mathbf{S}_{rel,k}\mathbf{S}^\top_{rel,k}\sigma^2_\rho\big) \gtrsim \mathcal{O}\big(\boldsymbol{\Sigma}_{r_p}\big) \tag{2.142}$$

the environmental term significantly changes the total covariance matrices.

An important mathematical feature of this environmental error must be explained. The atmospheric error covariance matrices are built by multiplying a column vector by a row vector. For the diagonal blocks, a sensitivity vector is multiplied by its own transpose ($\mathbf{S}_{rel,k}\mathbf{S}^\top_{rel,k}$). For the off-diagonal blocks, the first sensitivity vector is multiplied by the transpose of the second ($\mathbf{S}_{rel,1}\mathbf{S}^\top_{rel,2}$). In linear algebra, this operation always produces a matrix with a rank of one.

Physically, this means that the position uncertainty added by the atmospheric drag only moves along a single straight line. For the second encounter, this line is defined by the sensitivity vector $\mathbf{S}_{rel,2}$. As a result, when the Schur complement reduces the variance, the mathematical subtraction only works along that exact line. Any direction perpendicular to the sensitivity vector remains completely unaffected, because the atmospheric error does not push the satellite in those directions.

Therefore, the atmospheric correlation alone can never reduce the conditioned covariance to zero ($\mathbf{0}$). It only removes the uncertainty in one specific dimension. The original state uncertainty in all other directions remains unchanged.

The conditioned mean gives the expected location of the second event based on the first event

$$\boldsymbol{\mu}^*_{Z_2|Z_1} = \boldsymbol{\mu}^*_{Z_2} + \boldsymbol{\Sigma}^*_{Z_{21}}\boldsymbol{\Sigma}^{*-1}_{Z_1}\left(\mathbf{z}^*_1 - \boldsymbol{\mu}^*_{Z_1}\right) \tag{2.143}$$

During the numerical evaluation of the integral, the variable $\mathbf{z}_1^*$ sweeps across the first B-plane. The distance from the nominal mean is measured by $(\mathbf{z}_1^* - \boldsymbol{\mu}_{Z_1}^*)$. When this distance is projected onto the first sensitivity vector $(\mathbf{S}_{rel,1}^*)$, the conditional mean of the second encounter is shifted as a function of the first encounter's variable. Because the environmental matrix has rank one, this shift only happens along the axis of the second sensitivity vector $(\mathbf{S}_{rel,2}^*)$. This shift moves the expected location of the second event closer to or further from the collision region.

The joint collision probability is evaluated using the nested integral

$$P(A_1 \cap A_2) = \int_{A_1} f_{Z_1}(\mathbf{z}_1^*) \left(\int_{A_2} f_{Z_2|Z_1}(\mathbf{z}_2^* \mid \mathbf{z}_1^*) \, d\mathbf{z}_2^* \right) d\mathbf{z}_1^* \tag{2.144}$$

To understand the pure effect of the atmospheric correlation, a theoretical limit is considered. In this limit, the initial state errors are set to zero, so the atmospheric error ϵ_ρ is the only source of uncertainty. In this extreme case, knowing the exact position at the first encounter $(\mathbf{z}_1^*)$ perfectly reveals the value of the drag error. Because the drag error is known, the exact position of the second encounter becomes completely certain. The conditional covariance matrix becomes zero $(\boldsymbol{\Sigma}_{Z_2|Z_1}^* \to \mathbf{0})$, and the probability distribution becomes a single point

$$f_{Z_2|Z_1}(\mathbf{z}_2^* \mid \mathbf{z}_1^*) \to \delta\big(\mathbf{z}_2^* - \boldsymbol{\mu}_{Z_2|Z_1}^*(\mathbf{z}_1^*)\big) \tag{2.145}$$

Using this theoretical limit simplifies the inner integral to a basic geometric check. It only tests if the drag-induced shift crosses the second collision area A_2.

However, in real operations, the state uncertainties $\boldsymbol{\Sigma}_{Z_k}^*$ are never zero. The environmental term only acts as an addition to the existing correlation. The conditional covariance $\boldsymbol{\Sigma}_{Z_2|Z_1}^*$ maintains a strictly positive 2D dispersion. The mathematical reduction only shows how the shared atmosphere helps predict the second encounter based on the first. Therefore, the full evaluation of the nested integral is always required to accurately calculate the real probability.

3 | Results

This chapter presents the numerical results obtained from the models developed in this thesis. The analysis is divided into two main sections. First, the simplified two-dimensional "toy problem" is evaluated to intuitively show how different sources of correlation affect the collision risk. Second, the complete three-dimensional orbital model is validated using Monte Carlo simulations and tested across realistic operational scenarios. The overall goal is to prove the accuracy of the proposed analytical method and to demonstrate the difference between the methods that neglect the correlation between the different events presented into the multiple-encounter scenarios proposed, and the analytic formula derived in this thesis.

3.1. Toy Problem results

These initial results are important to isolate the basic physical and statistical factors that create correlation between events, avoiding the geometric complexity of three-dimensional cases. By solving these basic cases, the isolated effects of different uncertainty sources—such as a common vehicle, a repeated pedestrian, or external forces—can be clearly understood and visualized. Ultimately, the "toy problem" validates the core mathematical logic and builds a solid, intuitive foundation for the subsequent 3D orbital analysis.

3.1.1. Experimental Results

This section presents both the analytical results and the Monte-Carlo simulations that validate the formulation of the two-dimensional "toy problem". The objective is to verify the consistency of the analytical expressions derived in the previous section, to evaluate the probabilistic limits previously defined, and to illustrate the influence of different uncertainty configurations.

The analytical results are obtained from the explicit expressions of $P(A_1)$, $P(A_2)$, and $P(A_1 \cap A_2)$, under the specific assumptions defined for each case. These expressions are used to compute the total collision probability $P(A_1 \cup A_2)$, which is then compared against the theoretical bounds $\max\{P(A_1),\, P(A_2)\} \leq P(A_1 \cup A_2) \leq \min\{P(A_1) + P(A_2),\, 1\}$. as well as with the simplified formulations $P(A_1 \cap A_2) = P(A_1)\, P(A_2)$ (for no correlation cases) and $P(A_1 \cup A_2) = P(A_1) + P(A_2)$ (for no correlation cases and individual probabilities much smaller than one).

To complement the analytical approach, Monte Carlo simulations are performed to estimate the empirical collision probabilities. These simulations serve two purposes: first, to confirm the analytical solutions within statistical uncertainty, and second, to visualize the probabilistic behaviour of the system under different configurations of means, standard deviations, and correlation between the random variables.

This approach requires an estimation about the number of samples required to obtain a decent result. To obtain this approximation the formula (1.9) will be used [16], for a confidence level of 95%, assuming a probability of collision on the order of 10^{-2} and a relative error of 1%, is on the order of 10^7.

Case 1: Deterministic vehicle, uncertain pedestrian lateral position

After deriving the analytical expressions, the results are numerically checked by directly solving the double integral (that is not strictly necessary due to the analytical simplification, but it has been done to verify the analytical development and to maintain a normalized method in all the cases) in Eq. (2.14) and comparing it with the analytically simplified product expression in Eq. (2.21). Both methods give the same value of $P(A_1 \cap A_2)$ within numerical accuracy, confirming that the factorization for independent variables ($\rho = 0$) is accurate.

Even though both events are independent and uncorrelated, the total collision probability cannot always be simplified as the direct sum of the individual ones. The expression $P(A_1 \cup A_2) \approx P(A_1) + P(A_2)$ gives a slightly higher value because it ignores the small but nonzero probability of both collisions happening together. Therefore, it can be seen as a conservative approximation. In all the tested cases, the total probability computed from Eq. (2.22) stays within the theoretical limits $\max\{P(A_1),\, P(A_2)\} \leq P(A_1 \cup A_2) \leq P(A_1) + P(A_2)$

To illustrate this, Tables 3.1 and 3.2 includes all the parameters of each pedestrian and the vehicle to allow the correct reproduction of the experiments.

Table 3.1: Geometrical parameters: initial states, vehicle width and TCA state.

Category	Parameter [units]	Value
Initial state	Vehicle $\mathbf{r}$ [m]; $\mathbf{v}$ [m/s]	$[0, 0]; [0, 10]$
	Ped. 1 $\mathbf{r}$ [m]; $\mathbf{v}$ [m/s]	$[-10, 100]; [1.2, 0.0]$
	Ped. 2 $\mathbf{r}$ [m]; $\mathbf{v}$ [m/s]	$[10, 200]; [-0.4, 0.0]$
Geometry	Vehicle width [m]	2
TCA state	Event 1 TCA [s]; $\boldsymbol{\mu}_Z$ [m]	$10.0; [2.02, 0]$
	Event 2 TCA [s]; $\boldsymbol{\mu}_Z$ [m]	$20.0; [2.20, 0]$

Table 3.2: Standard deviations of initial states and TCA state.

Category	Parameter [units]	Value
Initial state	Vehicle σ_x [m]	0.00
	Pedestrian 1 σ_x [m]	0.45
	Pedestrian 2 σ_x [m]	0.60
TCA state	Event 1 σ_x [m]	0.45
	Event 2 σ_x [m]	0.60

The results of the simulation are presented in Table 3.3, which reports the individual collision probabilities, the joint probability, and the total probability obtained from both the analytical expression and the Monte Carlo simulations. The agreement between the results confirms that the model behaves as expected, and that the errors introduced by the simplified formulas remain small.

Table 3.3: Comparison between analytical, Monte Carlo, and simplified results.

Probability quantities	Analytical results [-]	Monte-Carlo results [-]	Simplified formulas [-]	Relative error [%]
$\mathrm{P}(A_1)$	0.0117	0.0118	-	-
$\mathrm{P}(A_2)$	0.0228	0.0228	-	-
$\mathrm{P}(A_1 \cap A_2)$	0.0003	0.0003	0.0003	1.42e-15
$\mathrm{P}(A_1 \cup A_2)$	0.0342	0.0343	0.0342	0.00e+00

The Monte Carlo simulation was carried out using random samples of X_1 and X_2 were generated following Eq. (2.6), and the collision condition in Eq. (2.12) was tested for each sample. The collision probabilities estimated from the simulation match the analytical values very closely. In addition, the scatter plot of the sampled pairs (Z_1, Z_2), shown in the left plot of Fig. 3.1, shows no visible correlation, confirming that both variables are indeed independent. The right plot represents the normalized relative position of the car with respect to the pedestrian, simulating the 1D extension of the B-plane used in the real 3D case to represent the relative position of the space objects in the TCA.

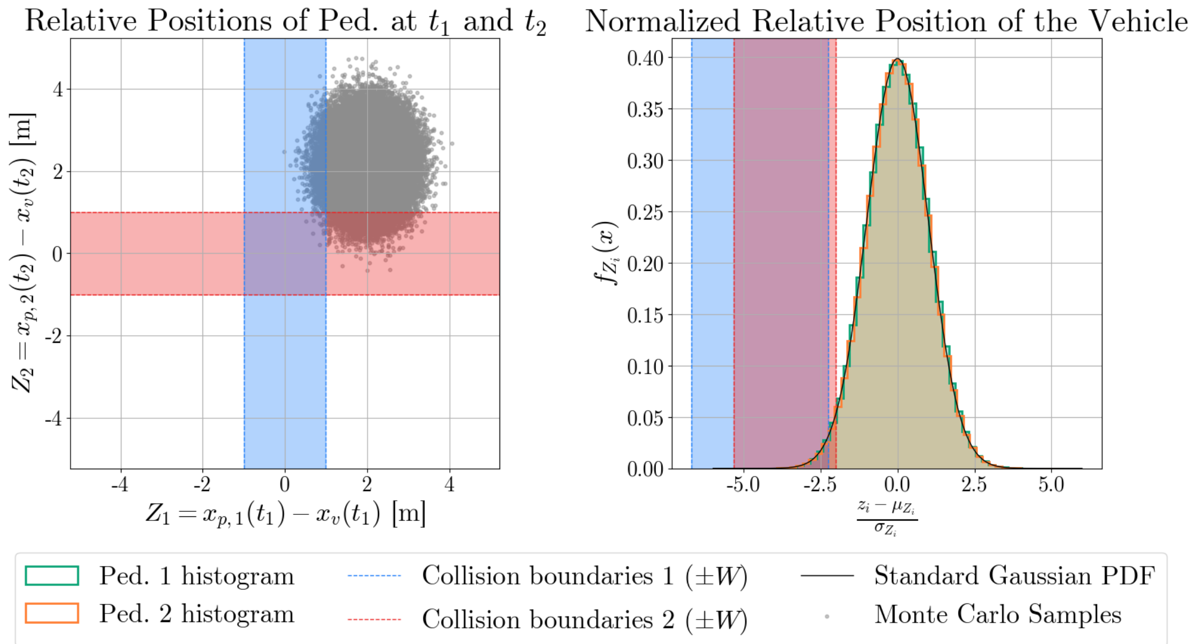

Figure 3.1: Monte Carlo validation for Case 1. The sampled pairs (Z_1, Z_2) show no correlation, confirming independence. Analytical and simulated probabilities agree within statistical noise.

In summary, this first case works as a simple reference example that confirms the consistency between the analytical results, the theoretical probability limits, and the numerical and Monte Carlo validations.

Case 2: Adding uncertainty to the vehicle position

In this second case, the vehicle initial position has lateral uncertainty, which induces correlation between the collision events. If the vehicle's standard deviation σ_{Y_v} is set to zero, this case naturally reduces to Case 1.

A larger number of examples are considered to illustrate how increasing vehicle uncertainty affects the correlation between events. Three configurations are proposed: (i) the vehicle's uncertainty is much smaller than the pedestrians', (ii) uncertainties of vehicle and pedestrians are comparable, and (iii) the vehicle's uncertainty exceeds that of the pedestrians.

These cases represents realistic scenarios: in the first case, the primary represents a well-known and controlled object relative to uncertain secondary objects, such as orbital debris; in the second case, both primary and secondary objects are well characterized, simulating conjunctions between active satellites; finally, a highly uncertain primary may occur when studying small satellites with sensor anomalies against well-identified secondary objects.

Another key parameter when computing joint probabilities is the initial configuration of the objects, which determines the average distances at the time of collision evaluation.

Two representative geometries are considered: The situation a, where each pedestrian is positioned on the same side of the vehicle, at similar relative distances. In this case, as the vehicle's uncertainty grows, any movement that brings it closer to one pedestrian also tends to bring it closer to the other, increasing the probability of multiple collisions. Consequently, the probability of at least one collision moves away from its upper bound (given by the sum of individual probabilities), and the simplified analytical approximation $P(A_1 \cup A_2) \approx P(A_1) + P(A_2)$ loses accuracy. And the situation b: where pedestrians are located on different sides of the vehicle or at highly different distances. Here, increasing vehicle uncertainty reduces configurations where it can approach both pedestrians simultaneously, lowering the chance of multiple collisions. The simplified formula's error is smaller in this case.

The geometrical parameters of both situations are represented in Table 3.4, and the covariances of each configuration are shown in Table 3.5. The combination of these variants gives six possible experiments to develop.

Table 3.4: Geometrical parameters: initial states, vehicle width and TCA state for all configurations.

Category	**Parameter [units]**	**Value**	
		Conf. a	**Conf.** b
Initial state	Vehicle $\mathbf{r}$ [m]; $\mathbf{v}$ [m/s]	[0, 0];[0, 10]	[0, 0];[0, 10]
	Ped. 1 $\mathbf{r}$ [m]; $\mathbf{v}$ [m/s]	[-10, 100];[1.202, 0]	[-10, 100];[1.202, 0]
	Ped. 2 $\mathbf{r}$ [m]; $\mathbf{v}$ [m/s]	[10, 200];[-0.380, 0]	[10, 200];[-0.620, 0]
Geometry	Vehicle width [m]	2	2
TCA state	Event 1 TCA [s]; $\boldsymbol{\mu}_Z$ [m]	10.0;[2.02, 0]	10.0;[2.02, 0]
	Event 2 TCA [s]; $\boldsymbol{\mu}_Z$ [m]	20.0;[2.40, 0]	20.0;[-2.40, 0]

Table 3.5: Standard deviations of initial states and TCA for all configurations.

Category	**Parameter [units]**	**Value**		
		Conf. i	**Conf.** ii	**Conf.** iii
Initial state	Vehicle σ_x [m]	0.05	0.50	1.20
	Pedestrian 1 σ_x [m]	0.45	0.45	0.45
	Pedestrian 2 σ_x [m]	0.60	0.60	0.60
TCA state	Event 1 σ_x [m]	0.45	0.67	1.28
	Event 2 σ_x [m]	0.60	0.78	1.34

Table 3.6 summarizes the analytical, Monte Carlo, and simplified results for the three experiments of the situation a, with increasing vehicle uncertainty.

Table 3.6: Comparison between analytical, Monte Carlo, and simplified results.

Conf.	Probability quantities	Analytical results [-]	Monte-Carlo results [-]	Simplified formulas [-]	Relative error [%]
$a.i$	$\mathrm{P}(A_1)$	0.0121	0.0121	-	-
	$\mathrm{P}(A_2)$	0.0100	0.0100	-	-
	$\mathrm{P}(A_1 \cap A_2)$	0.0001	0.0001	0.0001	6.11e-02
	$\mathrm{P}(A_1 \cup A_2)$	0.0220	0.0220	0.0220	3.59e-04
$a.ii$	$\mathrm{P}(A_1)$	0.0647	0.0647	-	-
	$\mathrm{P}(A_2)$	0.0365	0.0365	-	-
	$\mathrm{P}(A_1 \cap A_2)$	0.0109	0.0108	0.0024	7.83e-01
	$\mathrm{P}(A_1 \cup A_2)$	0.0904	0.0903	0.0989	9.42e-02
$a.iii$	$\mathrm{P}(A_1)$	0.2038	0.2037	-	-
	$\mathrm{P}(A_2)$	0.1427	0.1426	-	-
	$\mathrm{P}(A_1 \cap A_2)$	0.1039	0.1039	0.0291	7.20e-01
	$\mathrm{P}(A_1 \cup A_2)$	0.2426	0.2424	0.3175	3.08e-01

From the results in Table 3.6, a slight discrepancy can be observed between the simplified and analytical values, both supported by the Monte Carlo simulations. These variations become more significant as the primary's uncertainty increases, confirming that the independence assumption progressively loses validity.

Moreover, the analytical bounds for the probability of the union are always respected. As the primary's uncertainty increases, the actual value approaches the lower bound, while when the primary's uncertainty is small, the value lies practically at the upper bound, as expected (see Figure 3.2).

To illustrate situation b, the results of the first experiment have been re-evaluated with a different initial configuration, shown in Table 3.4 and maintaining the three uncertainty configurations from Table 3.5.

The numerical results of these new experiments developed are shown in Table 3.7.

This results shows a better performance of the simplified formula to approximate the total probability of collision. See Figure 3.3

To illustrate both situations, the Figures 3.4,3.5 and 3.6 depict all the Monte Carlo experiments and the relative position between the vehicle and each pedestrian in their respective TCA.

In the Monte Carlo results, situation a corresponds to events distributed along the diagonal. As correlation increases, these events become more aligned with the diagonal,

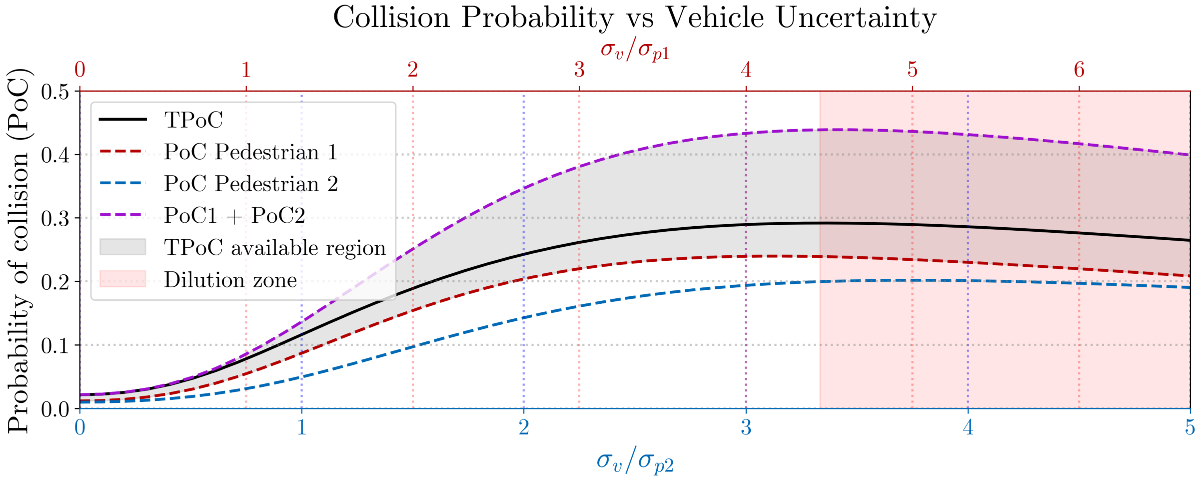

Figure 3.2: Cases a, total probability bounded for al the uncertainty relations tested.

Table 3.7: Comparison between analytical, Monte Carlo, and simplified results.

Conf.	Probability quantities	Analytical results [-]	Monte-Carlo results [-]	Simplified formulas [-]	Relative error [%]
b.i	$\mathrm{P}(A_1)$	0.0121	0.0121	-	-
	$\mathrm{P}(A_2)$	0.0100	0.0100	-	-
	$\mathrm{P}(A_1 \cap A_2)$	0.0001	0.0001	0.0001	6.61e-02
	$\mathrm{P}(A_1 \cup A_2)$	0.0221	0.0220	0.0220	3.42e-04
b.ii	$\mathrm{P}(A_1)$	0.0647	0.0648	-	-
	$\mathrm{P}(A_2)$	0.0365	0.0366	-	-
	$\mathrm{P}(A_1 \cap A_2)$	0.0001	0.0001	0.0024	3.02e+01
	$\mathrm{P}(A_1 \cup A_2)$	0.1012	0.1013	0.0989	2.26e-02
b.iii	$\mathrm{P}(A_1)$	0.2038	0.2038	-	-
	$\mathrm{P}(A_2)$	0.1427	0.1427	-	-
	$\mathrm{P}(A_1 \cap A_2)$	0.0000	0.0000	0.0291	7.39e+02
	$\mathrm{P}(A_1 \cup A_2)$	0.3465	0.3465	0.3175	8.38e-02

indicating a higher occurrence of simultaneous collisions. Extending this reasoning to real-world scenarios, multiple collision probabilities tend to increase when the configurations of primary and secondary objects in the B-plane of each conjunction are similar, as this geometric alignment increases multiple collisions.

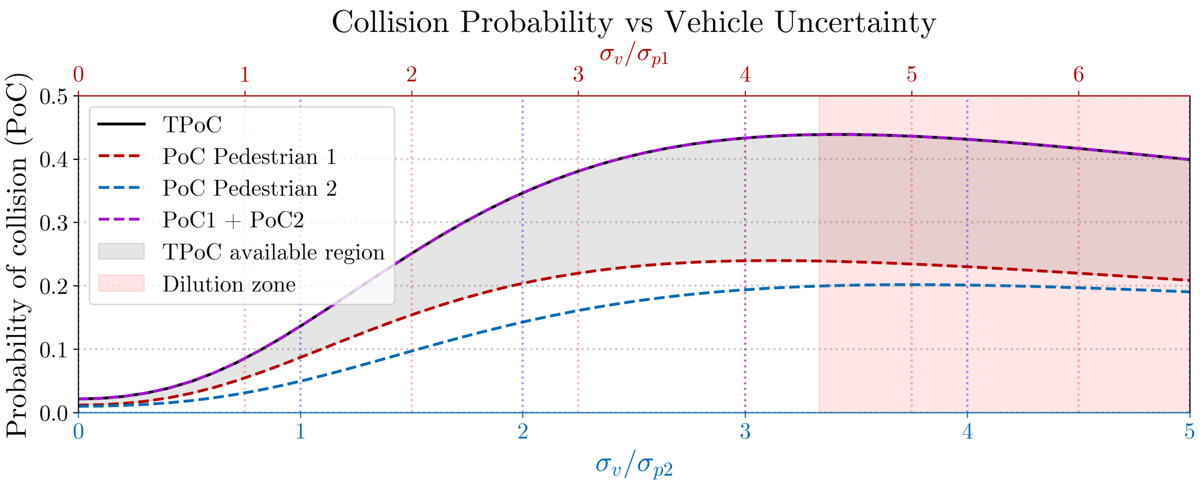

Figure 3.3: Cases b, total probability bounded for al the uncertainty relations tested.

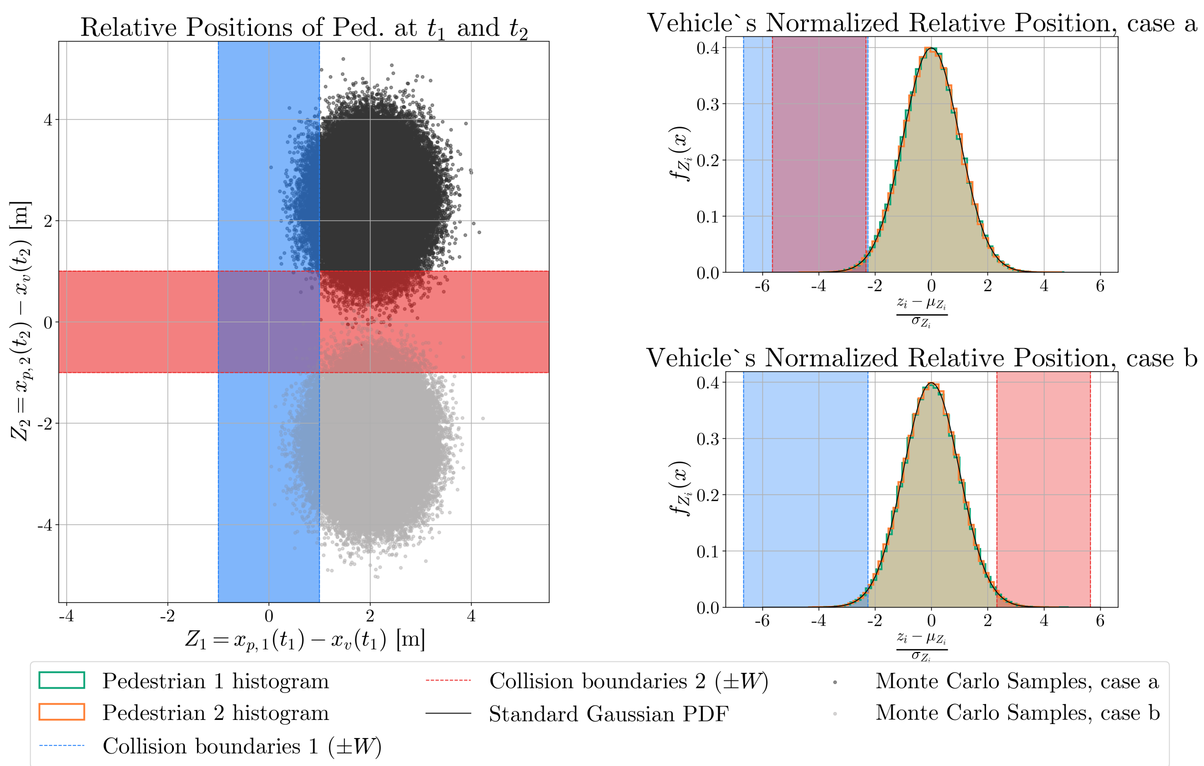

Figure 3.4: Monte Carlo validation for Case 2. For the first cases $a.i$ and $b.i$, where the uncertainty of the vehicle is much lower than the pedestrian ones.

Case 3: Single pedestrian crossing twice

In this third scenario, since the same pedestrian is involved in both events, the correlation between them is complete, representing a limit case of the previous scenario ($\rho_{Z_1 Z_2} = 1$). As a result, all Monte Carlo simulation samples converge along a diagonal, reflecting

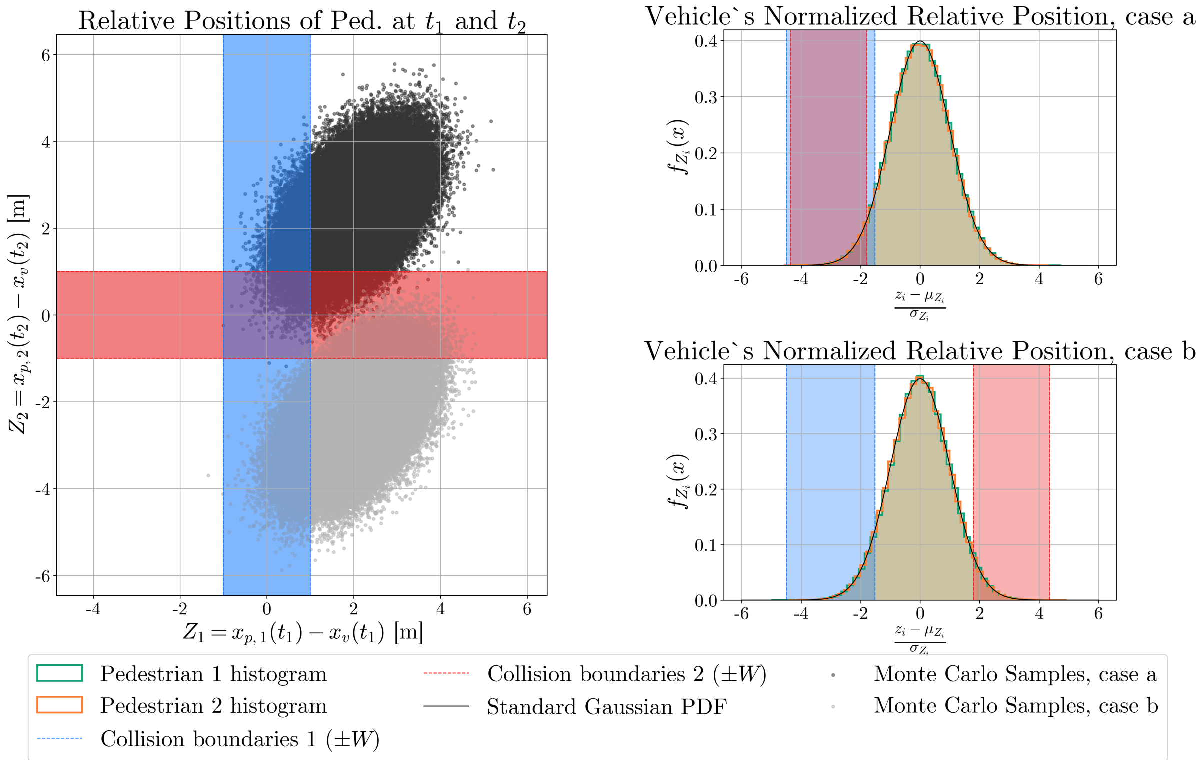

Figure 3.5: Monte Carlo validation for Case 2. For the first cases *a.ii* and *b.ii*, where the uncertainty of the vehicle is on the same order of the pedestrian ones.

the deterministic correlation between the relative positions at t_1 and t_2. This means that knowing the pedestrian's deviation in the first event completely determines their deviation in the second.

Consequently, as shown in the previous case, the main factor driving the total risk is the geometrical relative position of the pedestrian in each event. The level of overlap between the collision domains of the two events becomes critical:

- If the pedestrian is expected to be on the same side of the vehicle in both events (i.e., the mean relative positions μ_{Z_1} and μ_{Z_2} have the same sign and similar magnitudes relative to σ), the events are highly coupled. A pedestrian that causes a collision at t_1 is likely to cause a collision at t_2.
- Conversely, if the relative positions are very different (e.g., on opposite sides of the vehicle), the subset of samples causing a collision in the first event is disjoint from those causing a collision in the second.

Two simulations illustrating this behaviour will be developed using the data from Tables 3.8 and 3.9.

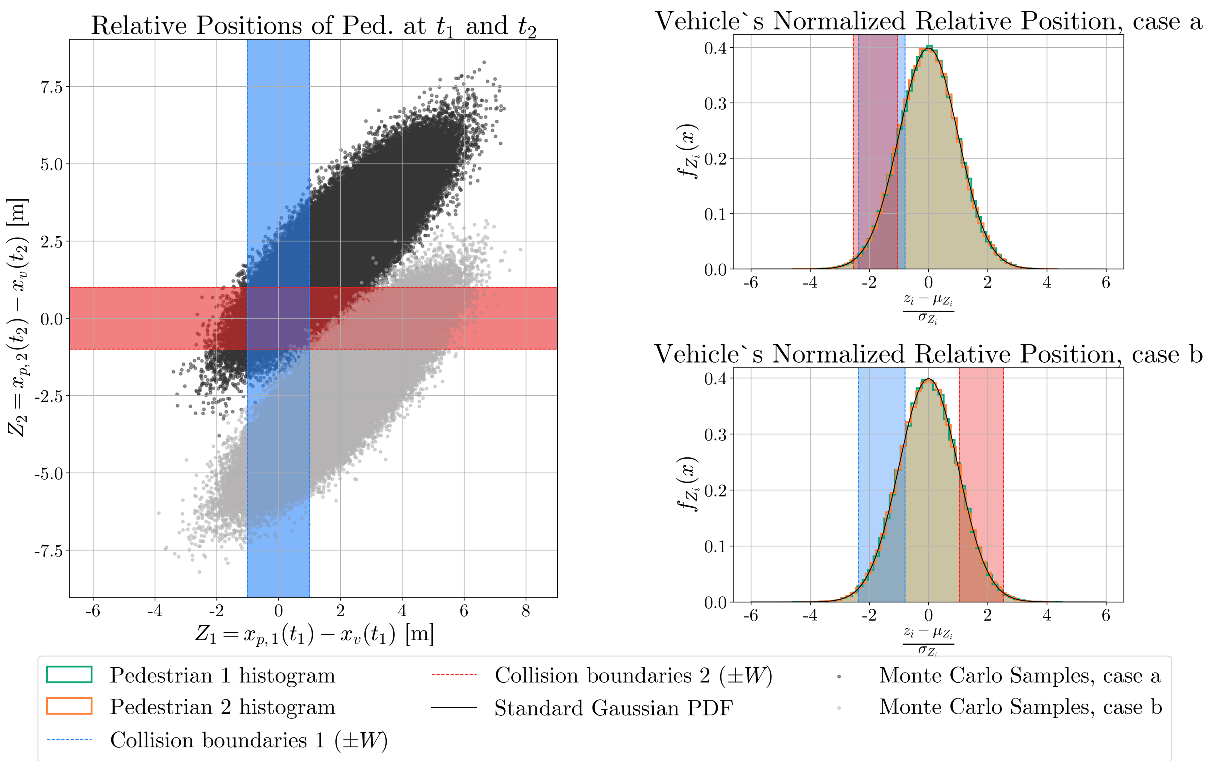

Figure 3.6: Monte Carlo validation for Case 2. For the first cases *a.iii* and *b.iii*, where the uncertainty of the vehicle is much higher than the pedestrian ones.

Table 3.8: Geometrical parameters: initial states, vehicle width and TCA state for all configurations.

Category	Parameter [units]	Value Conf. a	Value Conf. b
Initial state	Vehicle $\mathbf{r}$ [m]; $\mathbf{v}$ [m/s] Ped. $\mathbf{r}$ [m]; $\mathbf{v}$ [m/s]	[0, 0]; [0, 10] [-5, 100]; [0.820, 0]	[0, 0]; [0, 10] [-2, 100]; [0.550, 0]
Geometry	Vehicle width [m] Path segment 1: $\mathbf{x}_\mathrm{i}; \mathbf{x}_\mathrm{f}$ [m] Path segment 2: $\mathbf{x}_\mathrm{i}; \mathbf{x}_\mathrm{f}$ [m] Path segment 3: $\mathbf{x}_\mathrm{i}; \mathbf{x}_\mathrm{f}$ [m]	2 [0, 0]; [0, 210] [0, 210]; [20, 210] [20, 210]; [20, 0]	2 [0, 0]; [0, 210] [0, 210]; [20, 210] [20, 210]; [20, 0]
TCA state	Event 1 TCA [s]; $\boldsymbol{\mu}_Z$ [m] Event 2 TCA [s]; $\boldsymbol{\mu}_Z$ [m]	10.0;[3.20, 0] 34.0;[2.88, 0]	10.0;[3.50, 0] 34.0;[-3.30, 0]

The results for these data are shown in Table 3.10. The analysis of these results highlights the dangers of ignoring correlation in multi-event scenarios.

In Configuration a, the pedestrian is positioned on the same side of the vehicle for both encounters. Due to the perfect positive correlation, a trajectory deviation leading to a collision in the first event propagates to the second, creating a "nested" scenario ($A_1 \subset$

Table 3.9: Standard deviations of initial states and TCA state.

Category	Parameter [units]	Value
Initial state	Vehicle σ_x [m]	0.00
	Pedestrian 1 σ_x [m]	1.00
	Pedestrian 2 σ_x [m]	1.00
TCA state	Event 1 σ_x [m]	1.00
	Event 2 σ_x [m]	1.00

Table 3.10: Comparison between analytical, Monte Carlo, and simplified results.

Conf.	Probability quantities	Analytical results [-]	Monte-Carlo results [-]	Simplified formulas [-]	Relative error [%]
a	P(A_1)	0.0139	0.0138	-	-
	P(A_2)	0.0300	0.0299	-	-
	P($A_1 \cap A_2$)	0.0139	0.0138	0.0004	9.70e-01
	P($A_1 \cup A_2$)	0.0300	0.0300	0.0435	4.47e-01
b	P(A_1)	0.0062	0.0062	-	-
	P(A_2)	0.0107	0.0106	-	-
	P($A_1 \cap A_2$)	0.0000	0.0000	0.0001	-
	P($A_1 \cup A_2$)	0.0169	0.0168	0.0169	3.93e-03

A_2). The simplified formula, by assuming independence, fails to account for this overlap. It treats the intersection as negligible, resulting in a significant overestimation of the total accumulated risk.

In contrast, Configuration b places the pedestrian on opposite sides of the vehicle across the two events. Given the positive correlation, a deviation towards the vehicle in one instance corresponds to a deviation away from it in the other, rendering the collision events mutually exclusive ($P(A_1 \cap A_2) \approx 0$). In this specific geometry, the simplified formula yields an accurate result: the product of individual probabilities is naturally negligible.

In Figure 3.7 are shown the Monte Carlo results to illustrate the results.

Case 4: Deterministic vehicle, correlated pedestrians

In this final scenario, the vehicle follows the same deterministic trajectory as in Case 2.1.3, while the initial lateral positions of the two pedestrians are statistically correlated. A positive correlation implies that both pedestrians are perturbed in the same direction, while a negative correlation implies they are affected in opposite directions.

The correlation coefficient $\rho_{Z_1 Z_2}$ is imposed arbitrarily in this study, acting as a parametric

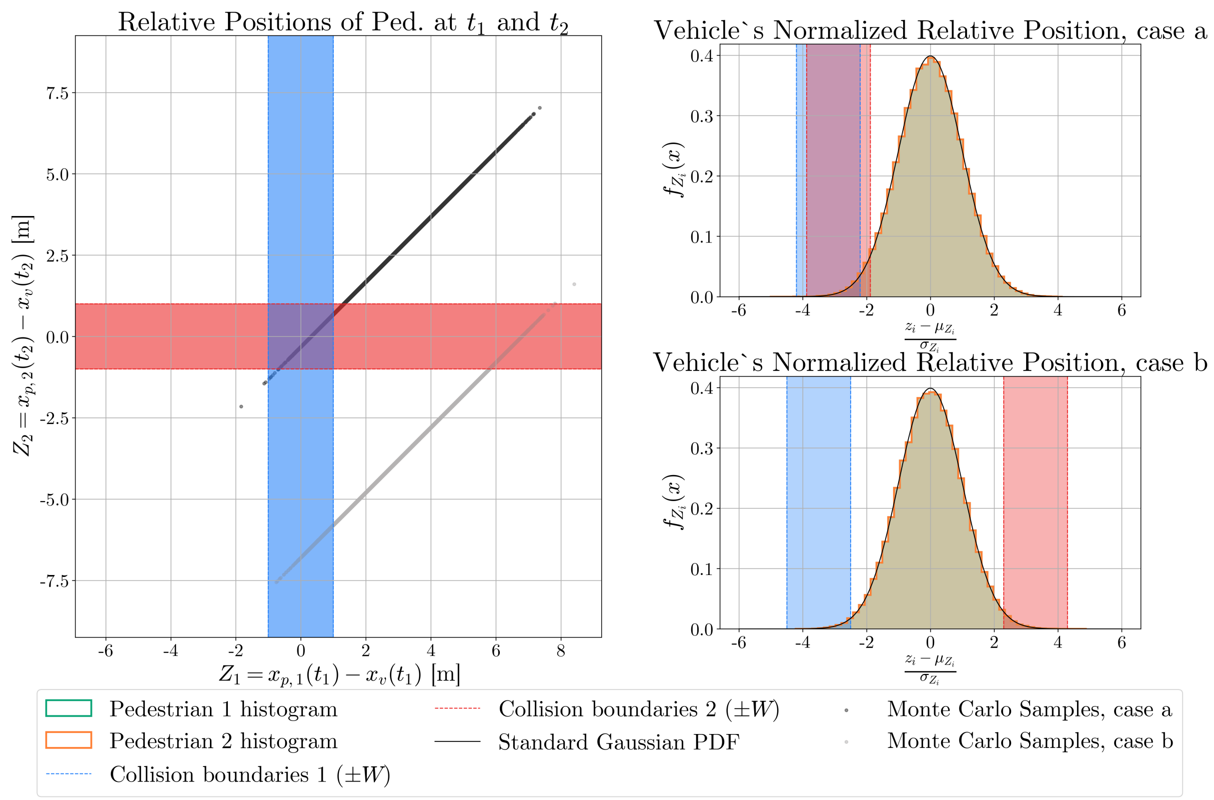

Figure 3.7: Monte Carlo validation for Case 3.

variable to analyse its impact on the total probability of collision.

Following the experimental structure established in Case 3.1.1, two distinct geometric configurations are considered:

- **Configuration** a: The relative positions of the pedestrians with respect to the vehicle at the Time of Closest Approach (TCA) are similar (same side of the vehicle).
- **Configuration** b: The relative positions are opposite (different sides of the vehicle).

The parameter sweep focuses on the Pearson correlation coefficient $\rho_{Z_1 Z_2}$, ranging from strong positive to strong negative values. The complete set of geometrical and statistical parameters required to replicate these simulations is provided in Tables 3.11 and 3.12.

Tables 3.13 and 3.14 present the results obtained both analytically and via Monte Carlo simulation, using the sample size derived from Eq. (**??**). The close agreement between the Monte Carlo results and the analytical values verifies the validity of the derivation. The "Simplified formulas" column, is provided for comparison.

The results for Configuration a (Table 3.13), where both pedestrians are located on the same side of the vehicle, show a clear dependency on the sign of the correlation. A strong

Table 3.11: Geometrical parameters: initial states, vehicle width and TCA state for all configurations.

Category	Parameter [units]	Value	
		Conf. a	Conf. b
Initial state	Vehicle $\mathbf{r}$ [m]; $\mathbf{v}$ [m/s]	[0, 0];[0, 10]	[0, 0];[0, 10]
	Ped. 1 $\mathbf{r}$ [m]; $\mathbf{v}$ [m/s]	[-10, 100];[1.200, 0]	[-10, 100];[1.200, 0]
	Ped. 2 $\mathbf{r}$ [m]; $\mathbf{v}$ [m/s]	[10, 200];[-0.385, 0]	[10, 200];[-0.615, 0]
Geometry	Vehicle width [m]	2	2
TCA state	Event 1 TCA [s]; $\boldsymbol{\mu}_Z$ [m]	10.0;[2.00, 0]	10.0;[2.00, 0]
	Event 2 TCA [s]; $\boldsymbol{\mu}_Z$ [m]	20.0;[2.30, 0]	20.0;[-2.30, 0]

Table 3.12: Standard deviations of initial states and TCA for all configurations.

Category	Parameter [units]	Value			
		Conf. i	Conf. ii	Conf. iii	Conf. iv
Initial state	Vehicle σ_x [m]	0.00	0.00	0.00	0.00
	Pedestrian 1 σ_x [m]	0.45	0.45	0.45	0.45
	Pedestrian 2 σ_x [m]	0.60	0.60	0.60	0.60
	$\rho_{Z_1 Z_2}$ [-]	0.70	0.30	-0.30	-0.70
TCA state	Event 1 σ_x [m]	0.45	0.45	0.45	0.45
	Event 2 σ_x [m]	0.60	0.60	0.60	0.60

Table 3.13: Comparison between analytical, Monte Carlo, and simplified results (Configuration a).

Conf.	Probability quantities	Analytical results [-]	Monte-Carlo results [-]	Simplified formulas [-]	Relative error [%]
$a.i$	$\mathrm{P}(A_1)$	0.0131	0.0132	-	-
	$\mathrm{P}(A_2)$	0.0151	0.0152	-	-
	$\mathrm{P}(A_1 \cap A_2)$	0.0041	0.0041	0.0002	9.51e-01
	$\mathrm{P}(A_1 \cup A_2)$	0.0242	0.0243	0.0281	1.60e-01
$a.ii$	$\mathrm{P}(A_1)$	0.0131	0.0131	-	-
	$\mathrm{P}(A_2)$	0.0151	0.0152	-	-
	$\mathrm{P}(A_1 \cap A_2)$	0.0010	0.0009	0.0002	7.92e-01
	$\mathrm{P}(A_1 \cup A_2)$	0.0273	0.0273	0.0281	2.78e-02
$a.iii$	$\mathrm{P}(A_1)$	0.0131	0.0130	-	-
	$\mathrm{P}(A_2)$	0.0151	0.0152	-	-
	$\mathrm{P}(A_1 \cap A_2)$	0.0000	0.0000	0.0002	1.30e+01
	$\mathrm{P}(A_1 \cup A_2)$	0.0283	0.0282	0.0281	6.53e-03
$a.iv$	$\mathrm{P}(A_1)$	0.0131	0.0132	-	-
	$\mathrm{P}(A_2)$	0.0151	0.0152	-	-
	$\mathrm{P}(A_1 \cap A_2)$	0.0000	0.0000	0.0002	4.89e+05
	$\mathrm{P}(A_1 \cup A_2)$	0.0283	0.0284	0.0281	7.03e-03

positive correlation ($\rho = 0.7$, Case *a.i*) implies that a deviation causing a collision in the first event likely causes one in the second. This increases the intersection probability $P(A_1 \cap A_2)$, reducing the total accumulated risk $P(A_1 \cup A_2)$ compared to the independent case. Conversely, a negative correlation ($\rho = -0.7$, Case *a.iv*) decouples the events: a deviation towards the vehicle in one event implies a deviation away from it in the other. This makes the events mutually exclusive ($P(A_1 \cap A_2) \to 0$), giving a total probability near to the upper bound (sum of individual probabilities).

This continuous evolution is depicted in Figure 3.8. The total collision probability approaches the upper bound (simple summation) for negative correlations and descends towards the lower bound (maximum of individuals) as ρ approaches 1.

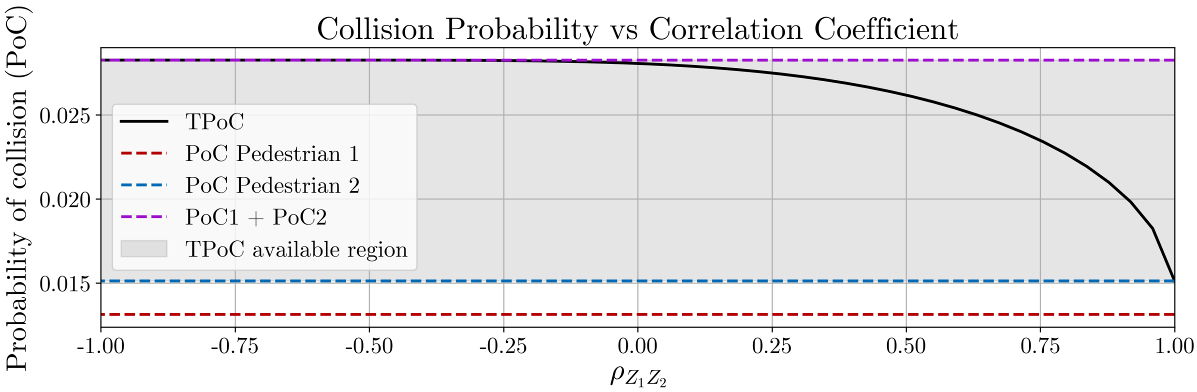

Figure 3.8: Evolution of total probability as a function of correlation ρ for Configuration a.

The results for Configuration b (Table 3.14) exhibit the exact opposite behaviour. Here, the pedestrians are on opposite sides of the vehicle. A positive correlation ($\rho > 0$) now reduces the intersection probability to near zero (Case *b.i*), because a shift that causes a collision in one event moves the other pedestrian away from danger. Conversely, a negative correlation ($\rho < 0$) has the opposite behaviour: a shift towards the vehicle in one event is generates a shift towards the vehicle in the other, significantly increasing $P(A_1 \cap A_2)$ (Case *b.iv*) and reducing the total risk.

Figure 3.9 illustrates this inverted trend, confirming that the impact of correlation is determined by the relative geometry of the encounters.

Finally, Figures 3.10 through 3.13 provide a validation of the Monte Carlo sampling process. These scatter plots of the sampled pairs (Z_1, Z_2) clearly show how the ellipse of the joint distribution rotates and deforms as the correlation coefficient varies from positive to negative, matching the theoretical bivariate Gaussian behaviour.

Table 3.14: Comparison between analytical, Monte Carlo, and simplified results (Configuration b).

Conf.	Probability quantities	Analytical results [-]	Monte-Carlo results [-]	Simplified formulas [-]	Relative error [%]
b.i	$P(A_1)$	0.0131	0.0132	-	-
	$P(A_2)$	0.0151	0.0151	-	-
	$P(A_1 \cap A_2)$	0.0000	0.0000	0.0002	4.89e+05
	$P(A_1 \cup A_2)$	0.0283	0.0283	0.0281	7.03e-03
b.ii	$P(A_1)$	0.0131	0.0131	-	-
	$P(A_2)$	0.0151	0.0151	-	-
	$P(A_1 \cap A_2)$	0.0000	0.0000	0.0002	1.30e+01
	$P(A_1 \cup A_2)$	0.0283	0.0281	0.0281	6.53e-03
b.iii	$P(A_1)$	0.0131	0.0128	-	-
	$P(A_2)$	0.0151	0.0150	-	-
	$P(A_1 \cap A_2)$	0.0010	0.0010	0.0002	7.92e-01
	$P(A_1 \cup A_2)$	0.0273	0.0269	0.0281	2.78e-02
b.iv	$P(A_1)$	0.0131	0.0132	-	-
	$P(A_2)$	0.0151	0.0153	-	-
	$P(A_1 \cap A_2)$	0.0041	0.0041	0.0002	9.51e-01
	$P(A_1 \cup A_2)$	0.0242	0.0244	0.0281	1.60e-01

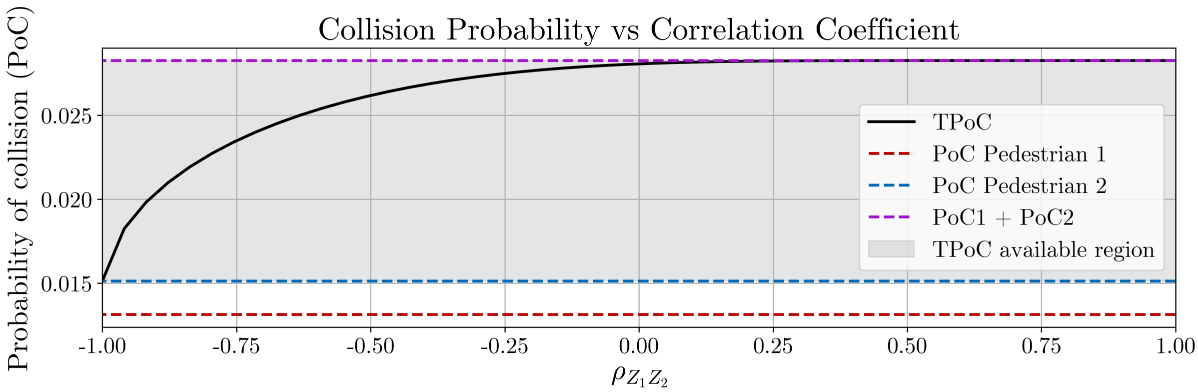

Figure 3.9: Evolution of total probability as a function of correlation ρ for Configuration b (opposite-side geometry).

Case 5: Adding wind to the scenario

This final case integrates all the previously studied effects to simulate the most realistic operational scenario in LEO: the combination of initial state uncertainty (Vehicle) and dynamic environmental model with uncertainty (Wind/Drag).

The setup introduces a common wind field modeled as a random variable W, which perturbs the trajectories of all objects. The susceptibility of each object to this wind is defined by sensitivity coefficients α. The total correlation between the events has now

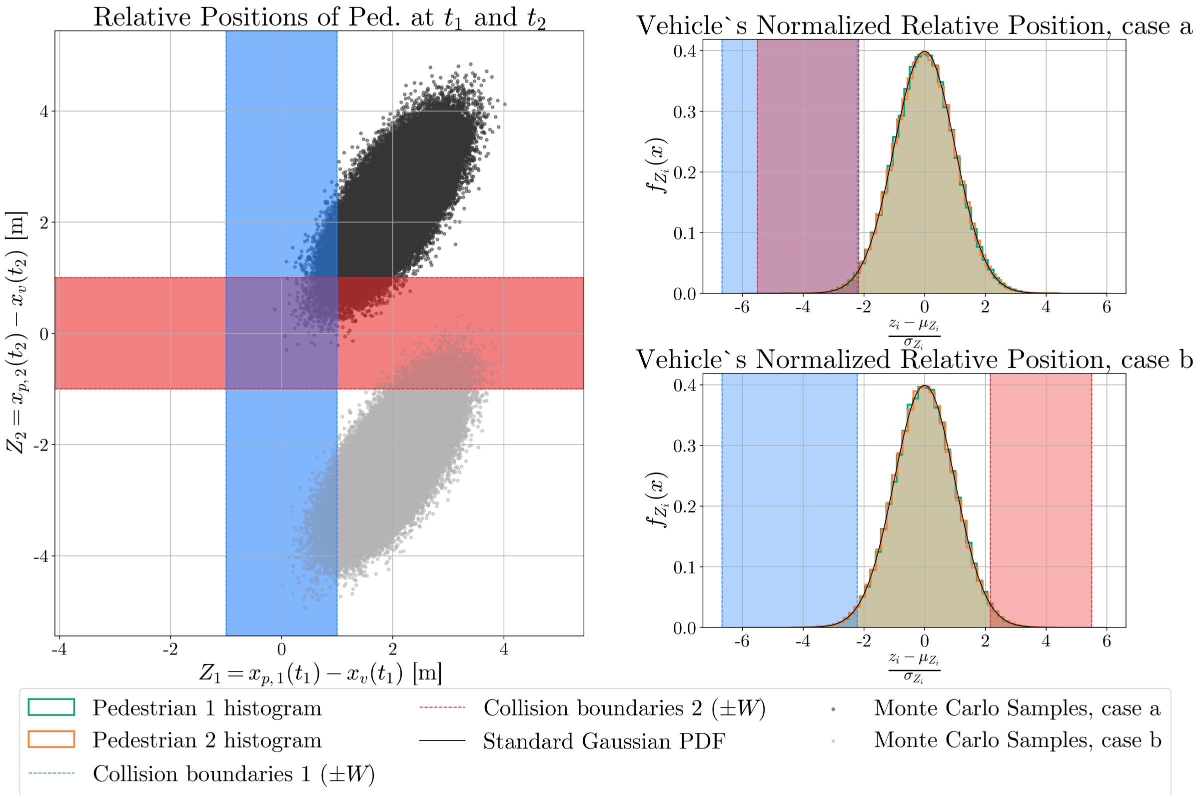

Figure 3.10: Monte Carlo scatter plot for $\rho = 0.7$. The distribution is elongated along the main diagonal, indicating strong positive correlation.

two sources:

1. **Vehicle Uncertainty (σ_{X_v}):** Induces a positive correlation (a shift in the vehicle affects both events identically).
2. **Wind Uncertainty (σ_W):** Can produce positive or negative correlation depending on the sensitivity between the vehicle and the pedestrians ($\alpha_{p,i} - \alpha_v$).

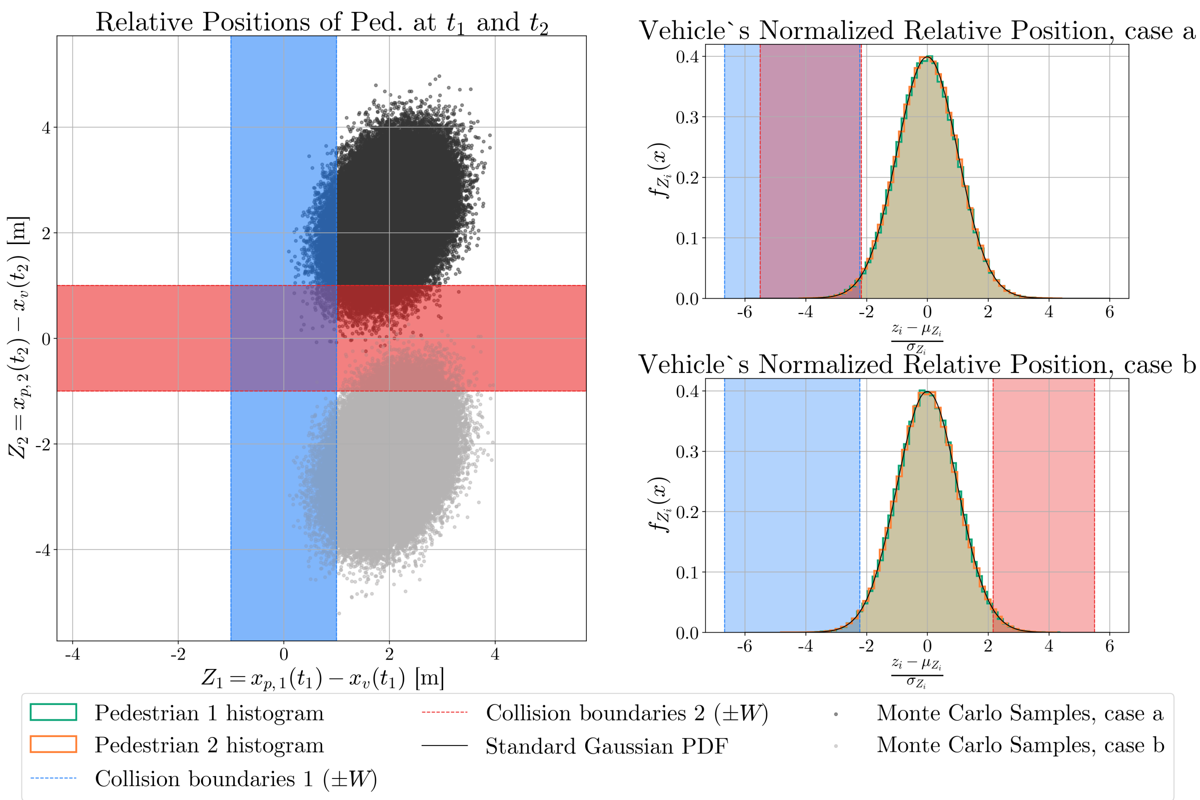

Figure 3.11: Monte Carlo scatter plot for $\rho = 0.3$. The correlation is weaker, resulting in a more circular dispersion.

To study this interaction, the wind uncertainty is kept constant ($\sigma_W = 0.10$ m/s), while the vehicle's initial position uncertainty σ_{X_v} is varied across three configurations (i, ii, iii) to observe the transition from a wind-dominated regime to a vehicle-dominated regime.

Tables 3.15 and 3.16 detail the parameters used. Note that the sencibility factors $[\alpha_v, \alpha_1, \alpha_2] = [1.0, 1.3, 0.8]$ imply that Pedestrian 1 is more sensitive to wind than the vehicle, while Pedestrian 2 is less sensitive.

Tables 3.17 and 3.18 present the probability results. As in previous cases, Configuration a places pedestrians on the same side of the vehicle, while Configuration b places them on opposite sides.

The results in Tables 3.17 and 3.18 reveal the shifting nature of the correlation.

In Configuration i (Wind Dominance, $\sigma_{X_v} \approx 0$), the wind is the primary common uncertainty source. In Case $b.i$, this results in a notable intersection probability $P(A_1 \cap A_2) \approx 0.0029$, which the simplified formula underestimates.

In Configuration iii (Vehicle Dominance, $\sigma_{X_v} = 1.20$), the vehicle's position uncertainty

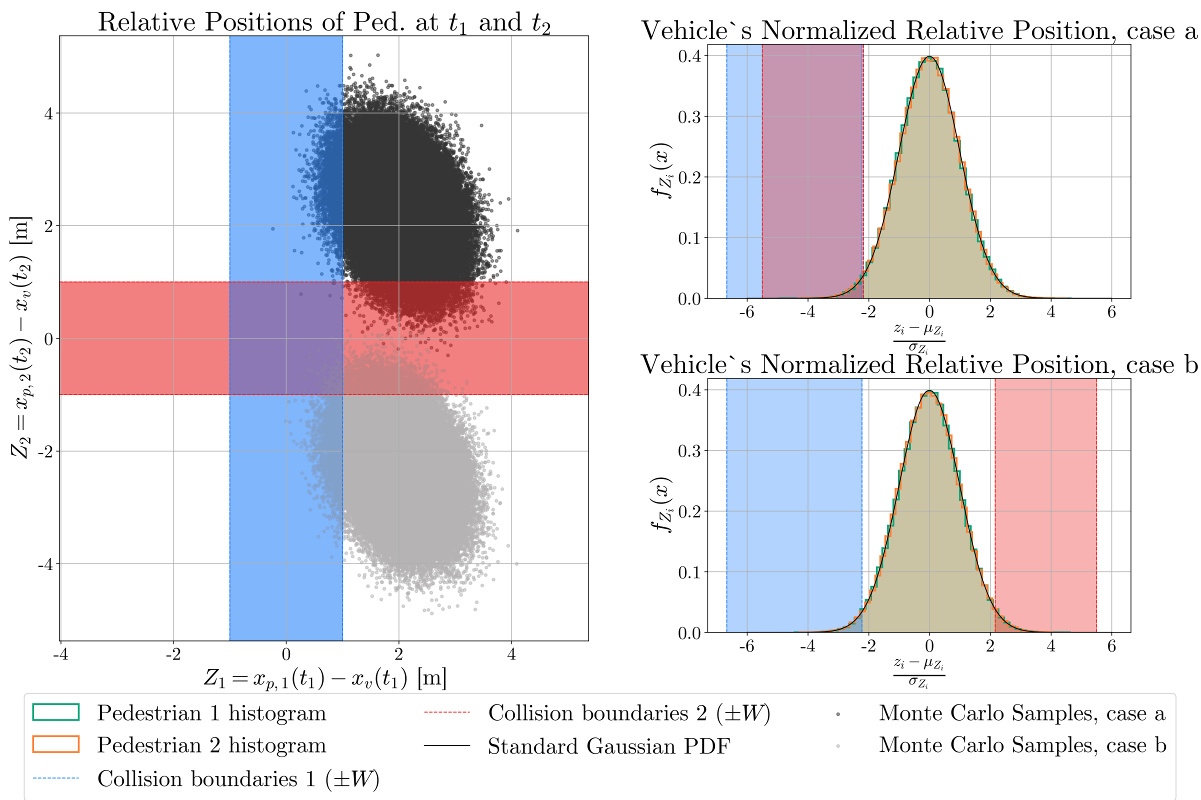

Figure 3.12: Monte Carlo scatter plot for $\rho = -0.3$. The distribution begins to align with the anti-diagonal.

Table 3.15: Geometrical parameters: initial states, vehicle width and TCA state for all configurations.

Category	Parameter [units]	Value	
		Conf. a	Conf. b
Initial state	Vehicle **r** [m]; **v** [m/s] Ped. 1 **r** [m]; **v** [m/s] Ped. 2 **r** [m]; **v** [m/s]	[0, 0];[0, 10] [-10, 100];[1.202, 0] [10, 200];[-0.380, 0]	[0, 0];[0, 10] [-10, 100];[1.202, 0] [10, 200];[-0.620, 0]
Geometry	Vehicle width [m]	2.0	2.0
Wind	Wind μ_W [m/s] Sensibility factor $[\alpha_v, \alpha_1, \alpha_2]$ [-]	0.0 [1.0, 1.3, 0.8]	0.0 [1.0, 1.3, 0.8]
TCA state	Event 1 TCA [s]; $\boldsymbol{\mu}_Z$ [m] Event 2 TCA [s]; $\boldsymbol{\mu}_Z$ [m]	10.0;[2.02, 0] 20.0;[2.40, 0]	10.0;[2.02, 0] 20.0;[-2.40, 0]

is the main common effect. The scenario reverts to Case 2: the large common vehicle error σ_{X_v} induces a strong positive correlation. In geometry a (same side), this high positive correlation increases the intersection probability ($P(\cap) \approx 0.090$), meaning the simplified formula overestimates total risk. In geometry b (opposite sides), this same

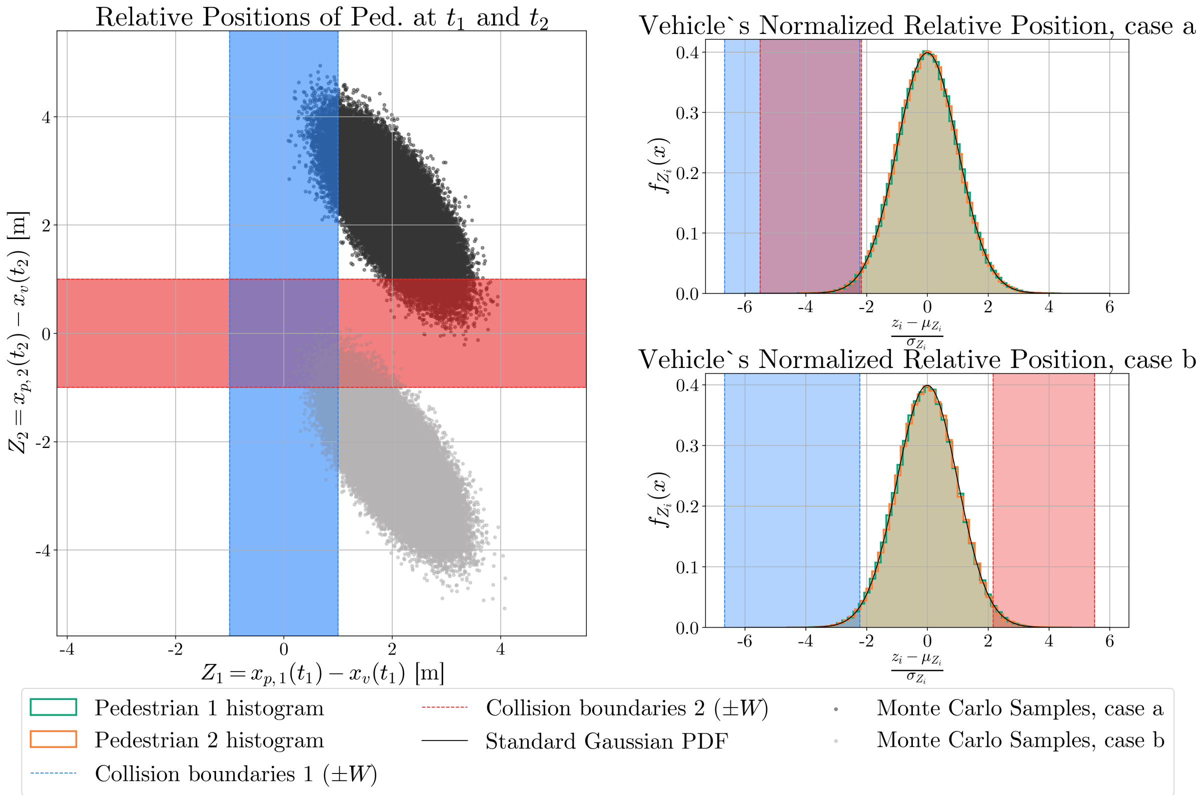

Figure 3.13: Monte Carlo scatter plot for $\rho = -0.7$. Strong negative correlation is evident, with samples aligning along the anti-diagonal.

Table 3.16: Standard deviations of initial states and TCA for all configurations.

Category	Parameter [units]	Value		
		Conf. *i*	Conf. *ii*	Conf. *iii*
Initial state	Vehicle σ_x [m]	0.05	0.50	1.20
	Pedestrian 1 σ_x [m]	0.45	0.45	0.45
	Pedestrian 2 σ_x [m]	0.60	0.60	0.60
	Wind σ_W [m/s]	0.10	0.10	0.10
TCA state	Event 1 σ_x [m]	0.54	0.74	1.32
	Event 2 σ_x [m]	0.72	0.88	1.40

positive correlation makes the events mutually exclusive ($P(\cap) \approx 0.001$), meaning the simplified formula significantly overestimates the intersection (predicting 0.0315).

Figures 3.14, 3.15, and 3.16 visually confirm this transition. In Fig. 3.14 (Wind dominated), the distribution is and shaped by the wind sensitivity. In Fig. 3.16 (Vehicle dominated), the distribution elongates along the main diagonal, characteristic of the positive correlation driven by the vehicle's state error.

Table 3.17: Comparison between analytical, Monte Carlo, and simplified results (Configuration a).

Conf.	Probability quantities	Analytical results [-]	Monte-Carlo results [-]	Simplified formulas [-]	Relative error [%]
$a.i$	$\mathrm{P}(A_1)$	0.0302	0.0300	-	-
	$\mathrm{P}(A_2)$	0.0264	0.0264	-	-
	$\mathrm{P}(A_1 \cap A_2)$	0.0001	0.0001	0.0008	7.23e+00
	$\mathrm{P}(A_1 \cup A_2)$	0.0565	0.0563	0.0558	1.24e-02
$a.ii$	$\mathrm{P}(A_1)$	0.0830	0.0827	-	-
	$\mathrm{P}(A_2)$	0.0553	0.0551	-	-
	$\mathrm{P}(A_1 \cap A_2)$	0.0088	0.0088	0.0046	4.79e-01
	$\mathrm{P}(A_1 \cup A_2)$	0.1295	0.1290	0.1337	3.26e-02
$a.iii$	$\mathrm{P}(A_1)$	0.2083	0.2087	-	-
	$\mathrm{P}(A_2)$	0.1511	0.1515	-	-
	$\mathrm{P}(A_1 \cap A_2)$	0.0898	0.0905	0.0315	6.50e-01
	$\mathrm{P}(A_1 \cup A_2)$	0.2696	0.2697	0.3279	2.16e-01

Table 3.18: Comparison between analytical, Monte Carlo, and simplified results (Configuration b).

Conf.	Probability quantities	Analytical results [-]	Monte-Carlo results [-]	Simplified formulas [-]	Relative error [%]
$b.i$	$\mathrm{P}(A_1)$	0.0302	0.0302	-	-
	$\mathrm{P}(A_2)$	0.0264	0.0264	-	-
	$\mathrm{P}(A_1 \cap A_2)$	0.0029	0.0029	0.0008	7.22e-01
	$\mathrm{P}(A_1 \cup A_2)$	0.0537	0.0537	0.0558	3.85e-02
$b.ii$	$\mathrm{P}(A_1)$	0.0830	0.0832	-	-
	$\mathrm{P}(A_2)$	0.0553	0.0552	-	-
	$\mathrm{P}(A_1 \cap A_2)$	0.0019	0.0019	0.0046	1.43e+00
	$\mathrm{P}(A_1 \cup A_2)$	0.1364	0.1365	0.1337	1.98e-02
$b.iii$	$\mathrm{P}(A_1)$	0.2083	0.2080	-	-
	$\mathrm{P}(A_2)$	0.1511	0.1511	-	-
	$\mathrm{P}(A_1 \cap A_2)$	0.0010	0.0010	0.0315	3.10e+01
	$\mathrm{P}(A_1 \cup A_2)$	0.3584	0.3582	0.3279	8.51e-02

3.1.2. Conclusions from the Toy Problem

The "toy problem" has provided a clear vision of how uncertainties, correlations, and geometrical configurations affect the total probability of collision. Throughout all the cases studied, the analytical bounds for the probability of the union of events are always respected. Monte Carlo simulations corroborate the analytical formulas developed, confirming their validity and accuracy for the simplified models considered.

The geometry of the problem is important in determining the effect of increasing corre-

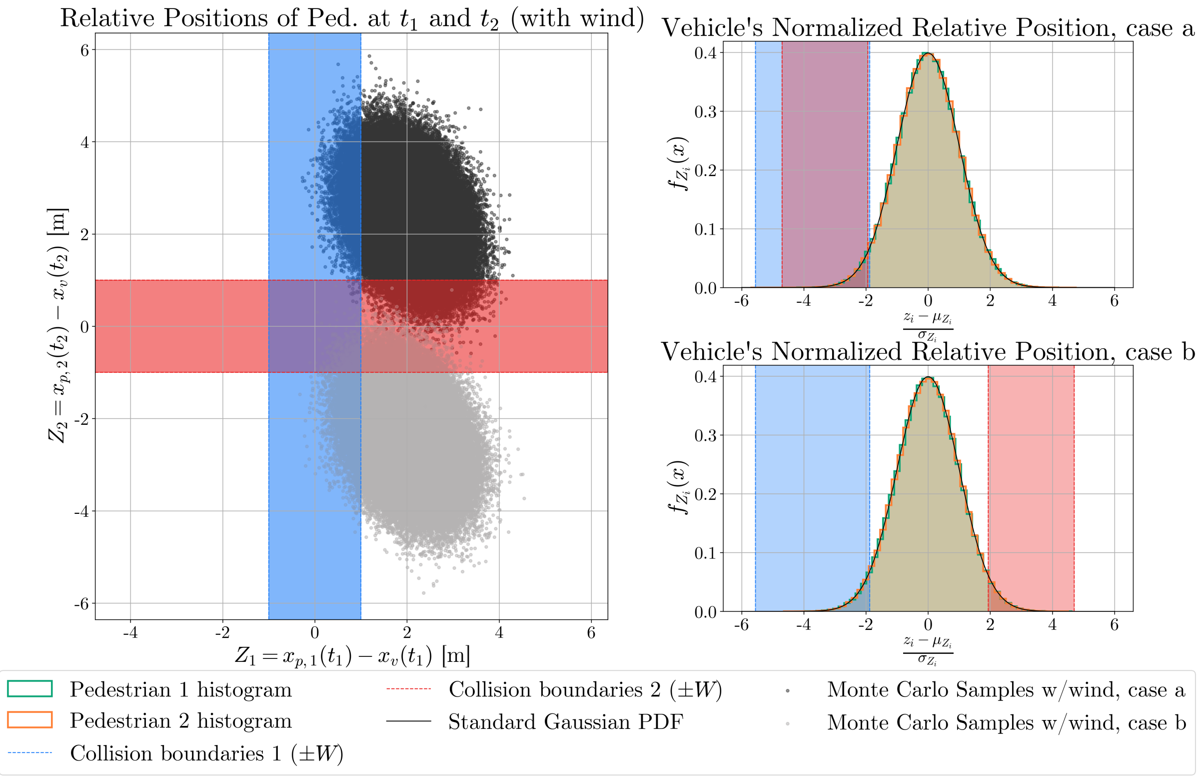

Figure 3.14: Monte Carlo scatter plot for Configuration i (Wind dominated). The correlation structure is subtle and driven by differential drag.

lation on the total probability of collision. When the relative positions of the objects at each TCA are close, a higher positive correlation leads to an increase in the joint probability, and consequently, a reduction of the total collision probability. In contrast, if the configuration presents completely opposite relative positions at the TCA for each event, a high negative correlation has the same effect, reducing the total collision probability. Otherwise, when the configuration reduces the likelihood of simultaneous events, correlation has little effect. This demonstrates that simplified approximations, such as assuming that the total probability is the sum of individual probabilities, can work well in some cases but may result in a significant overestimation of collision probability in others.

It is important to note the limitations of this experiment. The models used for collision verification are very simple and do not fully represent the true computation of conjunctions between satellites in space or TCA. Moreover, fixing the directions of motion of all objects limits the possible geometrical configurations, but in three-dimensional space the number of possible configurations is much larger and correlations between events are more complex to estimate. Despite these limitations, the results provide knowledge that can be extrapolated to more realistic 3D scenarios, which will be implemented in the following

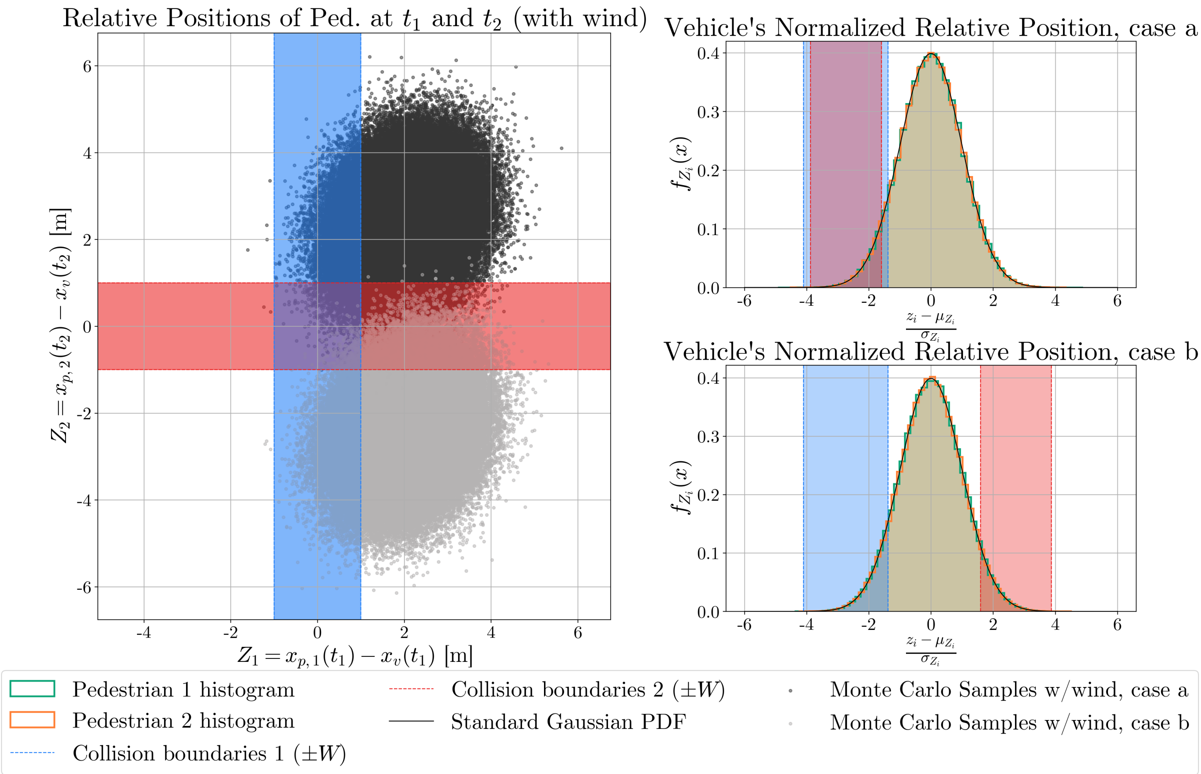

Figure 3.15: Monte Carlo scatter plot for Configuration *ii* (Intermediate). A mix of wind and vehicle effects.

section.

Finally, all cases analysed in this "toy problem" consider only two possible collisions to simplify the formulation and computations. However, the methods and conclusions can be extended to a larger, number of potential collisions, allowing for an extended application of the developed analytical and numerical techniques.

3.2. Orbital 3D Case Results

This section presents the results obtained using the models and formulations derived in Chapter 2. To ensure the proposed method is reliable, the results are first validated against Monte Carlo simulations.

The selection and design of the three-dimensional study cases are driven by the conclusions obtained from the two-dimensional "toy problem". The simplified analysis demonstrated that specific physical configurations govern the statistical correlation between encounters. Consequently, these fundamental behaviours are now translated into realistic orbital scenarios to verify if the same patterns hold true in a complex 3D environment.

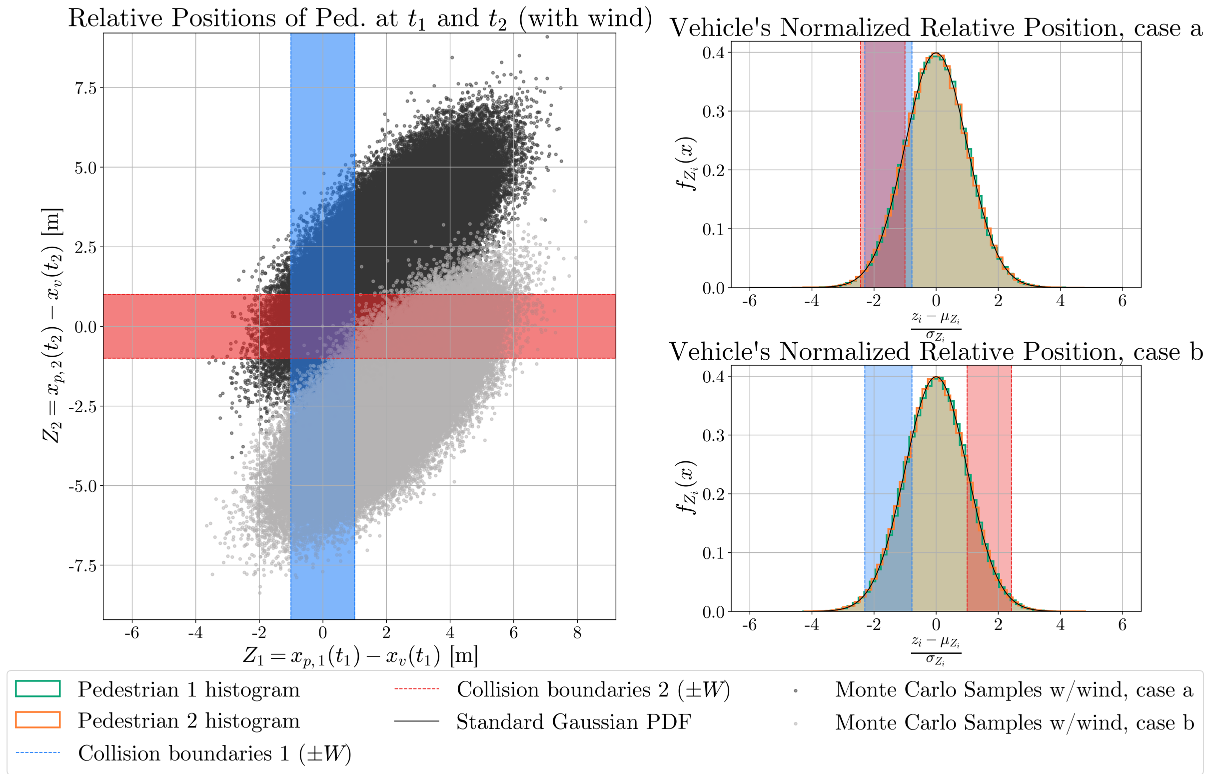

Figure 3.16: Monte Carlo scatter plot for Configuration *iii* (Vehicle dominated). The distribution aligns with the main diagonal, indicating strong positive correlation.

Specifically, the findings from the "toy problem" define the following expectations for the 3D cases:

- **Influence of a common primary object:** Based on the results of the uncertain vehicle in the 2D analysis, it is expected that the correlation in 3D will be governed by the ratio between the primary satellite's covariance and those of the secondary objects. If the primary's uncertainty dominates, a strong statistical coupling should be observed, rendering the independent approximation invalid.

- **Influence of a common secondary object:** Following the repeated pedestrian scenario, encountering the same secondary object is expected to generate extreme correlation values. As seen in the "toy problem", the total collision probability is expected to be highly sensitive to the relative geometry of the encounters and to the deviations introduced by realistic orbital perturbations.

By evaluating these specific configurations, this section aims to prove that the analytical model accurately captures the variance reductions and spatial shifts predicted by the theoretical 2D model. Ultimately, it is expected to confirm that traditional operational approaches, which assume statistical independence, lead to overestimate the actual accumulated collision risk.

The analysis is organized into two main parts:

- **Model Validation:** The methodology is tested using a specific case study with a high collision probability. By comparing the analytical approach to Monte Carlo results, the accuracy and computational efficiency of the model are confirmed.
- **Performance across different configurations:** Following validation, the analytical model is applied to the previously defined orbital scenarios, testing various encounter geometries and uncertainty levels to simulate the situations tested in the "toy problem".

3.2.1. Model Validation

The validation of the proposed methodology is performed through a Monte Carlo (MC) analysis. It has been selected a determined case with a high probability of collision in both events involved, in order to reduce the computational cost while maintaining a good quality result.

The required number of samples to achieve a representative estimate of the PoC is determined through the application of the Dagum estimation formula. A comparative analysis of various sample size estimators is presented in Figure 3.17,illustrating the convergence requirements for different criteria. This approach ensures that the estimated PoC remains within a relative error of less than 10%, considering a 95% confidence interval. Based on this studio, and knowing that the lower PoC estimated will be in the order of 10^{-2}, the number of samples selected has been 100000.

The physical and orbital parameters for the primary satellite and both secondary objects are detailed in Table 3.19, Table 3.20, and Table 3.21. Additionally, the initial uncertainty associated with each object is defined by the covariance matrices provided in Table 3.22.

The statistical results from the Monte Carlo validation are summarized in Table 3.23. This table presents the individual Probability of Collision (PoC) for each conjunction event, the joint probability of collision and the Total Probability of Collision (TPoC) calculated for the multi-event scenario. These numerical values are used in the next comparison with the analytical model.

Following the numerical validation, the analytical results are evaluated. These results are summarized in Table 3.24, which includes the individual PoC for each event, the analytical joint probability and the TPoC for comparison.

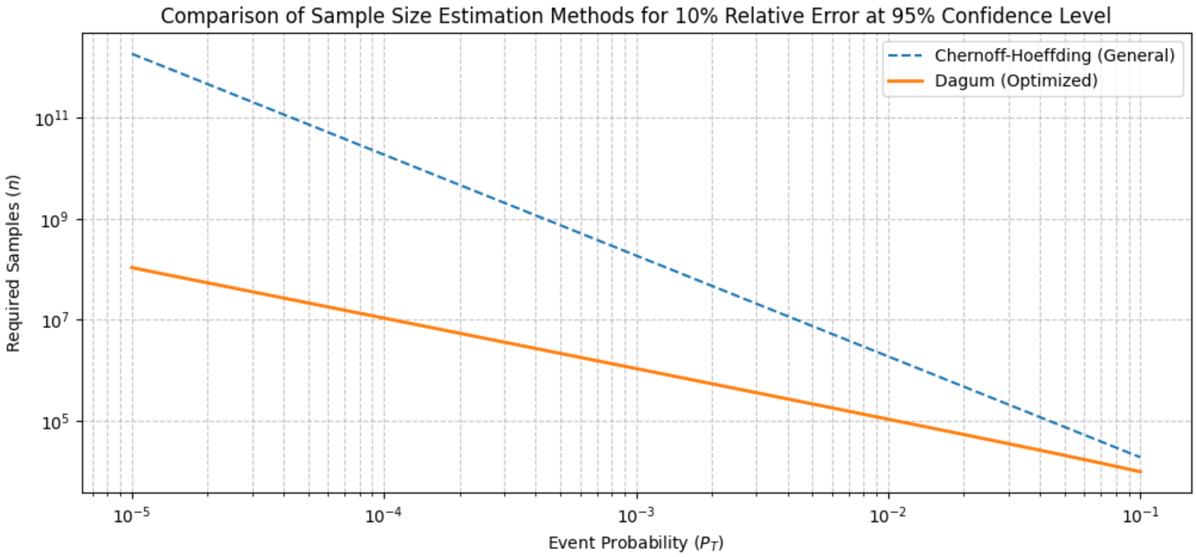

Figure 3.17: Comparison of sample size estimators for PoC convergence and relative error margins.

Table 3.19: Physical properties and state evolution of the primary satellite.

Category	Parameter [units]	Value
Initial State (EME2000)	Epoch [UTC] Position $\mathbf{r}$ [km] Velocity $\mathbf{v}$ [km/s]	2010-02-02 00:50:00 $[-3689.220,\ 5722.423,\ 2286.732]$ $[-0.865,\ 2.240,\ -7.054]$
Physical Properties	HBR [m], Mass [kg] Drag A [m^2], C_D SRP A [m^2], C_R	7.50, 2000.00 10.000, 2.000 10.000, 1.200
TCA Event 1 (EME2000)	Epoch [UTC] Position $\mathbf{r}$ [km] Velocity $\mathbf{v}$ [km/s]	2010-02-02 01:00:00 $[-3481.687,\ 5905.908,\ -2107.203]$ $[1.535,\ -1.652,\ -7.114]$
TCA Event 2 (EME2000)	Epoch [UTC] Position $\mathbf{r}$ [km] Velocity $\mathbf{v}$ [km/s]	2010-02-02 04:00:00 $[-2135.249,\ 2714.866,\ 6309.577]$ $[-3.239,\ 5.671,\ -3.552]$

Finally, the analytical results are compared with the MC estimations. The absolute and relative errors are calculated to verify the model accuracy, as shown in Table 3.25. The relative errors obtained are found to be within the margins established by the statistical estimation, validating the the proposed model.

3.2.2. Analytical Results

Following the initial validation, the analytical model is applied to two distinct scenarios designed to evaluate its performance, following some of the the cases studied in Section

Table 3.20: Physical properties and state evolution of secondary satellite 1.

Category	Parameter [units]	Value
Initial State (EME2000)	Epoch [UTC]	2010-02-02 00:50:00
	Position **r** [km]	$[-1969.031,\ 3874.209,\ -5704.060]$
	Velocity **v** [km/s]	$[-3.351,\ 4.912,\ 4.489]$
Physical Properties	HBR [m], Mass [kg]	5.00, 2000.00
	Drag A [m^2], C_D	10.000, 2.000
	SRP A [m^2], C_R	10.000, 1.200
TCA Event 1 (EME2000)	Epoch [UTC]	2010-02-02 01:00:00
	Position **r** [km]	$[-3481.681,\ 5905.924,\ -2107.205]$
	Velocity **v** [km/s]	$[-1.526,\ 1.638,\ 7.110]$

Table 3.21: Physical properties and state evolution of secondary satellite 2.

Category	Parameter [units]	Value
Initial State (EME2000)	Epoch [UTC]	2010-02-02 00:50:00
	Position **r** [km]	$[757.215,\ -2028.756,\ 6863.464]$
	Velocity **v** [km/s]	$[3.857,\ -5.975,\ -2.181]$
Physical Properties	HBR [m], Mass [kg]	5.00, 2000.00
	Drag A [m^2], C_D	10.000, 2.000
	SRP A [m^2], C_R	10.000, 1.200
TCA Event 2 (EME2000)	Epoch [UTC]	2010-02-02 04:00:00
	Position **r** [km]	$[-2135.242,\ 2714.874,\ 6309.583]$
	Velocity **v** [km/s]	$[3.252,\ -5.681,\ 3.545]$

2.4.1

- **Case 1: Influence of the Common Primary Object.** This scenario explores the statistical correlation introduced when multiple secondary objects encounter a single, common primary satellite, evaluating how the primary's uncertainty affects the joint probability.
- **Case 2: Influence of a Common Secondary Object.** The analysis focuses on the situation where both objects are common in both conjunctions, adding an additional source of correlation

The specific configurations and numerical results for each scenario are presented in the following sections. To evaluate the performance of the proposed analytical model, the results will be compared against the most common approximations used now in the operations defined in Section 1.3.3, which can be summarised in:

- **Independent Joint Probability ($P_{1\cap 2,\mathbf{ind}}$):** This metric assumes that the conjunction events are independent. In such cases, the joint probability is calculated

Table 3.22: Initial covariance matrices in the TNW reference frame. Position units are $[km^2]$, velocity units are $[km^2/s^2]$, and cross-terms are $[km^2/s]$.

Object	Initial Covariance Matrix [TNW]					
Primary	4.49e-4	-	-	-	-	-
	-1.89e-5	2.07e-5	-	-	-	-
	-2.36e-6	-7.66e-7	6.49e-6	-	-	-
	-1.87e-8	2.14e-8	-7.98e-10	2.22e-11	-	-
	4.34e-7	-1.93e-8	-2.69e-9	-1.91e-11	4.26e-10	-
	2.00e-8	2.62e-9	-4.78e-9	2.76e-12	1.96e-11	1.16e-11
Sec. 1	8.07e-3	-	-	-	-	-
	4.05e-4	1.45e-4	-	-	-	-
	1.28e-4	1.88e-6	8.46e-4	-	-	-
	4.18e-7	1.50e-7	2.10e-9	1.56e-10	-	-
	7.64e-6	4.39e-7	1.18e-7	4.53e-10	7.31e-9	-
	4.59e-7	4.44e-8	-1.82e-7	4.58e-11	4.40e-10	2.80e-10
Sec. 2	8.35e-3	-	-	-	-	-
	5.18e-4	1.13e-4	-	-	-	-
	-1.66e-4	-2.55e-5	8.58e-4	-	-	-
	5.19e-7	1.16e-7	-2.61e-8	1.19e-10	-	-
	7.83e-6	5.42e-7	-1.79e-7	5.45e-10	7.43e-9	-
	3.49e-7	4.71e-8	2.48e-7	4.79e-11	3.52e-10	3.09e-10

Table 3.23: Summary of Monte Carlo simulation results for the multi-event scenario.

Metric	PoC Event 1 [-]	PoC Event 2 [-]	Joint PoC [-]	TPoC [-]
MC Estimate	1.453×10^{-1}	2.448×10^{-1}	3.952×10^{-2}	3.506×10^{-1}

Table 3.24: Analytical results for the multi-event conjunction scenario.

Metric	PoC Event 1 [-]	PoC Event 2 [-]	Joint PoC [-]	TPoC [-]
Analytical	1.487×10^{-1}	2.436×10^{-1}	3.700×10^{-2}	3.553×10^{-1}

Table 3.25: Absolute and relative error analysis between MC estimates and analytical results.

Error Type	PoC Event 1	PoC Event 2	Joint PoC	TPoC
Absolute [-]	3.43×10^{-3}	1.21×10^{-3}	2.52×10^{-3}	4.74×10^{-3}
Relative [%]	2.304	0.497	6.822	1.334

as the product of the individual probabilities:

$$P_{1\cap 2,\text{ind}} = P_1 P_2 \tag{3.1}$$

The divergence between this value and the analytical joint probability indicates the level of correlation introduced by shared sources of uncertainty.

- **Independent TPoC ($P_{c,\text{ind}}$):** This approximation derives the total probability of collision by assuming independence between events, applying the inclusion-exclusion principle for two sets:

$$P_{c,\text{ind}} = P_1 + P_2 - (P_1 P_2) \tag{3.2}$$

Significant errors in this metric highlight the impact of the correlation between the encounters on the overall mission risk.

- **Small Probability TPoC ($P_{c,\text{sum}}$):** Often used as a conservative upper bound in operational environments, this approximation assumes that P_1 and P_2 are sufficiently small such that their intersection is negligible:

$$P_{c,\text{sum}} = \sum_{i=1}^{n} P_i \approx P_1 + P_2 \tag{3.3}$$

While computationally trivial, this linear sum fails to account for any statistical overlap, leading to potential overestimations when dealing with high-risk scenarios.

Case 1: Influence of the Common Primary Object

In this scenario, the impact of the primary object's uncertainty on the joint probability of collision is analysed. To ensure the comparability of the results across different evaluations, a consistent orbital configuration is maintained for all simulations. The physical properties and state vectors for the primary and secondary objects involved in this case are summarized in Table 3.26, Table 3.27 and Table 3.28.

Table 3.26: Physical properties and state evolution of the Primary Satellite (Target 1) at Initial Epoch and TCA Events.

Category	Parameter [units]	Value
Initial State (EME2000)	Epoch [UTC] Position $\mathbf{r}$ [km] Velocity $\mathbf{v}$ [km/s]	2010-02-01 00:00:00 [−771.467, 2092.346, −6808.723] [3.800, −6.006, −2.276]
Physical Properties	HBR [m], Mass [kg] Drag A [m^2], C_D SRP A [m^2], C_R	7.50, 2000.00 10.000, 2.000 10.000, 1.200
TCA Event 1 (EME2000)	Epoch [UTC] Position $\mathbf{r}$ [km] Velocity $\mathbf{v}$ [km/s]	2010-02-02 01:00:00 [−3481.690, 5905.912, −2107.189] [1.535, −1.652, −7.114]
TCA Event 2 (EME2000)	Epoch [UTC] Position $\mathbf{r}$ [km] Velocity $\mathbf{v}$ [km/s]	2010-02-02 04:00:00 [−2135.249, 2714.867, 6309.575] [−3.239, 5.671, −3.552]

The study is structured into three configurations based on the relative magnitude of the

Table 3.27: Physical properties and state evolution of Secondary Satellite 1 (Chaser 1) at Initial Epoch and TCA Event 1.

Category	Parameter [units]	Value
Initial State (EME2000)	Epoch [UTC]	2010-02-01 00:00:00
	Position $\mathbf{r}$ [km]	$[-3703.538,\ 5629.207,\ 2451.422]$
	Velocity $\mathbf{v}$ [km/s]	$[0.990,\ -2.399,\ 6.990]$
Physical Properties	HBR [m], Mass [kg]	5.00, 2000.00
	Drag A [m^2], C_D	10.000, 2.000
	SRP A [m^2], C_R	10.000, 1.200
TCA Event 1 (EME2000)	Epoch [UTC]	2010-02-02 01:00:00
	Position $\mathbf{r}$ [km]	$[-3481.683,\ 5905.924,\ -2107.190]$
	Velocity $\mathbf{v}$ [km/s]	$[-1.526,\ 1.638,\ 7.110]$

Table 3.28: Physical properties and state evolution of Secondary Satellite 2 (Chaser 2) at Initial Epoch and TCA Event 2.

Category	Parameter [units]	Value
Initial State (EME2000)	Epoch [UTC]	2010-02-01 00:00:00
	Position $\mathbf{r}$ [km]	$[3251.269,\ -4651.352,\ -4451.153]$
	Velocity $\mathbf{v}$ [km/s]	$[-2.143,\ 4.080,\ -5.825]$
Physical Properties	HBR [m], Mass [kg]	5.00, 2000.00
	Drag A [m^2], C_D	10.000, 2.000
	SRP A [m^2], C_R	10.000, 1.200
TCA Event 2 (EME2000)	Epoch [UTC]	2010-02-02 04:00:00
	Position $\mathbf{r}$ [km]	$[-2135.244,\ 2714.875,\ 6309.585]$
	Velocity $\mathbf{v}$ [km/s]	$[3.252,\ -5.681,\ 3.545]$

covariance matrices:

- **Configuration A:** The primary object's covariance is significantly smaller than those of the secondary objects ($\|\mathbf{\Sigma}_p\| \ll \|\mathbf{\Sigma}_s\|$). This represents the most frequent operational reality in space situational awareness.
- **Configuration B:** The primary and secondary uncertainties are of the same order of magnitude ($\|\mathbf{\Sigma}_p\| \approx \|\mathbf{\Sigma}_s\|$). While less common, this serves as an intermediate test for the analytical model.
- **Configuration C:** The primary object's covariance exceeds those of the secondary ($\|\mathbf{\Sigma}_p\| \gg \|\mathbf{\Sigma}_s\|$). Although this is considered operationally infrequent, it is included to highlight the divergence between current approximations and the proposed analytical result.

It should be noted that the collision probabilities utilized in this study are significantly higher than those typically encountered in daily satellite operations. This choice is made for theoretical purposes to ensure high numerical precision and to facilitate the clear observation of the statistical dependencies modelled.

Configuration A: Dominant Secondary Uncertainty In this first configuration, the uncertainties associated with the secondary objects are significantly larger than that of the primary satellite. The initial covariance matrices for this scenario, defined in the TNW reference frame, are provided in Table 3.29.

Table 3.29: Initial covariance matrices in the TNW reference frame. Position units are $[km^2]$, velocity units are $[km^2/s^2]$, and cross-terms are $[km^2/s]$.

Object	Initial Covariance Matrix [TNW]					
Primary	3.76e-05	-	-	-	-	-
	-1.93e-06	1.30e-06	-	-	-	-
	3.22e-06	-1.76e-07	2.12e-06	-	-	-
	-2.07e-09	1.36e-09	-1.89e-10	1.41e-12	-	-
	3.37e-08	-2.19e-09	2.85e-09	-2.35e-12	3.35e-11	-
	2.20e-10	7.11e-11	6.37e-10	7.33e-14	1.49e-13	1.00e-12
Sec. 1	7.52e-04	-	-	-	-	-
	-3.86e-05	2.61e-05	-	-	-	-
	6.44e-05	-3.51e-06	4.24e-05	-	-	-
	-4.15e-08	2.71e-08	-3.77e-09	2.83e-11	-	-
	6.74e-07	-4.38e-08	5.70e-08	-4.68e-11	6.14e-10	-
	4.41e-09	1.42e-09	1.27e-08	1.46e-12	3.12e-12	1.62e-10
Sec. 2	7.52e-04	-	-	-	-	-
	-3.86e-05	2.61e-05	-	-	-	-
	6.44e-05	-3.51e-06	4.24e-05	-	-	-
	-4.15e-08	2.71e-08	-3.77e-09	2.83e-11	-	-
	6.74e-07	-4.38e-08	5.70e-08	-4.68e-11	6.14e-10	-
	4.41e-09	1.42e-09	1.27e-08	1.46e-12	3.12e-12	1.62e-10

The encounter geometry is illustrated in the Figure 3.18, where two distinct statistical formulations are presented for comparison. The left panel displays the standard representation of relative positions and covariances in the B-plane for the two evaluated events isolated. Conversely, the right panel illustrates the conditioned means and covariances that are strictly applied in the resolution of the analytical integral (2.88).

For the first encounter, both the mean and the covariance are identical to the independent case, establishing a consistent reference framework between the two representations. However, the second encounter is represented by its conditioned covariance. Depending on the specific scenario evaluated, this conditioned matrix presents a reduction compared to the isolated marginal covariance of the second event as it has been determined in Section 2.4.1.

Additionally, the spatial displacement of the conditioned mean for the second event is depicted. This illustrates how the expected location of the second encounter shifts dynamically during the resolution of the global nested integral, directly impacting the final computation of the joint collision probability.

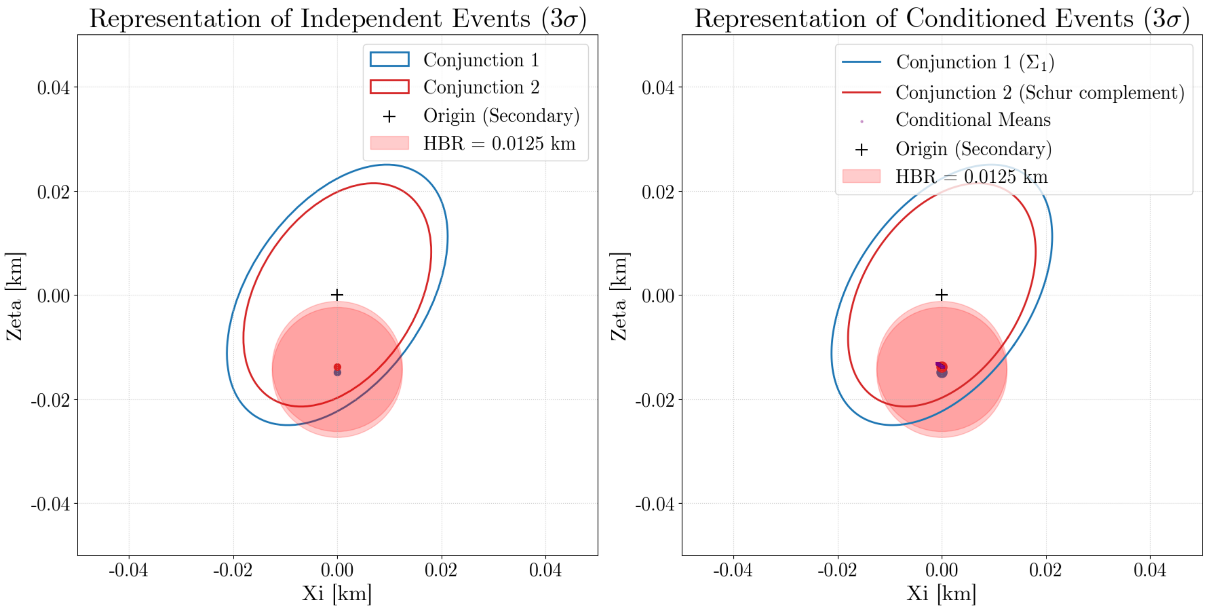

Figure 3.18: Projection of covariance ellipses and the Hard-Body Radius (HBR) onto the B-plane for Configuration A at each TCA. As previously established, given that the primary covariance is significantly smaller than the secondary covariance in this configuration, minimal variance reduction is observed in the conditioned covariance. Furthermore, the conditioned means do not deviate significantly from the independent mean.

The numerical results are summarized in Table 3.30. As expected from the analysis in Section 2.4.1, the small primary covariance leads to low cross-coupling between conjunction events. The conditioned covariance $\mathbf{\Sigma}^*_{Z_2|Z_1}$ is almost identical to the unconditioned $\mathbf{\Sigma}^*_{Z_2}$, and the independent approximation for the joint probability yields a low error. In this case, the error with respect to the approximation of small probabilities is high due to that the PoC studied are high.

Configuration B: Balanced Uncertainties In this configuration, the covariance of the primary satellite is increased to match the order of magnitude of the secondary objects' uncertainties. This transition aims to demonstrate how a larger shared source of uncertainty begins to couple the two conjunction events. The initial covariance matrices for this intermediate scenario are detailed in Table 3.31.

As in the previous configuration, the geometry of the encounter is depicted in the Figure

Table 3.30: Numerical results and error analysis for Configuration A.

Individual Probabilities			
Metric	**Value**		
PoC Event 1 (P_1)	2.924×10^{-1}		
PoC Event 2 (P_2)	3.499×10^{-1}		
Joint Probability Analysis			
Method	**Value [-]**	**Abs. Error [-]**	**Rel. Error [%]**
Analytical Joint ($P_{1\cap 2}$)	1.057×10^{-1}	-	-
Approx. Independent ($P_1 P_2$)	1.023×10^{-1}	3.40×10^{-3}	3.22
Total Probability of Collision (TPoC)			
Method	**Value [-]**	**Abs. Error [-]**	**Rel. Error [%]**
Analytical TPoC	5.366×10^{-1}	-	-
Approx. Independent ($P_1 + P_2 - P_1 P_2$)	5.400×10^{-1}	3.40×10^{-3}	0.63
Approx. Small Prob. ($P_1 + P_2$)	6.423×10^{-1}	1.057×10^{-1}	19.70

Table 3.31: Initial covariance matrices for each object in the TNW reference frame. Position units are $[km^2]$, velocity units are $[km^2/s^2]$, and cross-terms are $[km^2/s]$.

Object	Initial Covariance Matrix [TNW]					
Primary	2.07e-04	-	-	-	-	-
	-1.06e-05	7.17e-06	-	-	-	-
	1.77e-05	-9.65e-07	1.17e-05	-	-	-
	-1.14e-08	7.46e-09	-1.04e-09	7.77e-12	-	-
	1.85e-07	-1.20e-08	1.57e-08	-1.29e-11	1.84e-10	-
	1.21e-09	3.91e-10	3.50e-09	4.03e-13	8.22e-13	5.52e-12
Sec. 1	4.14e-04	-	-	-	-	-
	-2.12e-05	1.43e-05	-	-	-	-
	3.54e-05	-1.93e-06	2.33e-05	-	-	-
	-2.28e-08	1.49e-08	-2.08e-09	1.55e-11	-	-
	3.71e-07	-2.41e-08	3.13e-08	-2.57e-11	3.38e-10	-
	2.42e-09	7.82e-10	7.01e-09	8.04e-13	1.72e-12	8.92e-11
Sec. 2	4.14e-04	-	-	-	-	-
	-2.12e-05	1.43e-05	-	-	-	-
	3.54e-05	-1.93e-06	2.33e-05	-	-	-
	-2.28e-08	1.49e-08	-2.08e-09	1.55e-11	-	-
	3.71e-07	-2.41e-08	3.13e-08	-2.57e-11	3.38e-10	-
	2.42e-09	7.82e-10	7.01e-09	8.04e-13	1.72e-12	8.92e-11

3.19.

The numerical results in Table 3.32 indicate an increase in the relative errors of the independent approximation. As the primary covariance grows, the assumption $P_{1\cap 2} \approx P_1 P_2$

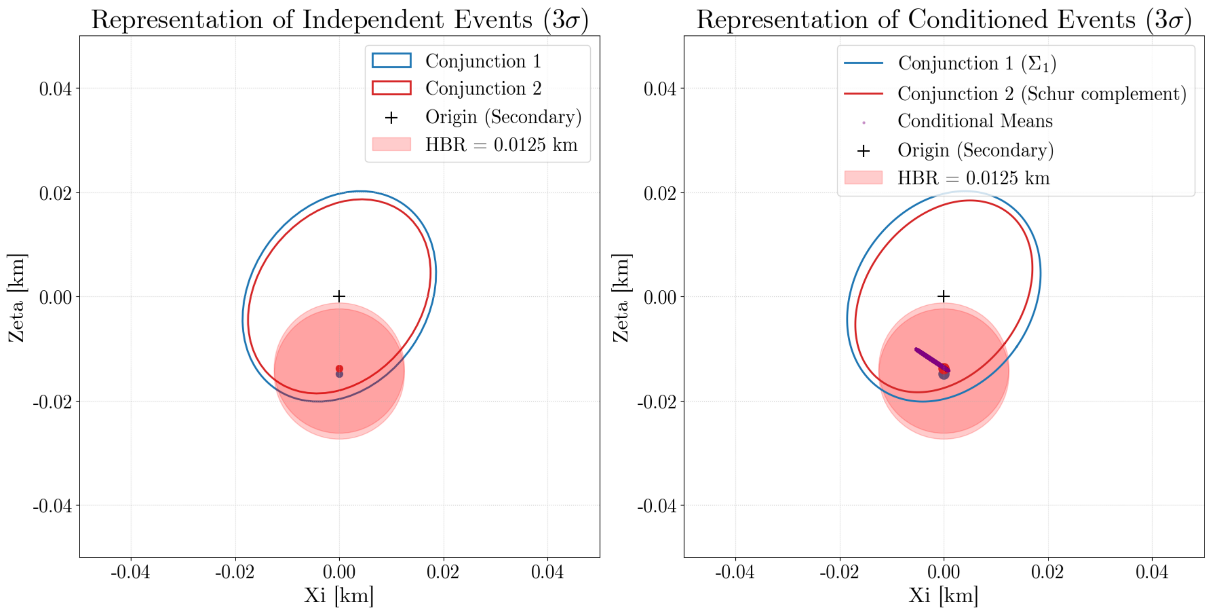

Figure 3.19: Projection of covariance ellipses and the Hard-Body Radius (HBR) onto the B-plane for Configuration B at each TCA. Because the primary and secondary covariances are of the same order of magnitude in this configuration, a more significant variance reduction is observed in the conditioned covariance. Furthermore, the displacement of the conditioned means becomes notable.

becomes less valid, showing the statistical correlation induced by the shared uncertainty. This behaviour aligns with the theoretical prediction that $\mathbf{\Sigma}^*_{Z_2|Z_1}$ is reduced but no longer negligible.

Configuration C: Dominant Primary Uncertainty The final configuration explores an extreme case where the primary object's uncertainty is significantly larger than those of the secondaries. This scenario, while less common operationally, provides a clear limit test for the analytical model. The initial covariance matrices for this dominant primary uncertainty case are summarized in Table 3.33. As shown in the results in Table 3.34, the relative error for the joint probability approximation increases.

The geometry of the encounter is depicted in the Figure 3.20.

The numerical results in Table 3.34 demonstrate an increase in the relative error of the independent approximation. Here, the primary object introduce a strong coupling between the conjunction events. The analytical model correctly captures this dependency, whereas traditional approximations underestimate the joint risk and overestimate the TPoC. This confirms the theoretical predictions: as $\mathbf{\Sigma}_P$ dominates, the conditioned covariance $\mathbf{\Sigma}^*_{Z_2|Z_1}$ and the conditioned mean $\boldsymbol{\mu}^*_{Z_2|Z_1}$ play an important role in the joint probability estima-

Table 3.32: Numerical results and error analysis for Configuration B.

Individual Probabilities			
Metric	**Value [-]**		
PoC Event 1 (P_1)	2.804×10^{-1}		
PoC Event 2 (P_2)	3.359×10^{-1}		
Joint Probability Analysis			
Method	**Value [-]**	**Abs. Error [-]**	**Rel. Error [%]**
Analytical Joint ($P_{1\cap 2}$)	1.081×10^{-1}	-	-
Approx. Independent ($P_1 P_2$)	9.419×10^{-2}	1.39×10^{-2}	12.83
Total Probability of Collision (TPoC)			
Method	**Value [-]**	**Abs. Error [-]**	**Rel. Error [%]**
Analytical TPoC	5.083×10^{-1}	-	-
Approx. Independent ($P_1 + P_2 - P_1 P_2$)	5.221×10^{-1}	1.38×10^{-2}	2.71
Approx. Small Prob. ($P_1 + P_2$)	6.163×10^{-1}	1.080×10^{-1}	21.25

Table 3.33: Initial covariance matrices for each object in the TNW reference frame. Position units are [km^2], velocity units are [km^2/s^2], and cross-terms are [km^2/s].

object	**Initial Covariance Matrix [TNW]**					
Primary	3.76e-04	-	-	-	-	-
	-1.93e-05	1.30e-05	-	-	-	-
	3.22e-05	-1.76e-06	2.12e-05	-	-	-
	-2.07e-08	1.36e-08	-1.89e-09	1.41e-11	-	-
	3.37e-07	-2.19e-08	2.85e-08	-2.35e-11	3.35e-10	-
	2.20e-09	7.11e-10	6.37e-09	7.33e-13	1.49e-12	1.00e-11
Sec. 1	7.52e-05	-	-	-	-	-
	-3.86e-06	2.61e-06	-	-	-	-
	6.44e-06	-3.51e-07	4.24e-06	-	-	-
	-4.15e-09	2.71e-09	-3.77e-10	2.83e-12	-	-
	6.74e-08	-4.38e-09	5.70e-09	-4.68e-12	6.14e-11	-
	4.41e-10	1.42e-10	1.27e-09	1.46e-13	3.12e-13	1.62e-11
Sec. 2	7.52e-05	-	-	-	-	-
	-3.86e-06	2.61e-06	-	-	-	-
	6.44e-06	-3.51e-07	4.24e-06	-	-	-
	-4.15e-09	2.71e-09	-3.77e-10	2.83e-12	-	-
	6.74e-08	-4.38e-09	5.70e-09	-4.68e-12	6.14e-11	-
	4.41e-10	1.42e-10	1.27e-09	1.46e-13	3.12e-13	1.62e-11

tion.

Overall, the results illustrate the influence of the common primary object. When its uncertainty is small, the conjunction events can be treated as independent. As the pri-

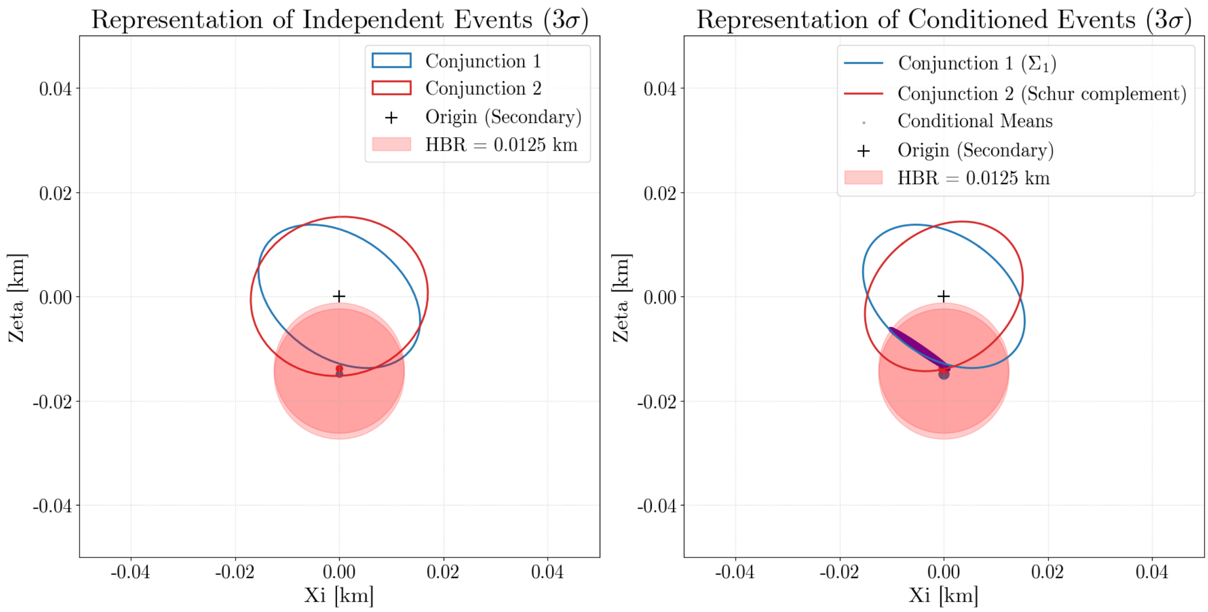

Figure 3.20: Projection of covariance ellipses and the Hard-Body Radius (HBR) onto the B-plane for Configuration C at each TCA. Since the primary covariance dominates the secondary covariance in this configuration, the maximum variance reduction is observed in the conditioned covariance. Furthermore, a highly pronounced spatial displacement is exhibited by the conditioned means.

Table 3.34: Numerical results and error analysis for Configuration C.

Individual Probabilities			
Metric	**Value [-]**		
PoC Event 1 (P_1)	2.304×10^{-1}		
PoC Event 2 (P_2)	3.128×10^{-1}		
Joint Probability Analysis			
Method	**Value [-]**	**Abs. Error [-]**	**Rel. Error [%]**
Analytical Joint ($P_{1\cap 2}$)	1.009×10^{-1}	-	-
Approx. Independent ($P_1 P_2$)	7.205×10^{-2}	2.886×10^{-2}	28.60
Total Probability of Collision (TPoC)			
Method	**Value [-]**	**Abs. Error [-]**	**Rel. Error [%]**
Analytical TPoC	4.422×10^{-1}	-	-
Approx. Independent ($P_1 + P_2 - P_1 P_2$)	4.711×10^{-1}	2.89×10^{-2}	6.53
Approx. Small Prob. ($P_1 + P_2$)	5.431×10^{-1}	1.009×10^{-1}	22.82

mary uncertainty grows, statistical coupling increases, and the analytical model provides accurate joint and total probability estimates, in contrast to simpler approximations.

Case 2: Influence of a Common Secondary Object

In this scenario, the impact of encountering the identical secondary object at two successive epochs is analysed. The statistical correlation is driven by the simultaneous propagation of both the primary and secondary uncertainties between the two events. To ensure the comparability of the results across different evaluations, a consistent orbital configuration is maintained. The physical properties, state vectors, and initial covariances are specific to each evaluation and are detailed in their respective configuration subsections.

The study is structured into two fundamental configurations based on the orbital dynamics and the presence of environmental perturbations:

- **Configuration A (Ideal Unperturbed Scenario):** The orbital propagation is executed via two-body Keplerian dynamics without environmental perturbations. State Transition Matrices (STM) represent the exact dynamic evolution, demonstrating the mathematical boundary where the Schur complement approaches the null matrix.
- **Configuration B (Realistic Perturbed Scenario):** Standard operational perturbations are included, and full state covariances (including initial velocity uncertainties) are propagated. This represents the practical operational reality where the dynamic mapping is complex and the covariance reduction is partial.

As in the previous case, the collision probabilities utilized in this study are higher than those typically encountered in daily operations to ensure numerical precision and facilitate the observation of the statistical phenomena.

Configuration A: Ideal Unperturbed Scenario In this first configuration, the analytical model is tested by removing environmental perturbations. The physical properties, state vectors, and initial covariances for the primary and secondary objects involved in this scenario are summarized in Table 3.35, Table 3.36, and Table 3.37.

The encounter geometry is illustrated in Figure 3.21, where two distinct statistical formulations are presented for comparison. The left panel displays the standard representation of relative positions and covariances in the B-plane for the two evaluated events isolated. Conversely, the right panel illustrates the conditioned means and covariances that are strictly applied in the resolution of the analytical integral.

For the first encounter, both the mean and the covariance are identical to the independent case, establishing a consistent reference framework. However, the second encounter is governed by the theoretical cancellation of uncertainties. Because both objects are identical

Table 3.35: Physical properties and state evolution of the Primary Satellite at Initial Epoch and TCA Events for Configuration A.

Category	Parameter [units]	Value
Initial State (EME2000)	Epoch [UTC] Position $\mathbf{r}$ [km] Velocity $\mathbf{v}$ [km/s]	2010-02-02 00:00:00 $[4852.209,\ 4852.259,\ -4148.669]$ $[2.575,\ 2.575,\ 6.034]$
Physical Properties	HBR [m], Mass [kg] Drag A [m^2], C_D SRP A [m^2], C_R	$7.50,\ 2000.00$ $10.000,\ 2.000$ $10.000,\ 1.200$
TCA Event 1 (EME2000)	Epoch [UTC] Position $\mathbf{r}$ [km] Velocity $\mathbf{v}$ [km/s]	2010-02-02 02:09:15 $[5666.842,\ 5666.875,\ -0.115]$ $[-0.006,\ -0.006,\ 7.052]$
TCA Event 2 (EME2000)	Epoch [UTC] Position $\mathbf{r}$ [km] Velocity $\mathbf{v}$ [km/s]	2010-02-02 04:08:12 $[5666.842,\ 5666.875,\ -0.235]$ $[-0.006,\ -0.006,\ 7.052]$

Table 3.36: Physical properties and state evolution of the Common Secondary Satellite at Initial Epoch and TCA Events for Configuration A.

Category	Parameter [units]	Value
Initial State (EME2000)	Epoch [UTC] Position $\mathbf{r}$ [km] Velocity $\mathbf{v}$ [km/s]	2010-02-02 00:00:00 $[4852.236,\ 4852.308,\ 4148.666]$ $[2.574,\ 2.574,\ -6.034]$
Physical Properties	HBR [m], Mass [kg] Drag A [m^2], C_D SRP A [m^2], C_R	$5.00,\ 2000.00$ $10.000,\ 2.000$ $10.000,\ 1.200$
TCA Event 1 (EME2000)	Epoch [UTC] Position $\mathbf{r}$ [km] Velocity $\mathbf{v}$ [km/s]	2010-02-02 02:09:15 $[5666.843,\ 5666.898,\ -0.115]$ $[-0.006,\ -0.006,\ -7.052]$
TCA Event 2 (EME2000)	Epoch [UTC] Position $\mathbf{r}$ [km] Velocity $\mathbf{v}$ [km/s]	2010-02-02 04:08:12 $[5666.843,\ 5666.898,\ -0.235]$ $[-0.006,\ -0.006,\ -7.052]$

and the propagation is purely linear and unperturbed, the cross-covariance terms perfectly cancel the diagonal block through the Schur complement.

Additionally, the spatial displacement of the conditioned mean for the second event is depicted. In this ideal limit, the conditioned mean interpolates directly around the origin, matching the spatial deviation observed in the first encounter.

The numerical results are summarized in Table 3.38. As expected from the analytical derivations in Section 2.4.1, the strong statistical correlation between the identical events renders the independent probability approximation invalid. The joint probability con-

Table 3.37: Initial covariance matrices for each object in the TNW reference frame for Configuration A. Position units are $[km^2]$, velocity units are $[km^2/s^2]$, and cross-terms are $[km^2/s]$.

Object	Initial Covariance Matrix [TNW]					
Primary	2.07e-04	-	-	-	-	-
	-1.06e-05	7.17e-06	-	-	-	-
	1.77e-05	-9.65e-07	1.17e-05	-	-	-
	-1.14e-08	7.46e-09	-1.04e-09	7.77e-12	-	-
	1.85e-07	-1.20e-08	1.57e-08	-1.29e-11	1.84e-10	-
	1.21e-09	3.91e-10	3.50e-09	4.03e-13	8.22e-13	5.52e-12
Sec.	4.14e-03	-	-	-	-	-
	-2.12e-04	1.43e-04	-	-	-	-
	3.54e-04	-1.93e-05	2.33e-04	-	-	-
	-2.28e-07	1.49e-07	-2.08e-08	1.55e-10	-	-
	3.71e-06	-2.41e-07	3.13e-07	-2.57e-10	3.38e-09	-
	2.42e-08	7.82e-09	7.01e-08	8.04e-12	1.72e-11	8.92e-10

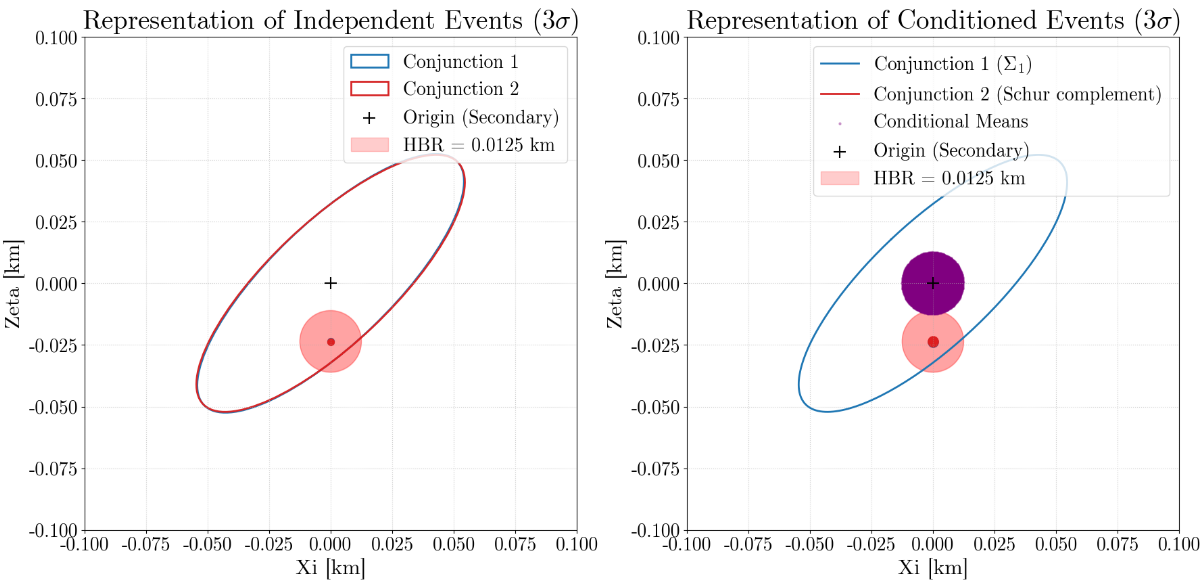

Figure 3.21: Projection of covariance ellipses and the Hard-Body Radius (HBR) onto the B-plane for Configuration A at each TCA. As theoretically established for ideal unperturbed scenarios, the subtraction term almost perfectly cancels the marginal covariance, driving the conditioned covariance toward a null matrix. Consequently, the conditioned mean dictates the deterministic location of the second encounter.

verges toward the theoretical upper bound (the minimum of the individual probabilities), behaving similarly to a Dirac delta distribution.

Table 3.38: Numerical results and error analysis for Configuration A (Ideal Unperturbed).

Individual Probabilities			
Metric	**Value [-]**		
PoC Event 1 (P_1)	6.435×10^{-2}		
PoC Event 2 (P_2)	6.700×10^{-2}		
Joint Probability Analysis			
Method	**Value [-]**	**Abs. Error [-]**	**Rel. Error [%]**
Analytical Joint ($P_{1\cap 2}$)	6.433×10^{-2}	-	-
Approx. Independent ($P_1 P_2$)	4.312×10^{-3}	6.002×10^{-2}	93.30
Total Probability of Collision (TPoC)			
Method	**Value [-]**	**Abs. Error [-]**	**Rel. Error [%]**
Analytical TPoC	6.702×10^{-2}	-	-
Approx. Independent ($P_1 + P_2 - P_1 P_2$)	1.270×10^{-1}	6.002×10^{-2}	89.56
Approx. Small Prob. ($P_1 + P_2$)	1.314×10^{-1}	6.433×10^{-2}	95.99

Configuration B: Realistic Perturbed Scenario In this configuration, standard orbital perturbations are restored to the propagation model, reflecting realistic operational conditions. The physical properties, state vectors, and initial covariances applied in this scenario are detailed in Table 3.39, Table 3.40, and Table 3.41.

Table 3.39: Physical properties and state evolution of the Primary Satellite at Initial Epoch and TCA Events for Configuration B.

Category	Parameter [units]	Value
Initial State (EME2000)	Epoch [UTC] Position $\mathbf{r}$ [km] Velocity $\mathbf{v}$ [km/s]	2010-02-02 00:00:00 $[4125.495,\ 4125.557,\ 3527.302]$ $[2.792,\ 2.792,\ -6.544]$
Physical Properties	HBR [m], Mass [kg] Drag A [m^2], C_D SRP A [m^2], C_R	7.50, 2000.00 10.00, 2.00 10.00, 1.20
TCA Event 1 (EME2000)	Epoch [UTC] Position $\mathbf{r}$ [km] Velocity $\mathbf{v}$ [km/s]	2010-02-02 01:09:42 $[-5666.610,\ -5666.555,\ 0.011]$ $[-0.007,\ -0.007,\ -7.054]$
TCA Event 2 (EME2000)	Epoch [UTC] Position $\mathbf{r}$ [km] Velocity $\mathbf{v}$ [km/s]	2010-02-02 03:08:41 $[-5666.649,\ -5666.571,\ -0.207]$ $[-0.007,\ -0.007,\ -7.054]$

The geometry of the encounter is depicted in Figure 3.22.

The numerical results presented in Table 3.42 illustrate the effect of these perturbations.

Table 3.40: Physical properties and state evolution of the Common Secondary Satellite at Initial Epoch and TCA Events for Configuration B.

Category	Parameter [units]	Value
Initial State (EME2000)	Epoch [UTC] Position **r** [km] Velocity **v** [km/s]	2010-02-02 00:00:00 [4852.236, 4852.308, 4148.666] [2.574, 2.574, −6.034]
Physical Properties	HBR [m], Mass [kg] Drag A [m^2], C_D SRP A [m^2], C_R	5.00, 2000.00 10.00, 2.00 10.00, 1.20
TCA Event 1 (EME2000)	Epoch [UTC] Position **r** [km] Velocity **v** [km/s]	2010-02-02 01:09:42 [−5666.629, −5666.549, 0.011] [−0.007, −0.007, 7.054]
TCA Event 2 (EME2000)	Epoch [UTC] Position **r** [km] Velocity **v** [km/s]	2010-02-02 03:08:41 [−5666.605, −5666.562, −0.207] [−0.007, −0.007, 7.054]

Table 3.41: Initial covariance matrices for each object in the TNW reference frame for Configuration B. Position units are $[km^2]$, velocity units are $[km^2/s^2]$, and cross-terms are $[km^2/s]$.

Object	Initial Covariance Matrix [TNW]					
Primary	2.07e-04	-	-	-	-	-
	-1.06e-05	7.17e-06	-	-	-	-
	1.77e-05	-9.65e-07	1.17e-05	-	-	-
	-1.14e-08	7.46e-09	-1.04e-09	7.77e-12	-	-
	1.85e-07	-1.20e-08	1.57e-08	-1.29e-11	1.84e-10	-
	1.21e-09	3.91e-10	3.50e-09	4.03e-13	8.22e-13	5.52e-12
Sec.	4.14e-03	-	-	-	-	-
	-2.12e-04	1.43e-04	-	-	-	-
	3.54e-04	-1.93e-05	2.33e-04	-	-	-
	-2.28e-07	1.49e-07	-2.08e-08	1.55e-10	-	-
	3.71e-06	-2.41e-07	3.13e-07	-2.57e-10	3.38e-09	-
	2.42e-08	7.82e-09	7.01e-08	8.04e-12	1.72e-11	8.92e-10

Because the exact cancellation of the Schur complement is prevented, the conditioned covariance retains a low but non-zero dispersion. The conditions required for the Dirac delta approximation are no longer satisfied, meaning the practical joint probability decreases significantly compared to the ideal theoretical bound. However, in this case, both relative positions are no longer identical, deviating the conditional means away from the origin. This produces a negative correlation that makes zero the joint probability.

Overall, the results confirm the mathematical derivations for Case 2. While the theoretical

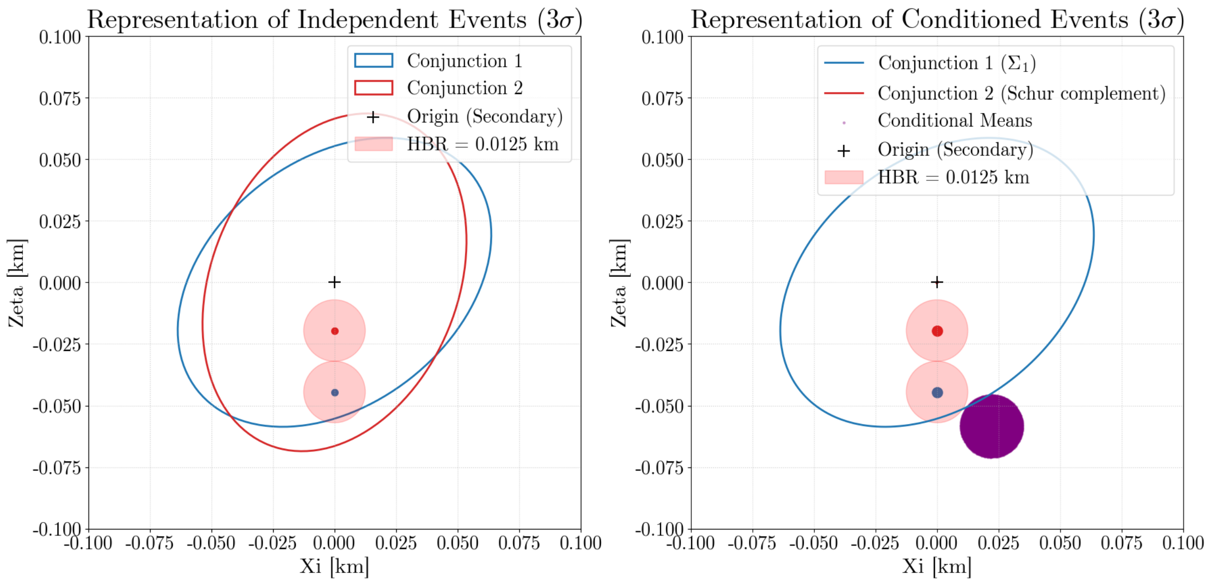

Figure 3.22: Projection of covariance ellipses and the Hard-Body Radius (HBR) onto the B-plane for Configuration B at each TCA. Due to the introduction of perturbations and STM deviations, the cross-terms do not perfectly cancel the diagonal block. Consequently, the conditioned covariance retains a small but strictly positive definite dispersion, and the spatial displacement of the conditioned means deviates from the ideal identity mapping.

Table 3.42: Numerical results and error analysis for Configuration B (Realistic Perturbed).

Individual Probabilities			
Metric	**Value [-]**		
PoC Event 1 (P_1)	1.361×10^{-2}		
PoC Event 2 (P_2)	1.247×10^{-1}		
Joint Probability Analysis			
Method	**Value [-]**	**Abs. Error [-]**	**Rel. Error [%]**
Analytical Joint ($P_{1\cap 2}$)	0.000	-	-
Approx. Independent ($P_1 P_2$)	1.697×10^{-3}	1.70×10^{-3}	-
Total Probability of Collision (TPoC)			
Method	**Value [-]**	**Abs. Error [-]**	**Rel. Error [%]**
Analytical TPoC	1.383×10^{-1}	-	-
Approx. Independent ($P_1 + P_2 - P_1 P_2$)	1.366×10^{-1}	1.70×10^{-3}	1.23
Approx. Small Prob. ($P_1 + P_2$)	1.383×10^{-1}	0.000	0.00

limit bound provides a conceptual understanding of identical recurring events, unmodelled perturbations guarantee a positive definite Schur complement. Traditional independent approximations fail to capture this strong underlying dependency, leading to inaccurate risk assessments, whereas the full analytical model successfully evaluates the true joint and total collision probabilities.

4 | Conclusions

This research work responds to the operational problems caused by the current saturation of space, characterized by the proliferation of objects and orbital debris. As indicated at the beginning, the higher probability of a satellite facing multiple conjunctions in a short time shows the limits of traditional risk metrics. Therefore, the main objective of this thesis has been to overcome the assumption that consecutive events are statistically independent. To achieve this, a complete analytical model that calculates the Total Probability of Collision (TPoC) has been formulated. With this development, a mathematical estimation closer to physical reality has been achieved. This allows measuring the real dependence between encounters and lays the foundation for optimizing collision avoidance maneuvers in the future.

To analyze this complex scenario, the development of the method was first based on defining the physical and statistical problem. To understand the statistical interactions without the geometric difficulty of a three-dimensional environment, the study started by proposing a simplified two-dimensional problem "toy problem". Solving this initial model has been fundamental to isolate, identify, and independently study the different physical causes that generate statistical correlation between successive events, thus preparing the theory for the three-dimensional case.

In this preliminary analysis with the simplified problem, different case studies were introduced progressively. First, the effect of the primary object's uncertainty was evaluated. Then, a scenario where the secondary object is repeated in both encounters was proposed. Afterwards, a direct correlation between both events was added. Finally, a case focused on an uncertain external force affecting all bodies, modeled similarly to a wind, was studied.

By solving these cases, important conclusions for the research were obtained. It was observed that, if the primary object is common and has uncertainty, its influence on the total probability depends on the ratio between its own uncertainty and that of the secondary objects. In the case of the same secondary object in both encounters, a limit situation was found where the correlation coefficients reach extreme values, depending on the geometry of the case. Finally, it was proven that uncertain external forces also modify the risk, provided that their impact is different for each body; if the kinematic effect is identical for all objects, their influence is canceled.

All this initial study served to gain a clear physical and statistical understanding of the system's behavior, preparing the ground to develop the three-dimensional model.

Based on the analytical solutions of the two-dimensional problem, and initially imposing that the multi-event to be studied consists of only two conjunctions (in order to avoid mathematical complexity without losing the necessary rigor to demonstrate the importance of correlations), the method has been successfully adapted to a realistic three-dimensional space environment. To achieve this, the Akella-Alfriend method has been extended, applying it to the double conjunction scenario through the geometric projection of the relative states onto their respective planes perpendicular to the relative velocity (B-planes). This has allowed reducing the joint collision probability integral from six to four dimensions. Furthermore, by using the Schur complement theory, this equation has been successfully separated into two nested double integrals. This factorization greatly optimizes computational efficiency and gives a direct physical meaning to the inner integral, which represents the probability of the second event conditioned on what occurs in the first. As the global equation for the joint probability does not have a simple analytical solution, it has been solved using numerical integration methods, implementing a dynamic meshing strategy adapted to the hard body radius (HBR) and the covariance magnitude to guarantee accuracy without exceeding the computational cost.

The shape of this integral is always the same and does not depend on the studied case. The differences between scenarios are based solely on adjusting the global covariance matrix between both events. The construction of this matrix, and in particular its cross-block that encapsulates the statistical correlation, has been achieved by linearly propagating the state error using State Transition Matrices (STM) between the times of closest approach, and the sensibility position vectors with respect to the atmospheric density. This analysis has been divided into three levels: first, the influence of a common primary satellite in successive events; second, the effect on the matrix in re-encounter scenarios with the same secondary object; and third, the inclusion of the necessary terms to model uncertainties in dynamic systems. Dealing with low Earth orbits (LEO), this last point has focused on the uncertainty of atmospheric density, a parameter that is very difficult to estimate and that strongly affects aerodynamic drag.

Regarding the mathematical results, the behaviour of the three-dimensional model has been successfully matched to the conclusions of the simplified problem. When the secondary objects are different, it has been mathematically proven that the ratio between the primary object's covariance and the secondary's directly defines the degree of correlation between both events. This ratio determines how much the relative position covariance of the second event is reduced, thus dictating the difference that exists between the real probability and the probability obtained by assuming statistical independence.

On the other hand, the scenario of re-encounters with the same secondary object is more sensitive. Here, the linear dependence with the covariance ratio is lost and extreme situations appear, defined mainly by the geometry between both encounters. Since the same bodies are involved in both events, the covariance of the second encounter is drastically reduced. In an ideal case without perturbations, where both orbits share the same period, the encounters can be considered practically identical. Under these conditions, the covariance of the second event conditioned to the first one is reduced to zero, since the absence of a collision in the first event would analytically guarantee survival in the second. However, by introducing perturbations in a more realistic model, the trajectories change, causing the STMs to deviate from the identity matrix. In this perturbed scenario, the conditioned covariance is reduced significantly, but it does not completely vanish. In this way, the possibility of finding operational situations where the correlation is total but negative has been demonstrated, making the joint probability null. In this situation, could be possible to obtain a full positive correlation, but it would be easier to obtain the full negative correlation case.

To conclude, several lines of future work are proposed to complete this research. Primarily, it is necessary to numerically verify the cases that include atmospheric density uncertainty. The analytical study of these scenarios has left very relevant preliminary conclusions. It has been deduced that, no matter how large the density uncertainty is, it is geometrically impossible to completely cancel the conditioned covariance of the second event. This is because the matrix generated by the aerodynamic uncertainty is mathematically of rank one, so it is only capable of reducing the covariance in one specific direction, and never in all three directions at once. Additionally, it has been concluded that this effect depends on the physical properties of the satellites, such as the ballistic coefficient; if the drag effect were identical for all bodies, the relative correlation introduced would be cancelled. Validating this theoretical analysis with real simulations is the natural next step. Likewise, extending this analytical model to sequences of N conjunctions is proposed. Although the theoretical framework naturally permits this extension, future developments must address the significant computational cost associated with solving the resulting high-dimensional nested integrals.

Bibliography

[1] European Space Agency and United Nations Office for Outer Space Affairs. ESA & UNOOSA space debris infographics and podcast. https://www.esa.int/Safety_Security/Space_Debris/ESA_UNOOSA_space_debris_infographics_and_podcast, 2021. [Online; accessed 2-Dec-2025].

[2] ESA Space Debris Office. ESA's Annual Space Environment Report. ESA Technical Report GEN-DB-LOG-00288-OPS-SD, European Space Agency (ESA), Darmstadt, Germany, October 2025. Status: Final.

[3] European Space Agency. Space debris: assessing the risk. https://www.esa.int/Enabling_Support/Operations/Space_debris_assessing_the_risk. [Online; accessed 02-Dec-2025].

[4] NASA Orbital Debris Program Office. Iss maneuvers to avoid potential collisions — orbital debris quarterly news, vol. 27, issue 4 (oct. 2023). https://ntrs.nasa.gov/api/citations/20230014738/downloads/ODQN%2027-4_final.pdf, 2023. [Online; accessed 02-Dec-2025].

[5] European Space Agency. Reentry and collision avoidance. https://www.esa.int/Space_Safety/Space_Debris/Reentry_and_collision_avoidance, 2025. [Online; accessed 02-Dec-2025].

[6] European Space Agency. Space debris faq: How often do active satellites have to perform debris avoidance manoeuvres? https://www.esa.int/Space_Safety/Space_Debris/Space_Debris_FAQ_Frequently_asked_questions, 2025. [Online; accessed 02-Dec-2025].

[7] European Space Agency (ESA). Space Situational Awareness – SSA Programme. https://www.esa.int/About_Us/ESAC/Space_Situational_Awareness_-_SSA, 2025. Accessed: 2025-02-14.

[8] European Space Agency (ESA). Space Surveillance and Tracking – SST Segment. https://www.esa.int/Safety_Security/Space_Surveillance_and_Tracking_-_SST_Segment, 2025. Accessed: 2025-02-14.

[9] European Union Agency for the Space Programme (EUSPA). EU SST – What is Space Surveillance and Tracking? `https://www.euspa.europa.eu/eu-space-programme/ssa/eu-sst`, 2025. Accessed: 2025-02-14.

[10] Oliver Montenbruck and Eberhard Gill. *Satellite Orbits: Models, Methods and Applications*. Springer-Verlag Berlin Heidelberg, 1st edition, 2000. Corrected 3rd Printing 2005.

[11] Consultative Committee for Space Data Systems (CCSDS). *Recommendation for Space Data System Standards: Orbit Data Messages, CCSDS 502.0-B-3, Blue Book*. CCSDS Secretariat, National Aeronautics and Space Administration, Washington, DC, USA, April 2023. Approved by CCSDS Management Council.

[12] CelesTrak. Norad two-line element (tle) sets. `https://celestrak.org/NORAD/elements/index.php?FORMAT=tle`. [Online; accessed 02-Dec-2025].

[13] D Casanova, C Tardioli, and A Lemaître. Space debris collision avoidance using a three-filter sequence. *Monthly Notices of the Royal Astronomical Society*, 442(4):3235–3242, 2014.

[14] Felix R Hoots, Paul L Crawford, and RL Roehrich. An analytic method to determine future close approaches between satellites. *Celestial Mechanics*, 33(2):143–158, 1984.

[15] Maruthi R. Akella and Kyle T. Alfriend. The probability of collision between space objects. *Journal of Guidance, Control, and Dynamics*, 23(5):769–772, 2000.

[16] Salvatore Alfano. Satellite conjunction monte carlo analysis. In *AAS/AIAA Astrodynamics Specialist Conference*, AAS 09-233, Pittsburgh, PA, 2009.

[17] Eduardo Arias, Daniel Sáez, Jorge Rubio, Diego Escobar, Óscar González, and Cristina Pérez. Collision risk estimation in multi-event scenarios. In *74th International Astronautical Congress (IAC)*, IAC-23-A6,2,8,x79843, Baku, Azerbaijan, 2023.

[18] Klaus Merz, Benjamin Bastida Virgili, and Vitali Braun. Risk reduction and collision risk thresholds for missions operated at ESA. In *18th Australian Aerospace Congress*, Melbourne, Australia, 2019.

[19] Roberto Armellin, Pierluigi Di Lizia, and G. Morgan-Lange. Collision avoidance maneuver optimization with a multiple-impulse convex formulation. *Astrodynamics*, 4(3):203–217, 2020.

[20] D. Pavanello, A. Morselli, R. Armellin, and P. Di Lizia. Collision avoidance maneu-

vers optimization in the presence of multiple encounters. In *70th International Astronautical Congress (IAC)*, IAC-19-A6.7.2, Washington D.C., United States, 2019.

[21] D. Pavanello, P. Di Lizia, and R. Armellin. A convex optimization method for multiple encounters collision avoidance. *Journal of Guidance, Control, and Dynamics*, 43(10):1–12, 2020.

[22] ESA Space Debris Office. Esa's annual space environment report. Technical Report GEN-DB-LOG-00288-OPS-SD, European Space Agency, Darmstadt, Germany, 2025.

[23] Doyle T Hall, Matthew D Hejduk, and Lauren C Johnson. Time dependence of collision probabilities during satellite conjunctions. In *27th AAS/AIAA Space Flight Mechanics Meeting*, AAS 17-271, San Antonio, TX, 2017.

[24] NASA. Nasa conjunction assessment handbook, appendix n: Pc calculation approaches. NASA CARA Program, 2024. Update 3/20/24.

[25] Arak M. Mathai and Hans J. Haubold. *Probability and Statistics: A Course for Physicists and Engineers*. Walter de Gruyter / De Gruyter Open, 2018. Open access edition; freely available PDF via De Gruyter Open / OER portals.

[26] T S Nanjundeswaraswamy and Shilpa Divakar. Determination of sample size and sampling methods in applied research. *Proceedings on Engineering Sciences*, 3(1):25–32, 2021.

[27] Doyle T Hall, Luis G Baars, and Stephen J Casali. A multistep probability of collision computational algorithm. In *AAS/AIAA Astrodynamics Specialist Conference*, AAS 23-398, Big Sky, MT, 2023.

[28] Fuzhen Zhang, editor. *The Schur Complement and Its Applications*, volume 4 of *Numerical Methods and Algorithms*. Springer, 2005.

[29] Maurice Fréchet. Généralisation du théorème des probabilités totales. *Fundamenta Mathematicae*, 25(1):379–387, 1935.

[30] Romain Garmier, Juan-Carlos Dolado-Perez, Xavier Pena, Bruno Revelin, and Pierre Legendre. Collision risk assessment for multiple encounters. In *European Space Surveillance Conference*, Madrid, Spain, 2011.

[31] Ryan C Frigm, Matthew D Hejduk, Lauren C Johnson, and Dragan Plakalovic. Total probability of collision as a metric for finite conjunction assessment and collision risk management. In *Advanced Maui Optical and Space Surveillance Technologies (AMOS) Conference*, Maui, HI, 2014.

[32] Zeno Pavanello, Laura Pirovano, Roberto Armellin, Andrea De Vittori, and Pierluigi Di Lizia. A convex optimization method for multiple encounters collision avoidance maneuvers. In *AIAA SCITECH 2024 Forum*, Orlando, FL, 2024.

[33] Zeno Pavanello, Laura Pirovano, Roberto Armellin, Andrea De Vittori, and Pierluigi Di Lizia. Collision avoidance maneuvers optimization in the presence of multiple encounters. *Journal of Guidance, Control, and Dynamics*, 2025. Article in Advance.

[34] Roberto Armellin. Collision avoidance maneuver optimization with a multiple-impulse convex formulation. *Acta Astronautica*, 186:347–362, 2021.

[35] Hunter Morris, Matthew Hejduk, and Lauri Newman. Issues with satellite collision risk aggregation. In *Advanced Maui Optical and Space Surveillance Technologies (AMOS) Conference*, Maui, HI, 2025. Paper presented at AMOS 2025.

[36] Doyle T Hall. Expected collision rates for tracked satellites. *Journal of Spacecraft and Rockets*, 58(3):715–728, 2021.

[37] Doyle T Hall. Ephemeris-based satellite collision rates and probabilities. *Journal of Spacecraft and Rockets*, 62(4):1152–1169, 2025.

[38] Stephen J Casali, Doyle T Hall, Daniel E Snow, Matthew D Hejduk, Lauren C Johnson, Bruce B Skrehart, and Luis G Baars. Effect of cross-correlation of orbital error on probability of collision determination. In *AAS/AIAA Astrodynamics Specialist Conference*, number AAS 18-272, Snowbird, UT, 2018.

[39] Matthew D Hejduk and Daniel E Snow. The effect of neutral density estimation errors on satellite conjunction serious event rates. *Space Weather*, 16(7):849–869, 2018.

Declaration of AI usage:

Artificial intelligence tools were used in this work only for the purpose of improving academic English phrasing and for spelling corrections. All other elements, including the core content, mathematical derivations, graphics, and source code, have been developed exclusively by the author.

List of Figures

List of Tables

Acknowledgements

First and foremost, I would like to express my deepest gratitude to my co-advisors at GMV: Dr. Diego Escobar Antón, Diego Aranda Pradana, and Jorge Rubio Antón. Your guidance and support have been key to the successful development of this thesis. I truly appreciate the dedication you showed in preparing me for this challenge, and the endless patience you had in resolving every doubt and problem that came up during these months of hard work. I am equally grateful to GMV for granting me the opportunity to carry out my internship and thesis within their team, and for trusting me with this project.

I would also like to extend my sincere thanks to my academic advisor, Prof. Pierluigi Di Lizia. Thank you not only for your valuable advice and supervision throughout these months but also for your excellent lectures. The knowledge I gained in your classes significantly shaped my academic formation during my time at Politecnico di Milano.

A very special mention goes to my friends. To those who have been by my side since my early days at the Universidad de Sevilla, all the way to those who shared this final year with me at PoliMi: thank you for always being there. Thank you for putting up with me during the most stressful periods and for your constant encouragement.

Finally, my most heartfelt gratitude belongs to my family. You have always supported my choices and encouraged me to keep moving forward to pursue my dreams. It is entirely thanks to your unconditional love and sacrifices that, step by step, I am turning those dreams into reality. This achievement is as much yours as it is mine.